Title

Proteostasis sustains T cell differentiation potential and tumor-infiltrating lymphocyte function

Journal

Cell, 189(10)

ISSN

0092-8674

Authors

Scharping, Nicole E

Ge, Xuezhen

Matias, Maria Inês

et al.

Publication Date

2026-05-01

DOI

10.1016/j.cell.2026.02.019

HHS Public Access

Author manuscript

Cell. Author manuscript; available in PMC 2026 June 04.

Published in final edited form as:

Cell. 2026 May 14; 189(10): 2857–2874.e31. doi:10.1016/j.cell.2026.02.019.

Proteostasis sustains T cell differentiation potential and tumor-infiltrating lymphocyte function

Nicole E Scharping[1], **Xuezhen Ge**[2], **Maria Inês Matias**[3], **Fulin Jiang**[2], **Allison Cafferata**[1], **Maximilian Heeg**[1], **Alexander Monell**[1], **Giovanni Galletti**[1], **Kitty P Cheung**[1], **Angelica Rock**[1], **Nick Thao**[1], **Sydnye L Shuttleworth**[4], **Michael A. Bauer**[5], **Kennidy K Takehara**[1], **Amir Ferry**[1], **Sara Quon**[1], **Brian Koss**[4], **Samuel A Myers**[3], **Eric J Bennett**[2], **Ananda W Goldrath**[1,6,7]

[1]School of Biological Sciences, Department of Molecular Biology, University of California, San Diego, La Jolla, CA, USA.

[2]School of Biological Sciences, Department of Cell and Developmental Biology, University of California, San Diego, La Jolla, CA, USA.

[3]La Jolla Institute for Immunology, La Jolla, CA, USA.

[4]Department of Biochemistry and Molecular Biology, University of Arkansas for Medical Sciences, Little Rock, AR, USA

[5]Department of Biomedical Informatics, University of Arkansas for Medical Science, Little Rock, AR, USA.

[6]Allen Institute for Immunology, Seattle, WA, USA

[7]Lead contact

Summary:

Tumor-infiltrating lymphocytes (TIL) often fail to restrain tumor growth due to progressive differentiation to an ‘exhausted’ state. Tissue-resident memory T cells (T_{RM}) maintain protection from infection for years in healthy tissues, and patient tumors that contain TIL with T_{RM} features are associated with better prognosis. Proteomic and transcriptomic profiling of T cell populations identified proteostasis as a significant factor distinguishing T_{RM} and progenitor-exhausted TIL from terminally-exhausted TIL, including loss of E3 ubiquitin ligases NEURL3, RNF149, and WSB1, with accumulation of unfolded proteins in spite of functional proteasome activity. Enforced expression of these ligases by TIL preserved stem-like $TCF1^+$ populations and improved anti-tumor function, whereas deficiency impaired TIL and altered T cell differentiation

Contact information: Ananda W. Goldrath: agoldrath@ucsd.edu.

Author contributions:

Conceptualization: N.E.S and A.W.G. Methodology: N.E.S and A.W.G. Investigation: N.E.S., X.G., M.I.M., F.J., A.C., G.G., K.P.C., A.R., N.T., S.L.S., K.K.T., A.F., S.Q. Formal Analysis: N.E.S., X.G., M.I.M., M.H., A.M., G.G., S.L.S., M.A.B. Visualization: N.E.S., M.H., A.M., A.W.G. Data Curation: X.G., M.I.M., M.H., G.G., A.M., S.L.S. Resources: B.K., S.A.M., E.J.B., A.W.G. Writing – Original Draft: N.E.S. and A.W.G. Writing – Review & Editing: N.E.S., E.J.B., A.W.G. Supervision: B.K., S.A.M., E.J.B., A.W.G. Project Administration: B.K., S.A.M., E.J.B., A.W.G. Funding Acquisition: A.W.G.

in acute infection. Sustained ligase expression rescued accumulation of unfolded proteins in TIL and improved immunotherapy outcome in preclinical models, underscoring the critical role of proteostasis in TIL function and highlighting a promising avenue for advancing cancer immunotherapy.

In Brief:

Exhausted T cells experience a breakdown of proteostasis, characterized by unfolded protein accumulation and rescued by E3 ubiquitin ligase activity. Targeting T cell proteostasis highlights a promising strategy for cancer immunotherapy.

Graphical Abstract

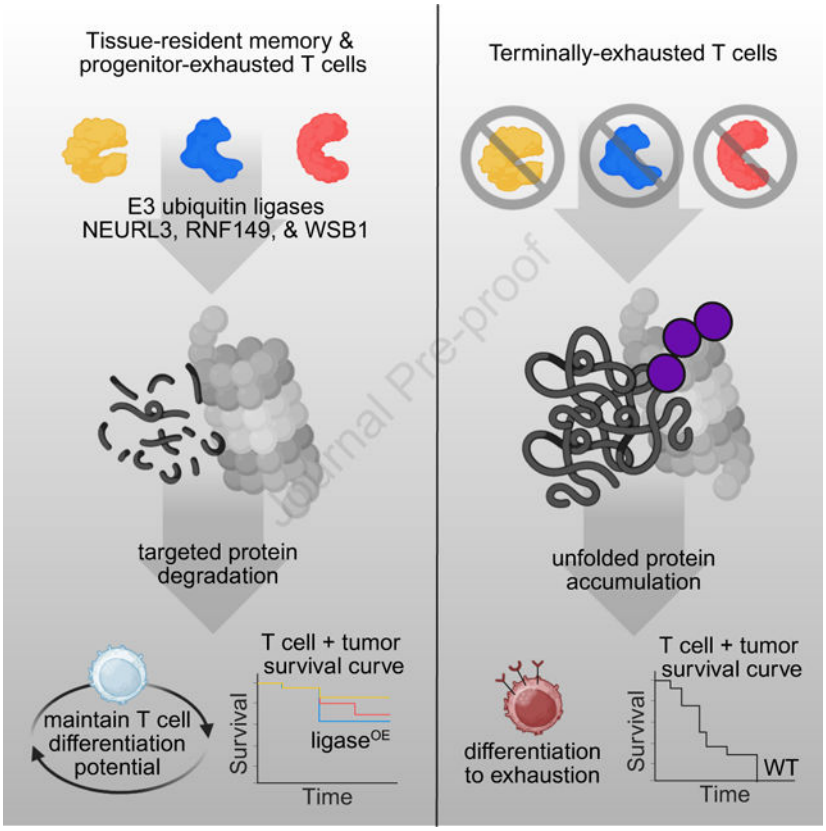

Introduction:

Naive $CD8^+$ T cell activation involves the integration of diverse signals to shape cell fates[1]. In response to tumor or chronic viral infection, persistent TCR stimulation drives T cell differentiation through a progressive loss of function[2], with a spectrum of functionality from more stem-like T_{PEX} to terminally-differentiated T_{EX}[3,4]. T_{PEX} retain self-renewal capacity via TCF1 expression and give rise to T_{EX}. T_{EX} are characterized by co-inhibitory receptor expression including PD-1 and TIM-3, metabolic dysfunction with high levels of reactive oxygen species production from dysfunctional mitochondria, an altered chromatin

landscape associated with expression of the transcription factor TOX that contributes the T_{EX} epigenomic state, and limited cytokine polyfunctionality[5–7].

The T_{RM} population is comprised of long-lived memory T cells that are essential for surveying barrier and non-lymphoid tissues, by providing a first-line defense against reinfection[8]. A population of TIL with T_{RM} features that are distinct from T_{EX} and T_{PEX} has also been identified in some patient tumors[4,9]. We have previously shown that enforcing adaptations consistent with tissue residency through the modulation of transcription factors or immunometabolic pathways are sufficient to improve tumor control in mice[10–12]. In humans, cancer patients with T_{RM}-like TIL show increased overall survival and have improved outcomes after immunotherapeutic checkpoint blockade[9,13]. Thus, elucidating the relationships among T_{PEX}, T_{EX}, and T_{RM}-like TIL populations is important to improve our knowledge of T cell biology and to facilitate the development of cancer immunotherapies.

Protein homeostasis (proteostasis) is an underexplored facet of T cell exhaustion, despite its known function in maintaining stem-like cell states. Targeted protein degradation plays a crucial role in regulating stem cell differentiation and embryonic development via the ubiquitin-proteasome system (UPS), regulating protein turnover by appending chains of ubiquitin onto target proteins[14–16]. E3 ubiquitin ligases are the substrate-specifying arm of the UPS which catalyzes ubiquitin transfer onto target proteins, leading to proteasome-dependent degradation. Beyond its role in cellular differentiation, proteostasis is critical for limiting excess protein accumulation, thus decreasing cellular stress. Accumulation of unfolded proteins due to rapid proliferation or metabolic dysfunction can trigger endoplasmic reticulum (ER) stress and the unfolded protein response (UPR)[17,18] Furthermore, E3-dependent protein degradation is required for optimal responses to environmental stresses, such as hypoxia and increased reactive oxygen species[19] and chronic stress can result in the accumulation of unfolded proteins that drive cellular dysfunction[20].

For T cells, some aspects of proteostasis have been characterized; in naive T cells, activation increases protein synthesis to meet the energy demands of rapid proliferation and differentiation[21–23]. Regulation of protein turnover has been characterized in effector T cell differentiation, as proteasome function plays a role in directing cell fates and inhibition during T cell proliferation has been shown to halt cell-cycle progression[24–26]. Memory T cells maintain a high level of protein turnover at steady state and rely on proteasomal activity for development and survival[27–29]. While more than 500 genes encoding E3 ligases have been identified in the human genome[16], the roles of specific E3 ligases in immune cells are understudied. A well-characterized example in many cell types, including T cells, is the E3 ubiquitin ligase Von Hippel-Lindau (VHL), which targets the transcription factor hypoxia-inducible factor (including HIF1α and HIF2α), allowing the cells to respond transcriptionally to local oxygen levels[30]. We have previously shown that the loss of VHL in T cells increases HIF activity, promoting T cell activity in infections and tumors[12,31]. [32–36]However, which of the hundreds of T cell-expressed ligases are required to maintain proteostasis through regulated protein degradation, and how ligase dysfunction impacts T cell function, are largely unknown.

Here, we show that modulation of T_{RM}- and T_{PEX}-associated E3 ubiquitin ligases NEURL3, RNF149, and WSB1 alters T cell function. Ligase overexpression in TIL increases $TCF1^+$ T cell accumulation and improves T cell function, while ligase knockout (KO) T cells show altered differentiation in the response to cancer and acute infection. We utilize low-input mass spectrometry for unbiased proteomics, enabling for the identification of thousands of proteins from *ex vivo*-sorted T cells, including T_{PEX} and T_{EX}. In characterizing T_{EX}, we show that despite possessing functional proteasomes, T_{EX} accumulate unfolded proteins and by enforcing upstream E3 ligase activity, it is possible to rescue this unfolded protein accumulation. In addition, we enhance proteostasis via ligase overexpression in combination with checkpoint blockade to boost the efficacy of adoptive cell therapy. Together, these data demonstrate the role of proteostasis in T cell exhaustion and identify a promising avenue for advancing immunotherapy.

Results:

Rescue of TIL function by sustained expression of T_{RM}-associated E3 ubiquitin ligases NEURL3, RNF149 and WSB1

To understand the transcriptional relationships between T_{RM} and TIL populations, we first analyzed enrichment of tissue-residency-associated genes among endogenous T_{PEX} cells ($CD8^+PD1^{lo/int}Tim3^-TCF1^{hi}TOX^{lo}$) and T_{EX} cells ($CD8^+PD1^{hi}Tim3^+TCF1^{lo}TOX^{hi}$) sorted from day 14 murine B16 melanoma tumors (Figure 1A, Supplement Figure 2A, Supplemental Table 1)[32,33]. This comparison revealed almost two-thirds of the T_{RM}-associated genes were expressed in T_{PEX}, but downregulated or repressed in T_{EX}. Of the T_{RM}-associated genes lost with terminal-differentiation to T_{EX}, 24% were associated with protein folding and degradation, including genes encoding for E3 ubiquitin ligases neuralized E3 ubiquitin protein ligase 3 (*Neurl3*, also known as *Lincr*), RING finger protein 149 (*Rnf149*), and WD repeat and suppressor of cytokine signaling (SOCS) box-containing 1 (*Wsb1*) (Figure 1B). NEURL3 contains a neuralized domain, and based on sequence-structure annotation, both NEURL3 and RNF149 contain RING domains, which facilitate ubiquitin transfer from E2 ubiquitin-conjugating proteins to target proteins[34,35]. WSB1 contains a SOCS domain (similar to VHL) and can act as a substrate adaptor protein for the multisubunit CUL5 RING ligase (CRL5) complex to facilitate ubiquitin transfer to substrate proteins[36,37]. However, the functions of these three ligases in immune cells are unknown.

We found that antigen-specific T_{RM} isolated from multiple tissues expressed *Neurl3*, *Rnf149*, and *Wsb1* (Figure 1C). In a single-cell (sc) RNA-seq time-course of P14 T cells responding to the lymphocytic choriomeningitis virus (LCMV) Armstrong, ligase expression in the spleen and small intestine intraepithelial lymphocytes (IEL) was observed on day 5 (d5) of infection and peaked at effector to early memory timepoints (Supplemental Figure 2B). *In vitro* exhaustion also led to significantly decreased ligase expression, an observation consistent with data from *ex vivo* T_{EX} (Supplemental Figure 2C). To determine if enforced ligase expression could improve TIL function, we overexpressed NEURL3, RNF149, or WSB1 in P14 TCR-transgenic $CD8^+$ T cells, specific for the LCMV glycoprotein 33–41 peptide ($GP_{33–41}$) (Supplemental Figure 2D). Ligase-expressing T cells were co-adoptively transferred with an equal number of empty vector (EV) congenically-

mismatched P14 T cells into MC38 adenocarcinoma-bearing mice that expressed $GP_{33–41}$ (Figure 1D, Supplemental Figures 1A). After 10 days, ligase-overexpressing P14 T cells were more abundant in the tumor-draining lymph node (dLN) and the tumor, had a higher frequency of TCF1-expressing cells, and were more polyfunctional following *ex vivo* $GP_{33–41}$ peptide restimulation compared to EV T cells (Figure 1E–H). However, there were no differences in the frequencies of $Tim3^{hi}Tcf1^{lo}$ cells or TOX^+ cells between control and ligase-overexpressing TIL (Figure 1F, Supplemental Figure 2E). Ligase-overexpressing cells also showed enhanced accumulation and improved TIL function in B16-$GP_{33–41}$ melanoma-bearing mice, but only dLN P14 displayed an increased frequency of TCF1-expressing cells (Supplemental Figure 2F–J). This phenotype indicated that ligase overexpression supported a stem-like population in the dLN, where this phenotype was more apparent in response to a highly immunogenic tumor (MC38) compared to a poorly immunogenic tumor (B16)[38]. To examine the functional impact of ligase overexpression, we used cell therapy-sensitive MC38-$GP_{33–41}$ where EV- or ligase-transduced P14 T cells were transferred into mice after tumor implantation, and tumor growth was monitored (Figure 1I). All three ligase-overexpressing T cell populations either slowed tumor growth or cleared tumors more efficiently than EV P14 T cells, resulting in significantly improved mouse survival (Figure 1J). Overall, we found that T_{PEX} and T_{RM} shared proteostasis-related gene expression, and overexpression of *Neurl3*, *Rnf149*, or *Wsb1* improved T cell function by maintaining a T_{PEX}-like T cell fate in cancer.

Rescue of T cell function by sustained expression of NEURL3, RNF149 and WSB1 in chronic viral infection

We next tested how ligase overexpression impacted T cell differentiation with LCMV-clone 13, which leads to chronic viral infection[39–41] (Figure 2A). We found a higher T_{PEX} frequency ($CX3CR1^{lo}SLAMF6^{hi}$), decreased T_{EX} frequency ($CX3CR1^{lo}SLAMF6^{lo}$) in ligase overexpressing P14 T cells compared to control T cells (Figure 2B). This corresponded with an increased frequency of $TCF1^+$ expression in ligase-overexpressing P14 compared to control, but no difference in frequency of TOX^+ expression (Figure 2C,D). These changes in exhaustion subset frequencies also correspond to increased functionality, with increased frequencies of ligase-overexpressing $TNF^+IFN\gamma^+$ P14 T cells after peptide restimulation compared to control P14 T cells (Figure 2E). These data highlight that ligase overexpression favors T_{PEX} accumulation regardless of exhaustion context.

Loss of NEURL3, RNF149, or WSB1 accelerates T cell exhaustion in tumors and differentiation during acute infection

To understand how loss of NEURL3, RNF149, and WSB1 impacted T cell differentiation, we used CRISPR/Cas9-mediated deletion of each of these ligases and followed the T cell response to both tumor and acute infection. P14 T cells were nucleofected with recombinant Cas9 complexed with trans-activating CRISPR RNA (tracrRNA) and ligase-specific crRNA. Equal numbers of control $Thy1^{KO}$ and $ligase^{KO}$ P14 T cells for each ligase were transferred into B16-$GP_{33–41}$-bearing mice (Figure 3A, Supplemental Figure 3A). Seven days after transfer, all three $ligase^{KO}$ T cell populations were less abundant, had lower $TCF1^+$ frequency, and produced less IFN-γ upon *ex vivo* restimulation, when compared with their control counterparts in the same host (Figure 3B–E). Taken together, these data indicate that

ligase^{KO} T cells become dysfunctional more quickly in comparison to control T cells, with decreased TCF1^{+} frequency and reduced functionality.

To test if NEURL3, RNF149, and WSB1 deletion changed T cell differentiation in acute infection, control and ligase^{KO} P14 T cells were transferred into mice that were then infected with LCMV Armstrong, and T cells were isolated on d5, d7, and d21–22 of infection (Figure 3F). While there were no differences in the number of ligase^{KO} T cells compared to control T cells on d5, we observed increased CD69 expression by ligase^{KO} T cells in the tissue on both d5 and d7 post-infection, including more CD69^{+}CD103^{+}, CD103^{+}, and CCR9^{+} ligase^{KO} T cells in the IEL, suggesting that ligase loss alters differentiation kinetics early after acute infection (Figure 3G–H, Supplemental Figure 1B, 3B,C). In the spleen, ligase deficiency resulted in a higher frequency of CD127^{+} memory-precursor T cells on d5 of infection, but there was no difference in the frequency of KLRG1^{+} short-lived effector T cells (Figure 3I). By d7 post-infection, we observed a decline in the frequency of KLRG1^{+} T cells, which suggested that the ligase^{KO} T cells were already beginning to contract (Figure 3J). At memory timepoints (days 21–22 post-infection), we found that higher frequencies of CD69^{+} ligase^{KO} T cells were maintained in the tissues, and that there was an increase in the number of ligase^{KO} T_{RM} in IEL (Supplemental Figure 3D). In the spleen, we observed decreased frequencies of long-lived, terminal-effector (CD62L^{lo}CD127^{lo}) and effectormemory (CD62L^{lo}CD127^{hi}) T cell subsets, with a corresponding increase in the central-memory (CD62L^{hi}CD127^{hi}) T cell subset, revealed both by frequency and absolute cell number of ligase^{KO} T cells compared with the control T cells, indicating that deficiency in all three ligases had a long-term impact on cell fate (Figure 3K–N). Finally, to directly interrogate the differentiation potential of ligase-deficient T cells, we adoptively transferred control or ligase^{KO} P14 cells into mice that were then infected with LCMV Armstrong. On day 30 of infection, T_{CM} from control or ligase^{KO} P14 T cells were sorted and then co-transferred at a 50:50 ratio into new recipients followed by LCMV Armstrong infection to assess secondary memory differentiation potential. This experiment showed that ligase-deficient T cells were less abundant than control T cells at secondary memory timepoints across tissue compartments (Supplemental Figure 3E). Thus, we found that in response to tumors and to acute infection, loss of ligase expression led to altered T cell differentiation in circulating memory, tissue-resident memory, and TIL populations.

To characterize and compare the functional impact of NEURL3, RNF149, and WSB1 on the T cell transcriptome, we performed scRNA-seq analysis of control and ligase^{KO} P14 T cells on d5 of infection with LCMV Armstrong, when we observed early phenotypic differences. We found that ligase deficiency in either the spleen or IEL shared RNA scRNA-seq clusters with the control and analysis revealed few differentially expressed genes enriched in the ligase^{KO} T cells, indicating that ligase loss-of-function minimally altered the transcriptome. (Supplemental Figure 4A,B, Supplemental Table 2). Consistent with this observation, RNA-seq performed on EV and Neurl3^{OE} P14 T cells obtained from MC38-$GP_{33–41}$ tumors, revealed few significant differences in gene expression between EV and Neurl3^{OE} T cells in the dLN or tumor (Supplemental Figure 4C,D). Taken together, these data indicate that NEURL3, RNF149, and WSB1 impact T cell differentiation, but the presence or absence of these ligases minimally impacted mRNA expression. E3 ligases have been previously shown to control self-renewal and cell-fate determination in intestinal

stem cells, hematopoietic stem cells, and embryonic development through targeted protein degradation[15,42], and therefore NEURL3, RNF149, and WSB1 may be having a similar function in $CD8^+$ T cell differentiation.

Comparing proteostasis in *ex vivo* T_{EX}, T_{PEX}, T_{RM}, and T_{EFF}

As NEURL3, RNF149, and WSB1 likely influence cell differentiation potential and cell fates via targeted protein degradation, we used quantitative proteomics to measure protein abundance in T cells. The extent to which TIL mRNA corresponds to protein expression has mainly been characterized on a gene-by-gene basis and relative mRNA versus protein comparisons have been made for *in vitro*-cultured T cells, lymphocytes at steady-state, and other non-immune cell types, but similar evaluations in *ex vivo* T cells upon infection or tumor formation have been undercharacterized[23,27,43–46]. To understand the proteome in *ex vivo* T cell populations, we used mass spectrometry to compare proteomes in T_{EX} and T_{PEX} from tumors and T_{RM} and T_{EFF} from acute infection (Figure 4A). We isolated P14 T cells from the spleen at the peak of immune response (T_{EFF}) and memory timepoint from IEL (T_{RM}) following LCMV Armstrong infection, as well as endogenous TIL (T_{PEX} and T_{EX}) from B16-bearing mice. We performed scRNA CITE-seq on these populations, as well as proteomic analysis using low-input data-independent acquisition (DIA) mass spectrometry and obtained >8,000 unique proteins per replicate from 1×10^5 sorted cells (Figure 4B,C, Supplemental Tables 3,4). We used TotalSeq oligonucleotide-conjugated antibodies to measure PD-1 and TIM-3 protein expression on TIL in our scRNA-seq data and compared gene-signature enrichment with previously published datasets[3,10], confirming that the T cell populations identified by scRNA-seq were comparable to the bulk sorted T cells analyzed by mass spectrometry (Supplemental Figure 4E,F). To ensure sufficient cell numbers for analysis, we included scRNA-seq data for T_{RM} from both endogenous $CD8^+$ T cells and P14 T cells (Supplemental Figure 4G). Direct comparison of RNA and protein abundances for individual genes revealed that for some genes, RNA and protein showed a linear relationship (quadrant 1 [Q_1], [Q_3]), while other genes had greater protein abundance than RNA expression [Q_2], or greater RNA expression than protein abundance [Q_4] (Figure 4D, Supplemental Figure 4H). Performing pathway enrichment to identify the top three Gene Ontology Biological Processes (GO:BP) pathways in each quadrant revealed that genes with greater protein than RNA expression were enriched for metabolite pathways, while genes with greater RNA than protein expression included enrichment in cytokine pathways, consistent with observations that T_{RM} and other effector T cell populations can maintain cytokine mRNA in a translationally repressed state[47,48] (Figure 4E). Using a distance matrix to summarize the relationships between populations categorized by RNA or protein abundance, we observed different correlation patterns: proteomic analyses revealed that T_{PEX} and T_{EX} were more distinct from each other than suggested by transcriptomic data alone (Figure 4F), highlighting how integrating proteomic analyses of *ex vivo* T cells with RNA expression can improve our understanding of T cell biology.

Analysis of differentially expressed proteins revealed nine unique clusters (Figure 4G, Supplemental Table 5). Performing gene ontology pathway analysis of the top five pathways per cluster revealed unique biological processes associated with each cluster (Figure 4H). We found that T_{RM} had increased levels of proteins associated with roles

in actin organization and the catabolism of small molecule pathways (clusters 1 and 2) and shared upregulation of proteins related to lipid catabolic processes with T_{PEX} (cluster 3). T_{RM}-specific expression of actin-regulatory proteins may indicate a poised activation state, as the immunological synapse requires dynamic actin regulation[49] or it may be related to the motile nature of T_{RM}, as surveying tissue requires dynamic actin regulation for movement[50,51]. For lipid metabolic pathways, lipid catabolism has been previously associated with tissue adaptation and function in T_{RM}, and with improved T cell function in cancer[11,52]. We found that T_{PEX} and T_{EFF} both shared proteins with roles in T cell differentiation (cluster 9), and T_{EX} uniquely upregulated proteins related to glycolysis (cluster 5), consistent with previous reports that T_{EX} upregulate glycolytic activities[53]. We found T_{EX} shared the upregulation of proteasome-mediated, ubiquitin-dependent protein catabolism pathways with T_{RM} (cluster 7), an aspect of T_{EX} biology that had not yet been characterized. Similar analysis of differential gene expression followed by GO BP pathway enrichment using RNA revealed the top RNA-enriched pathways were distinct from most pathways observed in the proteomic data (Supplemental Figure 5). Thus, proteomic analyses revealed distinct enrichment of proteasome-mediated protein catabolism pathways in T_{EX} and T_{RM} and uncovered unique proteomic profiles for each of the T cell populations.

T_{EX} have functional proteasomes, yet accumulate short-lived proteins

Performing GSVA on differentially expressed proteins, we found that both T_{EX} and T_{RM} had increased expression of proteins involved in a number of pathways related to proteasome-dependent degradation relative to T_{EFF} and T_{PEX} (a pattern not reflected in GSVA of differentially-expressed RNA), including protein K48-linked ubiquitination (Figure 5A, Supplemental Figure 6A). We cross-validated our DIA-proteomics results with tandem mass tag (TMT)-based mass spectrometry on both related experimental groups and additional populations: P14 from dLN and B16-$GP_{33–41}$ TIL to allow us to compare endogenous to antigen-specific T cells, T_{EM} and T_{RM} P14 post-LCMV Armstrong infection to compare multiple memory T cell populations, and endogenous T_{PEX} and T_{EX} TIL from B16-$GP_{33–41}$ to validate our DIA-proteomic T_{PEX} and T_{EX} populations (Supplemental Figure 6B,C, Supplemental Table 6). While fewer proteins were identified compared to the DIA-PASEF dataset, we observed similar patterns of protein expression (Supplemental Figure 6D). Using GSVA for differentially expressed proteins followed by GO:BP pathway analysis, we saw similar enrichment in protein degradation and K48-linked ubiquitination in T_{EX} and T_{RM} compared to T_{PEX}, but also found that antigen-specific dLN and TIL P14 had similar relative abundance of the pathway proteins to T_{EX}, indicating that antigen-specific TIL and endogenous T_{EX} showed a similar phenotype (Supplemental Figure 6E). We also found T_{EM} had similar protein degradation pathway phenotype to T_{PEX} rather than T_{RM}, indicating that not all memory T cells upregulate proteasomal degradation and K48-linked ubiquitination equivalently (Supplemental Figure 6E).

To compare the proteostasis status of T_{RM} to additional circulating memory T cell populations, we performed DIA-PASEF mass spectroscopy on P14 T cells sorted on day 33 post LCMV-Armstrong infection from the spleen ($CD127^{hi}CD62L^{hi}$ T_{CM}, $CD127^{hi}CD62L^{lo}$ T_{EM}, $CD127^{lo}CD62L^{lo}$ LLTE) and the IEL (T_{RM}) (Supplemental Figure 7A). We obtained >6,000 unique proteins per replicate from 2×10^3 sorted cells (Supplemental Figure 7B)

and integrated these data with results from Figure 4C by normalizing the datasets to their shared T_{RM} population (Supplemental Figure 7C). We then compared these data to our previously identified cell-type specific protein expression from Figure 4G and found that all three circulating memory T cell populations shared substantial protein expression with T_{RM}-enriched proteins but did not share protein expression with T_{PEX}+T_{RM}, T_{EFF}+T_{PEX}+T_{EX}, or the T_{EX} protein clusters (Supplemental Figure 7D). Using GSVA for differentially-expressed proteins followed by GO:BP pathway analysis on the combined datasets, we observed similar enrichment in protein degradation and K48-linked ubiquitination in T_{EX} and T_{RM} compared to T_{PEX}, T_{EFF}, T_{CM}, T_{EM}, and LLTE (Supplemental Figure 7E).

Increased abundance of K48-linked polyubiquitin chains can be used to indicate defective protein degradation, therefore we measured K48 ubiquitin staining by flow cytometry and found significantly increased levels of K48-linked polyubiquitin in T_{EX} and T_{RM}; however, K48-linked polyubiquitin was higher in T_{EX} compared to other $CD8^+$ T cell groups, suggesting that T_{EX} may have increased proteostasis dysfunction compared to other T cell populations (Figure 5B). To determine if proteasome-mediated protein degradation was functional in the T_{EX} population, we utilized proteasome peptidase activity assays and found that T_{EX} possessed functional proteasomes, as assessed by increased chymotrypsin-like, caspase-like, and trypsin-like proteasome activities compared with the dLN or T_{PEX} populations (Figure 5C).

Interestingly, GO pathway analysis revealed that both T_{EX} and T_{EFF} had higher levels of proteins involved in UPR pathways, a pattern not reflected in RNA expression (Figure 5D, Supplemental Figure 6A). In our TMT-mass spectrometry dataset, we saw both endogenous T_{EX} and antigen-specific $P14^+$ TIL had similarly upregulated proteins involved in the UPR pathways, while endogenous T_{PEX}, P14 T_{EM}, and P14 T_{RM} had decreased relative abundance compared to T_{EX} (Supplemental Figure 6F). In comparison to circulating memory T cells, we also observed enrichment in response to unfolded protein and ER stress response (hallmarks of UPR) only in T_{EX} and T_{EFF}, but not in T_{RM}, T_{PEX}, T_{CM}, T_{EM}, and LLTE (Supplemental Figure 7F). The UPR in TIL has previously been characterized as negatively correlated with T cell function in tumors, since studies limiting UPR activation via IRE1α–XBP1 or PERK–CHOP showed improvement of TIL function[54–57]. To understand proteostasis dysregulation and evaluate protein turnover dynamics within TIL, we performed metabolic protein labeling using heavy isotopes of arginine ($^{13}C_6$, $^{15}N_4$) and lysine ($^{13}C_6$, $^{15}N_2$) in *in vitro*-cultured $CD8^+$ T cells. This approach allowed us to identify rapidly degraded proteins in mouse $CD8^+$ T cells (i.e., half-life ≤8 h, Supplemental Table 7). We then used this data to assign our *ex vivo* proteomics data to short-lived (half-life ≤8 h) and non-short-lived (half-life >8 h to ≤20 h) protein subsets (Figure 5E–H). The abundance of non-short-lived proteins was similar among T_{RM}, T_{EFF}, T_{PEX}, and T_{EX}. However, when quantifying the abundance of short-lived proteins, we observed that T_{EX} had an enrichment for numerous short-lived proteins, despite having functional proteasomes (Figure 5E–H). These data indicate that protein degradation in T_{EX} is dysfunctional either due to a proteasome-independent mechanism or that T_{EX} proteasomal subunit composition may be suboptimal for protein degradation *in vivo* (Figure 5C,E, Supplemental Figure 7G).

Unfolded protein accumulation in T_{EX} is rescued by NEURL3, RNF149, or WSB1 expression

To characterize the conformational states of the proteins in T cells, we stained for unfolded proteins using Proteostat, a dye that fluoresces upon binding to unfolded protein quaternary structures[58]. We found that T_{EX} had significantly increased levels of unfolded proteins compared to T_{PEX}, T_{RM}, and T_{EFF} cells (Figure 6A,B). Inhibiting protein synthesis *ex vivo* for 6 hr did not change unfolded protein accumulation in T_{EX}, despite observing a decrease in Cyclin A2 (a rapidly degraded protein[59]) during this timeframe (Figure 6C). These data indicate that the increased levels of unfolded proteins in T_{EX} do not primarily arise from newly synthesized proteins or from dysfunctional proteasomes.

Since T_{EX} proteasomes were functional and protein synthesis did not drive unfolded protein accumulation, we instead targeted protein degradation upstream of proteasome activity by overexpressing the E3 ubiquitin ligases NEURL3, RNF149, or WSB1 in P14 TIL. We found that there was a minimal impact on dLN T cells, whereas ligase overexpression rescued the elevated unfolded protein accumulation in TIL (Figure 6D). Taken together, these data show that T_{EX} experience a unique proteostasis state in which protein degradation can occur and the UPR is upregulated, yet T_{EX} have significant accumulation of unfolded proteins. Overexpression of NEURL3, RNF149, or WSB1 in T cells rescues accumulation of unfolded proteins, indicating that unfolded proteins contribute to T_{EX} dysfunction and that modulation of specific E3 ubiquitin ligase activity reduces proteotoxic stress.

NEURL3, RNF149, or WSB1 improve immunotherapeutic responses in humans and improve cancer immunotherapy in mice

We next wanted to understand the therapeutic potential of NEURL3, RNF149, and WSB1 expression in the context of anti-tumor immunity. Quantification of the scRNA-seq data from melanoma patient TIL[60] showed that *RNF149* and *WSB1* were expressed at higher levels in T_{RM}-like TIL and T_{PEX} than in other $CD8^+$ T cell populations in the tumor (Figure 7A), consistent with our murine TIL data (Figure 1B). Quantification of *RNF149* and *WSB1* transcripts in patients that received checkpoint blockade showed that prior to the start of therapy, the expression levels of *RNF149* and *WSB1* were moderately predictive of response to therapy, while the levels of *RNF149* and *WSB1* expression following checkpoint blockade were highly correlated with the favorable response to checkpoint blockade (Figure 7B). Human scRNA-seq analysis did not detect the *NEURL3* transcript, however, bulk RNA-seq from patients with metastatic melanoma who had their primary tumor resected and sequenced prior to checkpoint blockade immunotherapy[61] showed higher levels of *NEURL3*, *RNF149*, or *WSB1* expression in patients that had improved survival following checkpoint blockade immunotherapy (Figure 7C). Thus, ligase expression correlates with improved responses to immunotherapy in humans.

To determine if ligase overexpression could improve T cell responses to B16-$GP_{33–41}$ mouse melanoma in a tumor resistant to checkpoint blockade, we combined cell therapy and anti-PD1 antibody treatment. P14 T cells were transduced with all three ligases and adoptively transferred into mice with established B16-$GP_{33–41}$ melanoma and treated with either isotype control or anti-PD1 therapy. We found that triple $ligase^{OE}$ cell therapy with

checkpoint blockade improved tumor control and significantly improved survival compared to EV P14 and triple ligase^{OE} isotype treated mice (Figure 7D,E). Thus, ligase-expressing $CD8^+$ T cell therapy synergizes with checkpoint blockade and improves immunotherapeutic responses to cancer, highlighting the role of proteostasis in regulating anti-tumor T cell responses during immunotherapy targeting co-inhibitory receptors.

Discussion:

In this study, we sought to understand the relationship between T cell function in tumors versus tissues given the association of T_{RM}-like TIL and improved responses to immunotherapy in patients with cancer[9]. The identification of T_{RM}-associated genes lost with terminal differentiation to T_{EX} introduces a tissue adaptation-centered approach to understanding T cell exhaustion, with downregulation of protein folding and degradation expression profiles suggesting that T_{EX} experience disrupted proteostasis, while T_{PEX} and T_{RM} actively maintain proteostasis. Active maintenance of differentiation potential by sustained proteostasis may be an important biological difference between memory and naive T cells: proteasome activity has been shown to be crucial for generating circulating memory T cell populations, and memory T cells maintain a higher level of protein turnover than naive T cells prior to TCR stimulation, while quiescent naive T cells and quiescent stem cells both have low levels of protein synthesis and degradation[27,28,62,63]. Previous research supports the roles of NEURL3, RNF149, and WSB1 in maintaining differentiation potential and responding to cell stress in non-immune cells, which may also help to maintain differentiation potential[64]. NEURL3 was previously shown to target Vimentin for degradation, to inhibit the epithelial mesenchymal transition of nasopharyngeal carcinoma[65]. RNF149 targets BRAF for degradation in cancer cells, reduces reactive oxygen species in cell lines, and regulates protein quality control in the ER during cell stress[66–68]. WSB1 was observed to be expressed under hypoxic conditions, and has been reported to target VHL, DNA damage-responsive ataxia-telangiectasia mutated (ATM) serine/threonine kinase, and Rho-binding protein RhoGDI2 for degradation[69–71]. WSB1 also correlates with increased tumor cell metastasis, although it exerts a protective effect against Parkinson's disease by targeting the leucine-rich repeat kinase 2 protein (LRRK2) in neurons[69,71–73]. It is not clear from our work what the specific targets of NEURL3, RNF149, or WSB1 are in T cells or if targets are shared across cell types. Given that these ligases do not share sequence homology, each ligase may target unique proteins, converging on a similar stem-like phenotype. This may include proteins in the TCR signaling cascade, proteins involved in RNA transcription, or proteins involved in protein translation, or additional pathways that help enforce a stem-like state. Recent publications identifying E3 ligase targets in cell lines using proximity labeling showed many E3 ligases can have hundreds of protein targets[74,75], rather than one predominant target. Defining the protein targets for NEURL3, RNF149, and WSB1 will be an important topic for future work.

Mass spectrometry of immune cells has been used as a tool to reveal metabolic states of *in vitro* and *ex vivo*-isolated T cells[76], but it has previously required large cell numbers for the acquisition of in-depth protein information, making *ex vivo* assessment of rare populations technically challenging. DIA-PASEF mass spectroscopy and TMT mass spectrometry[45] are important technological advancements, allowing for proteomic assessments of less-

abundant populations and yielding higher sensitivity and deeper proteome coverage. Our data is consistent with reports that mRNA profiles poorly correlate with protein expression patterns[23,27,44–46], highlighting that comparing mRNA and protein provides complementary yet unique biological information. This may be a particularly important insight for T_{EX}, as the RNA profiles in T_{EX} do not clearly explain why T_{EX} are dysfunctional or how checkpoint blockade permits some patients to respond to therapy while others do not. Proteomics may help reveal information about T_{EX} and other immune cell populations to aid immunotherapy development.

Our mass spectrometry datasets have revealed shared pathway enrichment in T_{RM} and T_{EX} proteasomal degradation, yet only T_{EX} upregulate UPR, despite having functional proteasomes (Figure 5C,D). Complementary findings examining disrupted proteostasis by T_{EX} were recently reported, further characterizing T_{EX} as not only having unfolded proteins, but protein aggregates and stress granules as well[46]. Comparing T_{EX} to cells from other unfolded protein diseases, such as neurodegenerative diseases, may help us to understand the biological consequences of unfolded protein accumulation in T_{EX}[20]: unfolded proteins themselves or ER stress driven by genetic or environmental factors can trigger the UPR, causing cells to respond transcriptionally to the proteotoxic stress. If this response is successful, the cell will return to proteostasis, known as “adaptive UPR”[20]. Conversely, if the UPR is unable to resolve the proteotoxic stress, this “terminal UPR” state results in cell dysfunction[20]. From our data, we see that T_{EX} upregulate the UPR and yet still have an abundance of unfolded proteins, suggesting that T_{EX} also experience a terminal UPR state. It is unclear whether NEURL3, RNF149, or WSB1 directly reduce the accumulation of unfolded proteins resulting from targeted degradation or instead prevent this phenotype through indirect mechanisms, but since all three ligases rescue unfolded protein accumulation, it suggests that this phenotype is a broader consequence of disrupted proteostasis involving multiple proteins rather than the dysfunction of a single unfolded protein. Proteotoxic cell stress has been shown to be associated with resistance to checkpoint blockade in human cancers[77], therefore engineering T_{EX}-specific proteolysis-targeting chimeras (PROTACs), or ligase overexpression in chimeric antigen receptor (CAR) T cell or other cellular immunotherapies, could be used for immunotherapy in human cancer.

Limitations of the study:

We identify NEURL3, RNF149, and WSB1 as molecular contributors to the maintenance of $CD8^+$ T cells differentiation potential in both cancer and chronic viral infection, but the direct targets remain undefined. Proximity-labeling studies of other E3 ubiquitin ligases have identified hundreds of potential targets, suggesting that these ligases may similarly act through a broad network. It also remains unclear whether unfolded protein accumulation in T_{EX} is a cause or a consequence of dysfunction, therefore future studies will be required to clarify the role of unfolded protein in the overall biological state of T cell exhaustion. In addition, the analysis of human T cell exhaustion is currently limited to gene expression in melanoma. Extending these findings to other human cancer types as well as proteome profiling will be essential to assess the human TIL proteostasis state.

Resource availability:

Lead Contact: Requests for resources and reagents should be directed to and will be fulfilled by the Lead Contact, Ananda Goldrath (agoldrath@ucsd.edu).

Materials availability: Unique reagents generated in this study are available from the lead contact with a completed materials transfer agreement.

Data and Code Availability: The RNA datasets generated during this study are available at NCBI GEO repository as indicated in the key resources table. The mass spectrometry proteomics datasets generated during this study are available at the ProteomeXchange Consortium via the PRIDE partner repository or MassIVE as indicated in the key resources table. This paper does not report original code.

STAR methods:

Reagents: See key resource table.

Software: See key resource table.

Experimental Model and Study Participant Details

Mice: All mouse strains were bred and housed in specific pathogen-free conditions in accordance with the Institutional Animal Care and Use Guidelines of the University of California, San Diego (UCSD) in the temperature range of 18°–23°C in 40%–60% humidity. Male and female mice were used in the present study, between 6–12 weeks old. All the mice used had the C57BL/6J background. P14, Thy1.1 and CD45.1 congenic mice were bred in-house. All the animal studies were approved by the Institutional Animal Care and Use Committees of UCSD and performed in accordance with UC guidelines.

Cell culture: B16 melanoma cells and MC38 colorectal tumor cells that expressed the LCMV glycoprotein epitope amino acids 33–41 (B16-$GP_{33–41}$) and PLAT-E cells were cultured in Dulbecco's modified Eagle's medium + D-glucose supplemented with 10% fetal bovine serum (FBS), 100 U ml^{-1} penicillin, 100 μg ml^{-1} streptomycin, 292 μg ml^{-1} L-glutamine, 1× non-essential amino acids, 1 mM sodium pyruvate, 10 mM HEPES and 55 μM 2-mercaptoethanol. The cell lines were confirmed to be free of mycoplasma using quantitative PCR (qPCR). Enriched $CD8^+$ T cells were maintained in RPMI supplemented with 10% FBS, 100 U ml^{-1} penicillin, 100 μg ml^{-1} streptomycin, 292 μg ml^{-1} L-glutamine, 1× non-essential amino acids, 10 mM HEPES and 55 μM 2-mercaptoethanol. For the protein turnover experiment, T cells were cultured in SILAC media, including SILAC RPMI supplemented with 10% dialyzed FBS, 100 U ml^{-1} penicillin, 100 μg ml^{-1} streptomycin, 292 μg ml^{-1} L-glutamine, 1× non-essential amino acids, 10 mM HEPES and 55 μM 2-mercaptoethanol, heavy isotopes of arginine ($^{13}C_6$, $^{15}N_4$) and lysine ($^{13}C_6$, $^{15}N_2$), and 100 μM alanine[83].

Method Details

Tumor studies: For the MC38-$GP_{33–41}$ TIL analysis, recipient mice were injected intradermally with 1×10^6 MC38-$GP_{33–41}$ adenocarcinoma cells. For co-transfers of transduced P14 cells, donor mice were sex- and age-matched to recipients or female donors, and the cells were transferred into recipients. On d5 post-activation, sorted ametrine$^+$ cells were mixed at a 1:1 ratio and a total of 5×10^5 P14 cells was transferred by intravenous (i.v.) injection into CD45 congenic recipients with d10 tumors. The mice were monitored three times per week, and the mice were sacrificed 10 days after the adoptive T cell transfer, for dLN and TIL analyses. For the MC38-$GP_{33–41}$ tumor growth curves, a total of 1×10^6 P14 cells was transferred by i.v. injection into CD45 congenic recipients with d8 tumors. The mice were monitored three times per week, and mice were removed from the study when their tumors extended 15 mm in any direction.

For the B16-$GP_{33–41}$ TIL analysis, recipient mice were injected intradermally with 2.5×10^5 B16-$GP_{33–41}$ melanoma tumor cells. For co-transfers of transduced P14 cells, donor mice were sex- and age-matched to recipients or female donors, and the cells were transferred into recipients. On d5 post-activation, sorted ametrine$^+$ cells were mixed at a 1:1 ratio and a total of 2×10^6 P14 cells was transferred by i.v. injection into CD45 congenic recipients with d8 tumors. The mice were monitored three times per week, and mice were sacrificed 8 days after the adoptive T cell transfer, for dLN and TIL analyses. For the B16-$GP_{33–41}$ tumor growth curves, a total of 5×10^6 P14 cells was transferred by i.v. injection into CD45 congenic recipients with d6 tumors. Mice were also administered isotype or anti-PD-1 therapy, 200 μg of Armenian hamster isotype antibody or anti-PD-1 antibody intraperitoneally (i.p.) every other day. Mice were removed from the study when their tumors extended 15 mm in any direction.

Infection studies: Donor mice were sex- and age-matched to recipients or female donors, and the cells were transferred into recipients. For LCMV Amstrong experiments, C57BL/6J P14 CD8$^+$ T cells congenic for CD45 or Thy1 were adoptively transferred at 2.5×10^4 cells per recipient mouse by i.v. injection into CD45 or Thy1 congenic recipients. The mice were then infected with 2×10^5 plaque-forming units (pfu) of LCMV Armstrong by i.p. injection 24 h after transfer. For co-transfers of nucleofected cells, P14 cells were mixed at a 1:1 ratio and a total of 5×10^5 P14 cells was transferred by i.v. injection into CD45 or Thy1 congenic recipients. Thereafter, recipient mice were infected with 2×10^5 pfu of LCMV by i.p. injection. For the experiment using sorted T_{CM} followed by reinfection, control or KO T_{CM} P14 cells mixed at a 1:1 ratio and a total of 6×10^3 P14 cells was transferred by i.v. injection into CD45 or Thy1 congenic recipients. Thereafter, recipient mice were infected with 2×10^5 pfu of LCMV by i.p. injection.

For LCMV Cl13 experiments, co-transfers of transduced P14 cells cells were mixed at a 1:1 ratio of sorted, ametrine$^+$ cells, and a total of 2×10^3 P14 cells was transferred by i.v. injection into CD45 or Thy1 congenic recipients. Thereafter, recipient mice were infected with 2×10^6 pfu of LCMV by retro-orbital injection.

Preparations of single-cell suspensions (tumor): Single-cell suspensions of lymphocytes were prepared by mechanical disaggregation followed by treatment with ACK (ammonium–chloride–potassium) lysing buffer. The tumor was minced into small pieces and then incubated in RPMI with 1.2 mg ml^{-1} of HEPES, 292 μg ml^{-1} L-glutamine, 1 mM $MgCl_2$, 1 mM $CaCl_2$, 5% FBS and 100 U ml^{-1} collagenase (Worthington) at 37°C for 30 min.

Lymphocytes from the tumor were separated on a 44%/67% Percoll density gradient. For the B16 experiments, Percoll density gradient separation was followed by lymphocyte separation media to further purify the lymphocytes.

Preparation of single-cell suspensions (other non-lymphoid tissues): To identify $CD8^+$ T cells in the vasculature of nonlymphoid tissues (small intestine, kidney, and liver), 3 μg of anti-CD8α (clone 53–6.7) conjugated with APC-eFluor 780 were injected i.v. into the mice 5 min before sacrifice. Cells that displayed weak or no labeling with the anti-CD8α antibody were considered to be located outside the vasculature. Single-cell suspensions of splenocytes were prepared by mechanical disaggregation followed by treatment with ACK lysing buffer. Intraepithelial lymphocytes (IEL) were prepared through the removal of Peyer's patches and the luminal contents. The small intestine was cut longitudinally and into 1-cm pieces, then incubated at 37°C for 30 min in Hanks' balanced salt solution with 2.1 mg ml^{-1} sodium bicarbonate, 2.4 mg ml^{-1} HEPES, 8% bovine growth serum and 0.154 mg ml^{-1} DTE (EMD Millipore). The kidneys and liver were minced into small pieces and then incubated in RPMI with 1.2 mg ml^{-1} of HEPES, 292 μg ml^{-1} L-glutamine, 1 mM $MgCl_2$, 1 mM $CaCl_2$, 5% FBS and 100 U ml^{-1} collagenase (Worthington) at 37°C for 30 min. Lymphocytes from the small intestine, kidney, and liver were separated on a 44%/67% Percoll density gradient.

Generation of retrovirus-containing supernatants and $CD8^+$ T cell transduction: To generate *Neurl3*-, *Rnf149*-, and *Wsb1*-overexpressing vectors, gBlocks of coding sequences (IDT) were cloned into MSCV-IRES-reporter vectors via NEBuilder HiFi DNA Assembly cloning, and then transformed into DH5alpha competent *Escherichia coli*. Successful cloning was confirmed by whole plasmid sequencing. Retroviral particles were produced by first plating 2 million PLAT-E cells on a 10-cm tissue culture dish 1 day before transfection. On the following day, each plate was transfected with 2 μg of pCL-Eco and 6 μg of the plasmid of interest using TransIT-LT1 (Mirus). After 24 h, plat-E media was replaced with T cell culture media to collect the retrovirus. On the same day, P14 T cells were isolated from the spleen and lymph nodes and negatively enriched; these cells were the resuspended with 2 μg/ml anti-CD28 antibody (catalog no. 37.51, eBioscience) and 50 U/ml IL-2 (CETUS) and plated in a 6-well dish that was coated with 5 μg/ml anti-CD3 antibody (catalog no. 145–2C11, eBioscience) for activation. Twenty-four hours after plating the T cells, retronectin-coated, non-tissue culture-treated plates were first incubated with retroviral media, after which the T cells resuspended in retroviral medium plus IL-2 were added to retronectin plates and spinfected for 40 min at 1,600 RPM at 37°C, followed by incubation overnight in retronectin plates with retroviral medium. Twenty-four hours after transduction, all the $ametrine^+$ cells (as assessed by flow cytometry) were considered to be transduced. For

the TIL analysis experiments, the cells were then sorted based on reporter expression, and expanded *in vitro* prior to adoptive transfer.

CRISPR-mediated gene knockout: P14 T cells were isolated from the spleen and lymph nodes and negatively enriched. They were then resuspended with 2 μg/ml anti-CD28 antibody (catalog no. 37.51, eBioscience) and 50 U/ml IL-2 (CETUS) and plated in a 6-well dish coated with 5 μg/ml anti-CD3 antibody (catalog no. 145–2C11, eBioscience) for activation. At 24 h post-activation, using the P3 Primary Cell 4D-Nucleofector X Kit and Unit, the T cells were electroporated with complexed tracrRNA (IDT), Cas9 (UC Berkeley), and pooled crRNA (IDT). crRNA targeting Thy1 (control) was used alone as a control and was mixed with the conditional crRNA to be used as an indicator of electroporated cells[84,85].

Flow cytometry and cell sorting: For sorting, the cells were incubated with antibodies for 15 min at 4°C in PBS that was supplemented with 0.5% BSA and 2 mM EDTA, followed by cell collection in medium. For flow cytometry, the cells were incubated with the indicated antibodies for 15 min at 4°C in PBS that was supplemented with 2% bovine growth serum and 0.01% sodium azide. All cells were then fixed with Fixation Buffer (BioLegend) to preserve surface staining. Cytoplasmic staining was completed using the BD Cytofix/Cytoperm™ Fixation/Permeabilization Kit (BD), and intranuclear staining was performed using the FoxP3 transcription factor staining kit (eBioscience). For assays that involved $CD8^+$ T cell stimulation, P14 cells were incubated for 4 h in T cell culture medium at 37°C with 10 nM $GP_{33–41}$ peptide and Protein Transport Inhibitor (eBioscience), together with congenially distinct splenocytes for peptide presentation. K48 staining included 10 μM MG-132 and incubation at 37°C for 1 h prior to staining. Proteostat staining included congenically distinct, naive splenocytes added to each well for dye staining normalization, followed by surface staining, surface fixation, and cytoplasmic fixation, followed by staining with Proteostat dye (diluted 1:50,000 in perm wash). The dye was not washed out before running the samples, as according to manufacturer's instructions. For ligase-overexpressing P14 Proteostat staining, Thy1.1 was used as a reporter, due to ametrine's spectral overlap with Proteostat. For ImageStream visualization of Proteostat staining, the same numbers of cells per group were stained to normalize for background staining. Stained cells were analyzed using the LSRFortessa or LSRFortessa X-20 cytometers (BD), FACSDiva software, and Flowjo software (TreeStar). All sorting was performed on BD FACSAria Fusion instruments.

Real-Time PCR: RNA was isolated using the RNeasy Plus Mini Kit (QIAGEN). Complementary DNA was reverse-transcribed using the High Capacity cDNA Reverse Transcription Kit (Applied Biosystems). Real-Time PCR was performed with SYBR Green and primers for *Neurl3*, *Rnf149*, *Wsb1*, and *Actb*; quantification was performed using the $\Delta\Delta C^t$ method.

Proteasome activity assay: Single-cell suspensions of LN and TIL were sorted as described above. After sorting, 5,000 cells per well were plated in 100 μl of medium in a white-walled, clear-bottom plate, with or without 10 μM MG-132 and incubated at 37°C for

1 h. Proteasome activity was then assessed using the Cell-Based Proteasome-Glo 3-Substrate System (Promega) according to the manufacturer's instructions.

CITE-seq of CD3ε$^+$ T cells from B16-GP$_{33–41}$ and LCMV Armstrong

Experimental setup, staining, and sorting – B16-GP$_{33–41}$: Recipient mice were injected intradermally with 5×10^5 B16-GP$_{33–41}$ melanoma tumor cells. Congenically distinct CD45.1.2 P14 T cells and CD45.1 Pmel T cells were activated in vitro (plate-bound CD3 and CD28), expanded to day 5, then 2.5×10^6 of each transgenic were transferred into day 7 tumor recipients (CD45.2 B6 mice). Mice also began 200ug anti-4–1BB + 50ug anti-PD-1 checkpoint blockade immunotherapy or isotype control on the day of adoptive T cell transfer, then every other day thereafter. CD3ε+ T cells from dLN or TIL were profiled by CITE-seq on day 7 after transfer. We first sorted (unless otherwise specified) 90,000 endogenous CD3ε+ T cells or 11,250 transferred T cells from the dLN or tumor into DMEM supplemented with 2% bovine growth serum and 10 mM HEPES. Due to cell number limitations, 10,000 endogenous CD3ε+ cells, 6000 P14 T cells, and 1000 Pmel T cells were sorted from the immunotherapeutic tumor group. When enough cells could not be sorted from the original sample, unstained cells were adding to get a total 500,000 cells. Following the first sort, hash-tagged cells were pooled incubated with the ImmGenT TotalSeq-C custom mouse panel containing a custom panel of 128 antibody-derived tags (ADT; see STAR methods) and washed thoroughly. For the second sort, 50,000 CD3ε+ T total cells from the pooled tissues were sorted. 5,000 CD3ε+ T cells from a naive spleen were also sorted to allow for batch correction with totalVI.

Experimental setup, staining, and sorting – LCMV-Armstrong: Prior to LCMV infection, congenically distinct 5×10^4 naive CD45.1 P14 T cells and 1×10^5 naive CD45.1.2 SMARTA T cells were transferred into naive CD45.2 B6 recipients. Then, CD3ε+ T cells from siIEL. siLPL, prostate, SG, lung, bone marrow, spleen, mesenteric lymph nodes and mediastinal lymph nodes were profiled by CITE-seq on days 7, 30, and 60 of LCMV Armstrong infection. For each timepoint, we first sorted 5×10^4 CD3ε+ T cells from the spleen, prostate, SG, bone marrow, mesenteric lymph node, siIEL, siLPL, lung and mediastinal lymph node were initially sorted (unless otherwise specified) into DMEM supplemented with 2% bovine growth serum and 10 mM HEPES. Due to cell number limitations, on day 7 4.36×10^3 CD3e cells were sorted from the SG and 4.32×10^3 CD3e cells from the prostate. On day 30, 25,106 CD3e cells from the SG, 19,277 CD3e cells from the prostate and 1,245 CD3e cells were sorted from the lung. When 5×10^4 cells could not be sorted from the original sample, unstained cells were adding to get a total 5×10^4 cells. Following the first sort, hash-tagged cells were pooled incubated with ImmGenT TotalSeq-C custom mouse panel containing a custom panel of 128 antibody-derived tags (ADT; see STAR methods) and washed thoroughly. For the second sort, 5×10^4 CD3ε+ T total cells from the pooled tissues were sorted. For each timepoint, 5×10^3 CD3ε+ T cells from a naïve spleen were also sorted to allow for batch correction with totalVI.

Single-cell RNA, TCR, and TotalSeq-C sequencing—Library preparation: The collected cells were pooled and split into two technical replicates (independent libraries) for all subsequent steps. scRNA-seq was performed using 10X Genomics 5'v2 with

feature barcoding for cell surface protein and immune receptor mapping following the manufacturer's instructions. After cDNA amplification, the smaller fragments containing the TotalSeq-C–derived cDNA were purified and saved for feature barcode library construction. The larger fragments containing transcript-derived cDNA were saved for TCR and gene expression library construction. For both cDNA portions, the library size was measured with an Agilent Bioanalyzer 2100 high-sensitivity DNA assay and quantified using a Qubit dsDNA HS assay kit on a Qubit 4.0 fluorometer.

TCR cDNA was amplified from the transcript-derived cDNA by nested PCR according to the manufacturer's protocol. The TCR libraries were then subjected to enzymatic fragmentation, ligation and indexing with unique Dual Index TT set A index sequences with an index PCR. Transcript-derived cDNA was processed into RNA libraries. After enzymatic fragmentation and size selection, purified cDNA was ligated to an Illumina R2 sequence and indexed with unique Dual Index TT set A index sequences with an index PCR. TotalSeq-C–derived cDNA was processed into feature barcode libraries. The cDNA was indexed with unique Dual Index TN set A index sequences with an index PCR. The three libraries were pooled together on the basis of molarity with relative proportions of 47.5% RNA, 47.5% feature barcode, and 5% TCR. This pool was then sequenced on an Illumina NovaSeq S2, 100c. The sequencing configuration followed 10X Genomics specifications.

Single-cell RNA, TCR, and TotalSeq-C sequencing—Data processing: Gene and TotalSeq-C antibody (surface protein panel and hashtags) counts were obtained by aligning reads to mm10(GRCm38) and the M25(GRCm38.p6) GeneCode annotation (GRCm38.p6) of the mouse genome and the DNA barcode for the TotalSeq-C panel using CellRanger software (v7.1.0) with default parameters. Cells were distinguished from droplets with high RNA and TotalSeq-C counts using inflection points on a total count curve (barcodeRanks function in the DropletUtils package). Samples were demultiplexed using hashtag oligo (HTO) counts and the HashSolo algorithm[86], and doublets (cells positive for multiple hashtags) were excluded. Surface protein expression was normalized using the DSB method to remove ambient background and technical noise[87]. Cells were filtered if they met any of the following criteria: expression of two isotype control antibodies, fewer than 150 RNA UMI counts, or >5% mitochondrial gene expression. RNA counts were normalized to 10,000 transcripts per cell using normalize_total() and log-transformed with log1p in Scanpy[88]. Highly variable genes were selected using the Seurat v3 method with batch correction[89], and expression data were scaled to unit variance (max value = 10) prior to integration. To jointly model RNA and protein data, we applied totalVI from the scvi-tools framework[90]. RNA and protein modalities from 3 conditions (d7 LCMV, d30 LCMV, Tumor) were concatenated using MuData, and totalVI was trained to a shared latent space accounting for batch effects and noise.

Clustering, dimensionality reduction, and subset annotation: Cells of interest were first subset from the larger multimodal dataset based on protein expression of CD4 and CD8A. TotalVI-denoised protein values for CD4 and CD8A were visualized in a 2D scatter plot, and thresholds were manually defined to retain CD8-enriched and CD4-low cells, isolating $CD8^+$ T cell populations. To further refine the dataset, P14 TCR transgenic T cells were

identified by high co-expression of TCRVA2 and CD45.1 proteins, using denoised TotalVI protein layers. For RNA-based clustering, we used the totalVI-derived RNA embedding (X_pca) and computed a neighborhood graph using 10 nearest neighbors (sc.pp.neighbors). Clustering was performed using the Leiden algorithm[91] at a resolution of 0.1. UMAP was used for visualization (sc.tl.umap). Clusters were annotated post hoc based on enrichment of previously defined transcriptional signatures for T_{RM}[10], T_{PEX}, T_{EX}, and T_{EFF}[3] subsets. Enrichment scores were calculated using scanpy.tl.score_genes() for each signature and violin plots were generated to visualize signature distribution across clusters. TIL T_{PEX} vs T_{EX} clusters were also confirmed using the protein modality PDCD1 and HAVCR2 expression.

Differential expression and pathway analysis: For each unique pairwise comparison between clusters, a Wilcoxon rank-sum test was applied using scanpy.tl.rank_genes_groups() to identify significantly differentially expressed genes (DEGs)[88] by RNA expression. Genes were considered significant if they had an adjusted p-value < 0.05 and an absolute $\log_2$ fold-change > 1.0. DEGs across clusters was used to construct gene "signatures," representing unique combinations of clusters in which a gene was upregulated. Each signature was stored as a tuple and linked to its associated genes, enabling identification of genes uniquely or jointly expressed across subsets. Each gene signature was subjected to enrichment analysis using the mouse GO:Biological Process 2023 gene set via Enrichr in Python through the gseapy package, with background set to genes expressed in the dataset[92,93]. Signatures with fewer than five genes were excluded. For each valid group the top five pathways (by adjusted p-value) were tagged, all significantly enriched pathways (FDR < 0.05) were retained, and combined pathway lists were exported, both globally and per T cell subset (T_{RM}, T_{PEX}, T_{EX}, T_{EFF}). To visualize pathways enriched across gene signatures, a bubble plot was generated using Seaborn and Matplotlib[94,95]. The size of each point reflected the number of genes contributing to enrichment, while color intensity encoded statistical significance as $-\log_{10}$(FDR), capped at 10. Pathway names were plotted on the y-axis and gene signature combinations on the x-axis. GSVA was performed on normalized scRNA-seq data using defined clusters. Differentially expressed genes between clusters were first identified with Wilcoxon test, and the union of significant DEGs ($|\log_2 FC| > 1$, FDR < 0.05) was used. GO Biological Process gene sets were retrieved with gseapy (GO_Biological_Process_2023, Mouse), mapped to mouse gene symbols, and GSVA scores were computed per cell; pathway differences across clusters were tested by one-way ANOVA with Benjamini–Hochberg FDR correction, and significant pathways were visualized as GSVA score heatmaps using seaborn and matplotlib[93].

CITE-seq of d5 ligase^{KO} P14 T cells from LCMV Armstrong

Experimental setup, staining, and sorting: Congenically distinct P14 T cells were activated and electroporated with complexed tracrRNA, Cas9, and crRNA (as described above) to generate CRISPR control and KO P14 T cells, which were co-transferred into recipients then infected with LCMV Armstrong. On day 5 of infection, P14 T cells from IEL, liver, and spleen, were profiled by CITE-seq. We first sorted 5×10^4 P14 T cells from the IEL, liver, and spleen of 4 pooled mice per group (control vs NEURL3^{KO}, control vs RNF149^{KO}, and control vs WSB1^{KO}) into DMEM supplemented with 2% bovine growth

serum and 10 mM HEPES. Due to the number of groups, all control samples were pooled together and all KO samples were pooled together. Following the first sort, hash-tagged cells were pooled incubated with antibody-derived tags (ADT, TotalSeq™-C Mouse Universal Cocktail, V1.0) and washed thoroughly. For the second sort, all stained cells from the pooled tissues were sorted as well as 5×10^4 CD8+ T cells from a naive spleen were also sorted to allow for batch correction with totalVI.

Single-cell RNA and TotalSeq-C sequencing—Library preparation: scRNA-seq was performed using 10X Genomics 5'v2 with feature barcoding for cell surface protein and immune receptor mapping following the manufacturer's instructions. After cDNA amplification, the smaller fragments containing the TotalSeq-C–derived cDNA were purified and saved for feature barcode library construction. The larger fragments containing transcript-derived cDNA were saved for gene expression library construction. For both cDNA portions, the library size was measured with an Agilent Bioanalyzer D5000 high-sensitivity DNA assay and quantified using a Qubit 2.0 fluorometer.

Transcript-derived cDNA was processed into RNA libraries. After enzymatic fragmentation and size selection, purified cDNA was ligated to an Illumina R2 sequence and indexed with unique Dual Index TT set A index sequences with an index PCR. TotalSeq-C–derived cDNA was processed into feature barcode libraries. The cDNA was indexed with unique Dual Index TN set A index sequences with an index PCR. The two libraries were pooled together on the basis of molarity with relative proportions of 40% GEX (RNA) and 10% surface (feature barcode) for each control and KO pooled samples. This pool was then sequenced on an Illumina NovaSeq X Plus 10B. The sequencing configuration followed 10X Genomics specifications.

Single-cell RNA and TotalSeq-C sequencing—Data processing: Gene expression and TotalSeq-C antibody (surface protein panel and hashtags) counts were obtained using CellRanger (v7.1.0, 10x Genomics) with default parameters. Reads were aligned to the *mm10* (2020) reference transcriptome and the DNA barcode for the TotalSeq-C panel. Samples were demultiplexed using hashtag oligo (HTO) counts and the HashSolo algorithm[86], and doublets (cells positive for multiple hashtags) were excluded. Surface protein expression was normalized using the DSB method to remove ambient background and technical noise[87]. Cells were filtered if they met any of the following criteria: expression of two isotype control antibodies, fewer than 150 RNA UMI counts, or >5% mitochondrial gene expression. RNA counts were normalized to 10,000 transcripts per cell using normalize_total() and log-transformed with log1p in Scanpy[88]. Highly variable genes were selected using the Seurat v3 method with batch correction[89], and expression data were scaled to unit variance (max value = 10) prior to integration. To jointly model RNA and protein data, we applied totalVI from the scvi-tools framework[90]. RNA and protein modalities from 2 conditions (Control and KO) were concatenated using MuData, and totalVI was trained to a shared latent space accounting for batch effects and noise.

Dimensionality reduction & differential expression: Dimensionality reduction was performed using contrastiveVI[96]. UMAP projections were computed using the salient representation, min_dist=1.5. Differentially expressed (DE) genes between knockout (KO)

and control samples were identified using the Wilcoxon rank-sum test as implemented in Scanpy's rank_genes_groups() function[88], DE genes were considered significant if they had an adjusted p-value < 0.05 and an absolute log fold change > 0.1, and visualized using dot plots.

EV and *Neurl3*^{OE} P14 – dLN and TIL bulk RNAseq: Recipient mice were injected intradermally with 1×10^6 MC38-$GP_{33–41}$ adenocarcinoma cells. Congenically distinct P14 T cells were activated and transduced (as described above) to generate EV and *Neurl3*^{OE} P14 T cells, which were co-transferred into recipients on d5 post-activation cells were mixed at a 1:1 ratio and a total of 5×10^5 P14 cells was transferred by intravenous (i.v.) injection into CD45 congenic recipients with d6 tumors. The mice were monitored three times per week, and the mice were sacrificed 6 days after the adoptive T cell transfer. For each replicate, cells from 2–3 mice were pooled per tissue and then 5,000 P14 sorted for bulk RNA-seq. 1×10^3 were then resorted into 1× TCL lysis buffer + 1% 2-mercaptoethanol. Library preparation for ultra-low-input RNA-seq was performed as described online (https://www.immgen.org/img/Protocols/ImmGenULI_RNAseq_methods.pdf).

Trimmomatic was used to remove adapters and trim low-quality reads (NexteraPE-PE.fa:2:30:10:1:TRUE LEADING:3 TRAILING:3 SLIDINGWINDOW:4:15 MINLEN:25)[97]. Trimmed reads were then aligned to the gencode M25 annotation of the mm10 genome using STAR with the default conditions[98]. Aligned reads were then quantified with featureCounts[99] (-t exon -g gene_id -p -B) and DEG was identified using DEseq2[100]. PCA analysis in was generated with the plotPCA function in DEseq2. Volcano Plot was generated with EnhancedVolcano.

Analysis of human melanoma single-cell RNA-seq dataset: Single-cell RNA-seq data from human melanoma patients treated with checkpoint blockade[60] was processed beginning with raw cell-by-gene matrices and associated metadata. Cells were filtered to retain those expressing at least 200 genes, and genes were retained if they were detected in three or more cells. Normalization was performed using Scanpy's normalize_total and log1p functions[88]. Highly variable genes were identified and used for PCA dimensionality reduction. A k-nearest neighbors graph was constructed in PCA space, followed by UMAP embedding[101] and Leiden clustering[91]. Clusters expressing CD8 markers were identified and retained for downstream analysis, and only cells with CD8A expression above a defined threshold were kept. These $CD8^+$ cells were re-clustered, inspected, and clusters of interest were identified based on expression profiles of canonical markers. A subset of clusters were extracted and relabeled (e.g., T_{PEX}, T_{EX}, T_{RM}-like-TIL, etc.) based on gene expression in clusters. UMAP was recomputed for this subset and used for visualization. These renamed clusters were treated as categorical variables and used to stratify subsequent expression analyses. A heatmap was generated using canonical markers and the E3 ligases *RNF149* and *WSB1* to illustrate overlap with transcriptional T cell subsets, and expression values were scaled between 0 and 1 for comparability across genes. Excluding cells with zero expression, violin plots were then generated to visualize *RNF149* and *WSB1* expression across $CD8^+$ T cells, stratified by treatment and response status, and significance was tested using unpaired t-test.

Analysis of T_{RM} infection time course and T_{RM} across tissues: For analysis of the P14 infection time course[80] and P14 T_{RM} across tissues[78], each were combined into a counts matrix using the merge function in Seurat. Data were log(normalized) and scaled using NormalizeData and ScaleData. Data imputation was performed using MAGIC[102] with the log(normalized expression) values and the default settings and the exact solver and plotted as violin plots.

Data Independent Acquisition-parallel accumulation–serial fragmentation mass spectrometry: For the T_{EFF}, T_{PEX}, T_{EX}, and T_{RM} dataset, naive P14 were adoptively transferred into mice and infected with LCMV as described above. At d7, 2 replicates of P14 from the spleen (T_{EFF}) and at d14, 3 replicates comprised of 6 pooled samples of P14 from the IEL (T_{RM}) were isolated, washed with PBS, and frozen as cell pellets. D14 was used as an early memory timepoint due to cell number limitations at d30. For endogenous TIL, mice received B16-$GP_{33–41}$ tumors as described above. Ad d14, 3 replicates comprised of 6 pooled samples each for T_{PEX}, and 3 replicates comprised of 6 pooled samples each for T_{EX} (T_{PEX} sorted on $CD8^+PD1^{lo/int}Tim3^-$ and T_{EX} sorted on $CD8^+PD1^{hi}Tim3^+$) were isolated, washed with PBS, and frozen as cell pellets.

For the T_{CM}, T_{EM}, LLTE, and T_{RM} dataset naive P14 were adoptively transferred into mice and infected with LCMV as described above. At d33, 4 replicates of P14 from the spleen ($CD127^{hi}CD62L^{hi}$ T_{CM}, $CD127^{hi}CD62L^{lo}$ T_{EM}, $CD127^{lo}CD62L^{lo}$ LLTE) and the IEL (T_{RM}) were isolated. The sample processing approach for low input T cell proteomics was adapted from a previous study[103]. 2,000 T cells were sorted into a PCR tube containing 2 μL of freshly prepared cell lysis buffer (0.045% n-dodecyl-β-D-maltoside, 90 mM TEAB pH 8.5) and snap frozen on dry ice.

Sample preparation (T_{EFF}, T_{PEX}, T_{EX}, and T_{RM}): Cell pellets, each containing 10^5 sorted cells, were resuspended in 50 μL of freshly prepared urea lysis buffer (8 M urea, 75 mM NaCl, 50 mM Tris-HCl, pH 8.0, 1 mM NaF, 1 mM sodium orthovanadate, 1 mM β-glycerophosphate). The suspension was sonicated for 300 s (30 s on/30 s off cycles) in a water bath sonicator (Fosmon, model #51028HOM). Protein was reduced with 10 mM TCEP for 30 min, alkylated with 15 mM freshly prepared iodoacetamide (IAA) for 45 min in the dark, and then treated with 10 mM DTT for 15 min to quench excess IAA. The samples were diluted to a final volume of 400 μL with 50 mM Tris-HCl, pH 8.0. For digestion, 200 ng LysC and 400 ng sequencing grade modified trypsin were added to the samples, which were then incubated at 37 °C with shaking overnight. The digestion was terminated by adding formic acid to achieve a final concentration of 1%.

Sample preparation (T_{CM}, T_{EM}, LLTE, and T_{RM}): The samples were incubated at 95°C for 5 min and then at 4°C for 1 min in a thermal cycler (Applied Biosystems). For digestion, 1 μL of 100 ng sequencing grade modified trypsin was added to the solution, which was then incubated at 37 °C in a thermal cycler overnight. The digestion was terminated by adding 1 μL of 6% formic acid.

Analysis (T_{EFF}, T_{PEX}, T_{EX}, and T_{RM}): The digests were desalted using the Stage-Tip method. Subsequently, 2 μL of the 10 μL peptide sample was analyzed using an LC-MS/MS

setup comprising a timsTOF Pro 2 mass spectrometer (Bruker Daltonics) coupled to a nanoElute 2 nano-LC system (Bruker Daltonics) via a CaptiveSpray ion source. Peptides were first loaded onto a trap column (PepMap Neo, 5 mm × 300 μm Trap) and then eluted through a reversed-phase C18 column (PepSep, 25 cm × 150 μm, 1.5 μm) maintained at 50 °C over a 50 min gradient of 5–35% solvent B (acetonitrile in 0.1% formic acid) at a flow rate of 450 nL/min. The peptides were analyzed using data-independent acquisition (dia) Parallel Accumulation-Serial Fragmentation (PASEF) mode. The isolation windows for dia-PASEF were determined based on data-dependent acquisition (dda)-PASEF data[104] and generated by implementing the py_diAID algorithm to maximize proteome coverage[105]. The settings for dda-PASEF included the following: a ramp time and an accumulation time of 75 ms each, one MS scan, and 10 PASEF MS/MS ramps per acquisition cycle. The MS survey scan covered 100–1700 m/z and 0.6–1.6 V·s/cm^2. Precursors with up to 5 charges were selected, with an active exclusion time of 0.4 min. For dia-PASEF, 50 variable isolation windows for 25 dia-PASEF scan cycles (two windows per cycle) were designed to encompass the precursor distribution across the m/z-1/K0 plane as defined by the dda-PASEF data, ranging from 323.6 to 1221.6 m/z and 0.7 to 1.34 V·s/cm^2, resulting in a cycle time of 2.11 s. Collision energy was decreased linearly with increasing mobility, starting from 59 eV at 1/K0 = 1.6 V·s/cm^2 and reducing to 20 eV at 1/K0 = 0.6 V·s/cm^2.

Analysis (T_{CM}, T_{EM}, LLTE, and T_{RM}): The peptides were directly loaded onto a trap column (PepMap Neo, 5 mm × 300 μm Trap), desalted online with 20 μL of solvent A (0.1% formic acid in H2O), and then eluted through a reversed-phase C18 column (PepSep, 25 cm × 150 μm, 1.5 μm) maintained at 50 °C over a 50 min gradient of 2–35% solvent B (0.1% formic acid in acetonitrile) at a flow rate of 300 nL/min. The dia-PASEF was performed as described above with the following modifications: high-sensitivity detection was enabled; ion accumulation and ramp time were set to 200 ms; each MS1 full scan was followed by 10 dia-PASEF MS2 scans (two isolation windows per scan), resulting in a cycle time of 2.2 s.

Data processing (T_{EFF}, T_{PEX}, T_{EX}, and T_{RM}): The dia-PASEF raw files were processed using a library-free search approach in DIA-NN version 1.8.1[106]. An in silico digestion of a UniProt Mus musculus reference proteome (downloaded in January 2023) was employed to predict the spectral library. The search parameters applied included the following: tryptic digestion with up to two missed cleavages, carbamidomethylation of cysteine as a static modification, and oxidation of methionine and N-terminal acetylation as variable modifications. The precursor false discovery rate (FDR) threshold was set at 1%. For quantification, the quantification strategy was set to Robust LC (high precision) and cross-run normalization was set to RT-dependent. Match-between-runs (MBR) was enabled. The resulting protein group matrix from DIA-NN, reported at a 1% FDR (global q-values for protein groups; global and run-specific q-values for precursors), was used for downstream and statistical analysis. The statistical analysis was performed using the limma package in R[107].

Data processing (T_{CM}, T_{EM}, LLTE, and T_{RM}): The data processing was performed as described above with the following modifications: DIA-NN version 2.2 was used;

cysteine modification was unchecked; the quantification strategy was set to QuantUMS (high precision).

Data analysis – differentially expressed proteins and pathway enrichment: Principal component analysis (PCA) was performed on variance-stabilized data (vst and rlog transformations) to visualize sample clustering. Data were structured as a count matrix for differential expression analysis using the DESeq2 package[100]. Sample metadata were loaded in parallel and matched to sample columns for experimental group assignment. Differential expression analysis was performed using a negative binomial generalized linear model (GLM) framework implemented in DESeq2, with group.type used as the design formula. For each pairwise group comparison, significantly differentially expressed proteins were defined as those with an adjusted p-value < 0.05 and an absolute $\log_2$ fold change > 0.5.

Heatmaps of normalized expression values for the union of all DEGs were generated using the pheatmap package. To explore functional patterns among DEGs, hierarchical clustering was applied to the DEG genes were partitioned into 9 expression clusters. Gene Ontology (GO) enrichment analysis for Biological Process (BP) terms was performed on each cluster using the clusterProfiler package[108], with gene symbol-to-Entrez ID mapping via org.Mm.eg.db. Top enriched mouse GO terms were visualized using a custom bubble plot showing $-\log_{10}$ (adjusted p-value) and number of genes per term, with background set to proteins expressed in the dataset. Redundant GO terms were collapsed by prioritizing terms associated with shared gene sets and lower adjusted p-values. All visualizations were created using ggplot2.

GSVA was used to calculate sample-wise enrichment scores using log-transformed, variance-stabilized intensity values. Mouse GO:BP gene sets were used as input, and enrichment scores were computed using the Gaussian kernel density estimation method (kcdf="Gaussian") in the GSVA package[109]. Differential enrichment of GSVA scores across groups was assessed using the limma package[107], and significantly enriched pathways (FDR < 0.05) were identified via linear modeling and empirical Bayes moderation. Pathways related to proteasomal degradation and the unfolded protein response (UPR) were selected based on biological relevance and filtered to remove redundant GO terms, and heatmaps were generated via clustered cell type. Redundancy and overlap among enriched gene sets were assessed via Jaccard similarity matrices.

T_{RM}-anchored normalization and integration: Proteomic data from the two DIA-PASEF datasets were processed in R: protein intensities were $\log_2$-transformed, and sample-median centered. Within each dataset, TRM samples were used as an internal reference to compute a per-gene TRM mean, which was subtracted to generate a TRM-centered matrix. TRM-centered matrices from both datasets were then combined on the union of genes, and genes with any non-finite values were removed for downstream analyses.

PCA, heatmaps, GSVA and pathway analysis: PCA was performed in R using prcomp (base R) and visualized with ggplot2. For heatmaps, TRM-anchored $\log_2$ values were summarized as cell group mean protein expression on a TRM-anchored $\log_2$ scale, row-z-scored, and plotted with pheatmap, using DE and LFC of 0.5-filtered gene clusters (1–5)

as defined in Figure 4G. GSVA was performed with the GSVA R package on the TRM-anchored matrix using mouse GO:BP gene sets to generate pathway activity scores across T cell groups to identify significantly enriched protein degradation and unfolded protein response pathways.

RNA vs protein analysis - RNA–Protein graph, quadrant-based pathway enrichment analysis, and distance matrix: To assess the concordance between gene expression at the transcriptomic and proteomic levels, pseudobulk RNA-seq data and averaged protein intensities were merged by gene symbol. Scatter plots comparing RNA and protein abundances were generated, and genes were assigned to one of four quadrants based on their log-transformed expression relative to the geometric mean of RNA and protein values. For each quadrant (Q1–Q4), gene ontology enrichment analysis was performed using Enrichr via the gseapy package, and the top 3 biological process (GO:BP) pathways (filtered on ≥5 gene expression) were extracted per quadrant, with background set to genes expressed in the dataset [92,93]. The enrichment results were visualized using quadrant-wise bubble plots. Dot sizes encoded the number of genes per pathway and color indicated statistical significance ($-\log_{10}$ *p*-value).

To compare global transcriptome- and proteome-level similarity across subsets, principal component analysis (PCA) was conducted separately for RNA and protein data using scanpy[88]. Pairwise Euclidean distances between subsets in PCA space were computed using scipy.spatial.distance_matrix, and results were visualized as heatmaps.

Tandem Mass Tag mass spectrometry: For memory T cells, naive P14 were adoptively transferred into mice and infected with LCMV as described above. At d14, 3 replicates comprised of 6 pooled samples of $CD127^{hi}CD62L^{lo}$ P14 from the spleen (T_{EM}) and P14 from the IEL (T_{RM}) were isolated, washed with PBS, and frozen as cell pellets. D14 was used as an early memory timepoint due to cell number limitations at d30. For endogenous TIL, mice received B16-$GP_{33–41}$ tumors as described above. Ad d14, 3 replicates comprised of 6 pooled samples each for T_{PEX}, and 3 replicates comprised of 6 pooled samples each for T_{EX} (T_{PEX} sorted on $CD8^+PD1^{lo/int}Tim3^-$ and T_{EX} sorted on $CD8^+PD1^{hi}Tim3^+$) were isolated, washed with PBS, and frozen as cell pellets. For P14 dLN and TIL, mice received B16-$GP_{33–41}$ tumors as described above, then received d5 *in vitro*-activated P14 on d7 after tumor implantation. On d14, 3 replicates comprised of 10 pooled samples each for P14 dLN, 2 replicates comprised of 10 pooled samples each for P14 TIL were isolated, washed with PBS, and frozen as cell pellets.

TMT-based proteomics was performed as previously described[45]. Briefly, samples with several modifications. First, TMTpro reagents were lysed, reduced, and alkylated using 8 M urea, 10 mM TCEP, and 10 mM iodoacetamide. Urea was then diluted to <2 M using 50 mM ammonium bicarbonate, and sequencing-grade trypsin was added at a 1:100 enzyme-to-substrate ratio utilized for overnight digestion at 37°C. The entire digest was passed through a Stage-tip and the on-tip labeling was performed using TMTpro reagents by adding 1 µL of reagent to 100 µL of freshly prepared. 1 uL of TMTpro was added to 50 mM phosphate buffer (pH 8.0), which was then passed before passing over the C18-bound peptides. Peptides were fractionated using Stage-tip-based SDB-RPS fractionation. Peptides

were eluted stepwise using increasing concentrations of acetonitrile (5–90%) in 20 mM ammonium formate, pH 10. Fractions were vacuum-dried and stored at –80°C until LC-MS analysis. Mass spectrometry data were tip. Data was acquired usingon an Orbitrap Eclipse (Thermo Scientific) mass spectrometer.

Raw data were processed using Spectrum Mill software (Agilent and Broad Institute) and searched against the UniProt Mouse database. Carbamidomethylation of cysteine and TMTpro on lysines and peptide N-termini were set as fixed modifications, with oxidation of methionine and protein N-terminal acetylation set as variable modifications. Up to three missed tryptic cleavages were allowed. Peptide and protein FDRs were controlled at <1% using a target-decoy approach. Protein quantification was performed using TMT reporter ion intensities normalized to a pooled reference channel. Proteins were reported if identified by at least two unique peptides and a protein score ≥20. Only one representative proteoform per gene was used for downstream analyses).

GSVA was used to calculate sample-wise enrichment scores using log-transformed, variance-stabilized intensity values. Mouse GO:BP gene sets were used as input, and enrichment scores were computed using the Gaussian kernel density estimation method (kcdf="Gaussian") in the GSVA package[109]. Differential enrichment of GSVA scores across groups was assessed using the limma package[107], and significantly enriched pathways (FDR < 0.05) were identified via linear modeling and empirical Bayes moderation. Pathways related to proteasomal degradation and the unfolded protein response (UPR) were selected based on biological relevance and filtered to remove redundant GO terms, and heatmap was generated via clustered cell type.

To compare T cell proteomic signatures across the two mass spectrometry datasets, intensity values were $\log_2$-transformed (where applicable) and rescaled per gene to the range [–3, 3] using min–max normalization to account for differences in dynamic range across studies. Combined heatmaps were constructed by merging the scaled matrices from both studies. Rows were clustered using hierarchical clustering on row-wise imputed matrices (mean imputation for missing values), while columns were manually ordered to reflect biological groupings. Heatmaps were generated using the pheatmap package and included a top annotation bar to indicate dataset origin. Missing values were colored in gray to distinguish from scaled intensities.

Protein turnover mass spectrometry

Experimental design: WT T cells were activated and electroporated with complexed tracrRNA, Cas9, and crRNA (as described above) to generate CRISPR control and KO T cells, which were then switched to T_{RM} culture conditions (25 U/mL IL-2, 10 ng/mL IL-15, 10 ng/mL TGFβ and 10 nM retinoic acid)[110] 1 day after nucleofection. Cells are expanded 2 more days in T_{RM} culture conditions, then on day 5 post-activation, cells were counted, washed with PBS, and frozen as pellets (for timepoint 0 hr), then remaining cells were switched to SILAC media including heavy isotopes of arginine ($^{13}C_6$, $^{15}N_4$) and lysine ($^{13}C_6$, $^{15}N_2$) plus T_{RM} cytokines. Cells were then sampled, counted, washed with PBS, and frozen as pellets for 2, 4, 8, 12, 16, 24, 32, 40, 48, 72 hr.

Sample Preparation: Cell pellets were lysed in protein (RIPA) lysis buffer (10mM Tris-Cl pH 8.0; 1.5mM EDTA; 1% Triton X-100; 0.1% SDS; 140 mM NaCl; 0.1% sodium deoxycholate; phosphatase and protease inhibitor cocktails (ThermoFisher Scientific)). Lysates were incubated on ice for 30min, sonicated for 10 seconds at 40% amplitude, and centrifuged at 14000 rcf for 10 minutes at 4°C. The supernatant was collected, and protein concentration was determined using Pierce BCA Protein Assay Kit (ThermoFisher Scientific) and a Molecular Devices SpectraMax iD3. A total of 30μg of protein was reduced with TCEP (ThermoFisher Scientific) to a concentration of 10mM and alkylated with IAA (Sigma) to a concentration of 30mM. Peptides underwent chloroform/methanol extraction (Fisher Chemical) and digested overnight at 47°C with sequencing grade modified porcine trypsin (Promega) in Triethylammonium bicarbonate (TEAB, Honeywell Fluka) at a protein:trypsin ratio of 50:1. The following day, samples were acidified to 0.5% formic acid/0.1% trifluoroacetic acid (TFA, Fisher Chemical). After plate equilibration with Buffer B, tryptic peptides were loaded onto a Sep-Pak C18 96-well plate (Waters) to be desalted using a Resolvex A200 (Tecan) automated method where samples underwent four washes with Buffer A. Peptides were eluted from the plate using 40% Buffer B. After equilibrating the plate with 70% Buffer B, samples were filtered using an AcroPrep Advance Filter Plate (Pall). Samples were lyophilized overnight (SpeedVac SPD210, ThermoFisher Scientific) and stored at −80°C. Buffer A = 0.1% formic acid, 0.5% acetonitrile in water, Buffer B = 80% acetonitrile, 20% water, 0.1% formic acid.

Analysis: SILAC LC-MS analysis was conducted using an EvoSep One (EvoSep) coupled to a trapped ion mobility spectrometry quadrupole time-of-flight mass spectrometer (timsTOF Pro, Bruker Daltonik) by a captive spray ion source (Bruker Daltonik). Tryptic peptides were reconstituted in Buffer A. 500 ng of sample was loaded on C18 Evotips (Evosep) according to the manufacturer's protocol. Peptides were separated on a 15cm × 150μm ReproSil-pur C18 Endurance analytical column with 1.9 μm beads (EvoSep) at 50°C using a linear 44 min gradient 30 SPD method (Evosep). Mass spectrometry analysis was performed in data-independent (dia-PASEF) mode with 1 MS1 survey TIMS-MS and 10 PASEF MS/MS scans per acquisition cycle. The captive spray ion source capillary voltage was set to 1650 V. Both the ramp time and ion accumulation time were set to 100.0 ms. The ion mobility ranged from 1/K0 = 0.85 to 1.27 $V{\cdot}s/cm^2$, excluding singly or triply charged precursor ions. Full scan mass ranged from 100 to 1700 m/z. Collision energy was decreased linearly with increasing mobility, starting from 59 eV at 1/K0 = 1.6 $V{\cdot}s/cm^2$ and reducing to 20 eV at 1/K0 = 0.6 $V{\cdot}s/cm^2$.

Data Processing: Raw files acquired from abundance LC-MS analysis were analyzed with Spectronaut software (version 18.2) using the directDIA method with MS2 scans used for protein and peptide quantification. The UniProt murine proteome reference (Mouse_UP000000589_10090) containing 21,756 protein entries was used with protein and peptide-level false discovery rates (FDR) set to 0.01. Selected variable modifications included N-terminal acetylation and methionine oxidation while cysteine carbamidomethylation was set as a fixed modification. Trypsin was selected as the digestion enzyme with a maximum of two allowed missed cleavages and a minimum peptide length of seven amino acids. A total of 90,392 peptides and 7,520 protein groups were

identified. Protein MS2 exclusive intensity values were quality-assessed using ProteiNorm [111]. Data normalization was performed with Variance Stabilizing Normalization (VSN)[112], followed by statistical analysis using proteoDA[113]. Linear Models for Microarray Data (limma) combined with empirical Bayes (eBayes) smoothing were applied to the standard errors[107]. Proteins with a false discovery rate (FDR)-adjusted p-value of less than 0.05 were considered statistically significant.

Raw files acquired from SILAC LC-MS analysis were analyzed with Spectronaut software (version 20.3). Using the Pulsar search engine, a DIA-based spectral library was created using the “Generate Library from Pulsar/Search Archives” function. The UniProt murine proteome reference (Mouse_UP000000589_10090) containing 21,756 protein entries was used with protein and peptide-level false discovery rates (FDR) set to 0.01. Selected variable modifications included N-terminal acetylation and methionine oxidation while cysteine carbamidomethylation was set as a fixed modification. Trypsin was selected as the digestion enzyme with a maximum of two allowed missed cleavages and a minimum peptide length of seven amino acids. To ensure robust filtering in multiplexed SILAC DIA data, the Multi Channel Q-value Filter was set to “Channel Qvalue,” enforcing channel-specific confidence estimation. A total of 92,824 peptides and 7,604 protein groups were identified . A labeled spectral library was then generated, utilizing two label channels with Arg10 and Lys8 modifications added to the second channel. Raw files were searched using the labeled spectral library with MS2 scans used for protein and peptide quantification and half-life determination.

Protein half-life determination: The statistical software R (v4.4.3) was used to calculate protein half-life. Peptide-level quantification were processed to compute the percentage of light-labeled peptides and organized by protein, gene, condition, replicate. Peptides were filtered to include only those that contained at least 11 timepoints between 0 and 72 hours and excluding those with an increasing light fraction over time (suggesting incomplete labeling or biological noise). Using the fitdecay1 function from the R package nlfitr (v0.1.0) a non-linear leas squares (NLS) decay model was fit for each peptide time course, with upper and lower asymptotes fixed at 1 and 0 respectively, and weighted fitting enabled. The R package broom (v1.0.7) was used to extract the model output. Peptides with valid model fits were evaluated for goodness-of-fit by calculating pseudo and adjusted R-squared values. Only peptides with an adjusted R-squared ≥ 0.9 were retained. These peptides were averaged across proteins to compute mean percent light curves that were re-fit using the same NLS procedure to obtain protein-label kinetic parameters. The decay constant (k) was converted to half-life for each protein and condition (half-life = log2(k)).

Short-Lived Protein Abundance Analysis: To compare the abundance of short-lived (half-life ≤8 h) versus non-short-lived (half-life >8 h to ≤20 h) proteins across T cell populations, protein annotations for short-lived proteins were curated into a list using half-life quantification from either of the two replicates. Then protein intensity values obtained from the DIA-PASEF dataset were used to evaluate the abundance of short-lived proteins across T cell populations. Proteins were annotated as “short-lived” or “non-short-lived” based on curated list. Intensities were summed for each protein within a sample. For

each biological replicate, the total abundance was computed as the sum of intensities for all detected proteins within each category. Mean abundance and standard error were calculated across replicates using the dplyr package. Visualization of group-wise means and significance was performed with ggplot2 and ggpubr, using bar plots with error bars and annotated *p*-values. For rank–abundance analysis, each T cell population was converted from protein intensities to within-sample proportions, averaged these across replicates, and ranked proteins by mean proportional contribution to plot faceted rank–abundance curves (implemented in R with dplyr, tidyr, and ggplot2). For stacked composition plots, the top 20 proteins per population were visualized (and the remaining collapsed as "Other") as 100% stacked bars with ordered fills (implemented with dplyr, forcats, ggplot2, and scales). For Protein Set Enrichment Analysis, peptide-count matrices values were log2-transformed (log2[count+1]) in R. Pairwise differential ranking statistics between group.type levels were computed using limma (linear modeling with empirical Bayes moderation), and a short-lived proteins set was tested for enrichment against the ranked t-statistics using fgsea (fgseaMultilevel). GSEA-style running enrichment score plots were generated with ggplot2.

Quantitative and Statistical Methods

Statistical tests were performed using Prism (7.0/9.0; GraphPad), R (v.4.1), and Python (3.11.9) in VS Code software packages. Two-tailed, paired or unpaired Student's *t*-tests, or one- or two-way analyses of variance (ANOVA) were used for comparisons between groups. *P*-values <0.05 were considered statistically significant. Values of $P < 0.05$ were ranked as follows: *, $P < 0.05$; **, $P < 0.01$; ***, $P < 0.001$; and ****, $P < 0.0001$.

Supplementary Material

Refer to Web version on PubMed Central for supplementary material.

Acknowledgments:

We would like to thank the Goldrath lab and other co-authors for manuscript review. We thank the La Jolla Institute for Immunology Flow Cytometry Core facility and staff for their sorting assistance. We also thank the ImmGen consortium and ImmGenT team including David Zemmour and Ian Magill for their expertise and assistance with the pan-tissue scRNA-seq experiments. This work was performed in the context of the ImmGenT project within the ImmGen consortium, supported by R24072073. This work was supported by National Institutes of Health grants K00CA222711 (N.E.S.), GM133351 (A.R.), F31AI176705 (K.K.T), DP5OD031863 (B.K.), R35GM148339 (E.J.B.), R21AI178362 (A.W.G.), R01AI179952 (A.W.G.), R37AI067545 (A.W.G.), R01AI072117 (A.W.G.), and R01AI150282 (A.W.G.).

Declaration of interests:

A.F. is a co-founder, CEO and board member of TCura Bioscience. A.W.G. is a co-founder of TCura Bioscience, Inc. and serves on the scientific advisory board of Foundery Biosciences and is a Senior Advisor to the Allen Institute for Immunology.

References:

1. Taniuchi I. (2018). CD4 Helper and CD8 Cytotoxic T Cell Differentiation. Annu. Rev. Immunol 36, 579–601. 10.1146/annurev-immunol-042617-053411. [PubMed: 29677476]
2. McLane LM, Abdel-Hakeem MS, and Wherry EJ (2019). CD8 T Cell Exhaustion During Chronic Viral Infection and Cancer. Annu. Rev. Immunol 37, 457–495. 10.1146/annurev-immunol-041015-055318. [PubMed: 30676822]

3. Miller BC, Sen DR, Al Abosy R, Bi K, Virkud YV, LaFleur MW, Yates KB, Lako A, Felt K, Naik GS, et al. (2019). Subsets of exhausted CD8+ T cells differentially mediate tumor control and respond to checkpoint blockade. Nat. Immunol 20, 326–336. 10.1038/s41590-019-0312-6. [PubMed: 30778252]
4. Blank CU, Haining WN, Held W, Hogan PG, Kallies A, Lugli E, Lynn RC, Philip M, Rao A, Restifo NP, et al. Defining 'T cell exhaustion.' Nat. Rev. Immunol 10.1038/s41577-019-0221-9.
5. Reina-Campos M, Scharping NE, and Goldrath AW (2021). CD8+ T cell metabolism in infection and cancer. Preprint at Nature Research, 10.1038/s41577-02100537-8 https://doi.org/10.1038/s41577-021-00537-8.
6. Belk JA, Daniel B, and Satpathy AT (2022). Epigenetic regulation of T cell exhaustion. Preprint at Nature Research, 10.1038/s41590-022-01224-z https://doi.org/10.1038/s41590-022-01224-z.
7. Huang YJ, Ngiow SF, Baxter AE, Manne S, Park SL, Wu JE, Khan O, Giles JR, and Wherry EJ (2025). Continuous expression of TOX safeguards exhausted CD8 T cell epigenetic fate.
8. Heeg M, and Goldrath AW (2023). Insights into phenotypic and functional CD8+ TRM heterogeneity. Preprint at John Wiley and Sons Inc, 10.1111/imr.13218 https://doi.org/10.1111/imr.13218.
9. Okła K, Farber DL, and Zou W. (2021). Tissue-resident memory T cells in tumor immunity and immunotherapy. Journal of Experimental Medicine 218, e20201605. 10.1084/jem.20201605.
10. Milner JJ, Toma C, Yu B, Zhang K, Omilusik K, Phan AT, Wang D, Getzler AJ, Nguyen T, Crotty S, et al. (2017). Runx3 programs CD8+ T cell residency in non-lymphoid tissues and tumours. Nature 552, 253–257. 10.1038/nature24993. [PubMed: 29211713]
11. Reina-Campos M, Heeg M, Kennewick K, Mathews IT, Galletti G, Luna V, Nguyen Q, Huang H, Milner JJ, Hu KH, et al. (2023). Metabolic programs of T cell tissue residency empower tumour immunity. Nature 621, 179–187. 10.1038/s41586-023-06483-w. [PubMed: 37648857]
12. Liikanen I, Lauhan C, Quon S, Omilusik K, Phan AT, Bartrolí LB, Ferry A, Goulding J, Chen J, Scott-Browne JP, et al. (2021). Hypoxia-inducible factor activity promotes antitumor effector function and tissue residency by CD8+ T cells. J. Clin. Invest 131. 10.1172/JCI143729.
13. Anadon CM, Yu X, Hänggi K, Biswas S, Chaurio RA, Martin A, Payne KK, Mandal G, Innamarato P, Harro CM, et al. (2022). Ovarian cancer immunogenicity is governed by a narrow subset of progenitor tissue-resident memory T cells. Cancer Cell 40, 545–557.e13. 10.1016/j.ccell.2022.03.008. [PubMed: 35427494]
14. Schröter F, and Adjaye J. (2014). The proteasome complex and the maintenance of pluripotency: sustain the fate by mopping up? Stem Cell Res. Ther 5, 24. 10.1186/scrt413. [PubMed: 25127410]
15. Cruz Walma DA, Chen Z, Bullock AN, and Yamada KM (2022). Ubiquitin ligases: guardians of mammalian development. Preprint at Nature Research, 10.1038/s41580-021-00448-5 https://doi.org/10.1038/s41580-021-00448-5.
16. Pohl C, and Dikic I. (2019). Cellular quality control by the ubiquitin-proteasome system and autophagy. Science (1979). 366, 818–822. 10.1126/science.aax3769.
17. Kerr SR, and Katz SG (2019). Activation of the Unfolded Protein Response Pathway in Cytotoxic T Cells: A Comparison Between in vitro Stimulation, Infection, and the Tumor Microenvironment. Yale J. Biol. Med 92, 675–685. [PubMed: 31866782]
18. Di Conza G, Ho PC, Cubillos-Ruiz JR, and Huang SCC (2023). Control of immune cell function by the unfolded protein response. Preprint at Nature Research, 10.1038/s41577-023-00838-0 https://doi.org/10.1038/s41577-023-00838-0.
19. Sheng X, Xia Z, Yang H, and Hu R. (2024). The ubiquitin codes in cellular stress responses. Preprint at Oxford University Press, 10.1093/procel/pwad045 https://doi.org/10.1093/procel/pwad045.
20. Hetz C, and Saxena S. (2017). ER stress and the unfolded protein response in neurodegeneration. Preprint at Nature Publishing Group, 10.1038/nrneurol.2017.99 https://doi.org/10.1038/nrneurol.2017.99.
21. Marchingo JM, and Cantrell DA (2022). Protein synthesis, degradation, and energy metabolism in T cell immunity. Cell. Mol. Immunol 19, 303–315. 10.1038/s41423-021-00792-8. [PubMed: 34983947]

22. Marchingo JM, Sinclair LV, Howden AJM, and Cantrell DA (2020). Quantitative analysis of how Myc controls T cell proteomes and metabolic pathways during T cell activation. Elife 9, e53725. 10.7554/eLife.53725.

23. Tan H, Yang K, Li Y, Shaw TI, Wang Y, Blanco DB, Wang X, Cho JH, Wang H, Rankin S, et al. (2017). Integrative Proteomics and Phosphoproteomics Profiling Reveals Dynamic Signaling Networks and Bioenergetics Pathways Underlying T Cell Activation. Immunity 46, 488–503. 10.1016/j.immuni.2017.02.010. [PubMed: 28285833]

24. Wang X, Luo H, Chen H, Duguid W, and Wu J. (1998). Role of Proteasomes in T Cell Activation and Proliferation. The Journal of Immunology 160, 788. [PubMed: 9551914]

25. Vilchez D, Boyer L, Morantte I, Lutz M, Merkwirth C, Joyce D, Spencer B, Page L, Masliah E, Travis Berggren W, et al. (2012). Increased proteasome activity in human embryonic stem cells is regulated by PSMD11. Nature 489, 304–308. 10.1038/nature11468. [PubMed: 22972301]

26. Cruz Walma DA, Chen Z, Bullock AN, and Yamada KM (2022). Ubiquitin ligases: guardians of mammalian development. Preprint at Nature Research, 10.1038/s41580-021-00448-5 https://doi.org/10.1038/s41580-021-00448-5.

27. Wolf T, Jin W, Zoppi G, Vogel IA, Akhmedov M, Bleck CKE, Beltraminelli T, Rieckmann JC, Ramirez NJ, Benevento M, et al. (2020). Dynamics in protein translation sustaining T cell preparedness. Nat. Immunol 21, 927–937. 10.1038/s41590-020-0714-5. [PubMed: 32632289]

28. Widjaja CE, Olvera JG, Metz PJ, Phan AT, Savas JN, de Bruin G, Leestemaker Y, Berkers CR, de Jong A, Florea BI, et al. (2017). Proteasome activity regulates CD8+ T lymphocyte metabolism and fate specification. J. Clin. Invest 127, 3609–3623. 10.1172/JCI90895. [PubMed: 28846070]

29. Moebius J, Van Den Broek M, Groettrup M, and Basler M. (2010). Immunoproteasomes are essential for survival and expansion of T cells in virus-infected mice. Eur. J. Immunol 40, 3439–3449. 10.1002/eji.201040620. [PubMed: 21108466]

30. Haase VH (2009). The VHL tumor suppressor: master regulator of HIF. Curr. Pharm. Des 15, 3895–3903. 10.2174/138161209789649394. [PubMed: 19671042]

31. Doedens AL, Phan AT, Stradner MH, Fujimoto JK, Nguyen JV, Yang E, Johnson RS, and Goldrath AW (2013). Hypoxia-inducible factors enhance the effector responses of CD8 + T cells to persistent antigen. Nat. Immunol 14, 1173–1182. 10.1038/ni.2714. [PubMed: 24076634]

32. Milner JJ, Toma C, Yu B, Zhang K, Omilusik K, Phan AT, Wang D, Getzler AJ, Nguyen T, Crotty S, et al. (2017). Runx3 programs CD8+ T cell residency in non-lymphoid tissues and tumours. Nature 552, 253–257. 10.1038/nature24993. [PubMed: 29211713]

33. Ford BR, Vignali PDA, Rittenhouse NL, Scharping NE, Peralta R, Lontos K, Frisch AT, Delgoffe GM, and Poholek AC (2022). Tumor microenvironmental signals reshape chromatin landscapes to limit the functional potential of exhausted T cells. Sci. Immunol 7, eabj9123. 10.1126/sciimmunol.abj9123.

34. Liu S, and Boulianne GL (2017). The NHR domains of Neuralized and related proteins: Beyond Notch signalling. Preprint at Elsevier Inc., 10.1016/j.cellsig.2016.10.004 https://doi.org/10.1016/j.cellsig.2016.10.004.

35. Deshaies RJ, and Joazeiro CAP (2009). RING domain E3 ubiquitin ligases. Preprint at Annual Reviews Inc., 10.1146/annurev.biochem.78.101807.093809 https://doi.org/10.1146/annurev.biochem.78.101807.093809.

36. Kile Benjamin T., Schulman Brenda A., Alexander Warren S., Nicola Nicos A., Martin Helene M.E., and Hilton Douglas J. (2002). The SOCS box: a tale of destruction and degradation. Trends Biochem. Sci, 235–241. 10.1016/S0968-0004(02)02085-6. [PubMed: 12076535]

37. Kim JJ, Lee SB, Jang J, Yi S-Y, Kim S-H, Han S-A, Lee J-M, Tong S-Y, Vincelette ND, Gao B, et al. (2015). WSB1 promotes tumor metastasis by inducing pVHL degradation. 10.1101/gad.268128.

38. Escobar G, Tooley K, Oliveras JP, Huang L, Cheng H, Bookstaver ML, Edwards C, Froimchuk E, Xue C, Mangani D, et al. (2023). Tumor immunogenicity dictates reliance on TCF1 in CD8+ T cells for response to immunotherapy. Cancer Cell 41, 1662–1679.e7. 10.1016/j.ccell.2023.08.001. [PubMed: 37625402]

39. Globig AM, Zhao S, Roginsky J, Maltez VI, Guiza J, Avina-Ochoa N, Heeg M, Araujo Hoffmann F, Chaudhary O, Wang J, et al. (2023). The β1-adrenergic receptor links sympathetic nerves to T cell exhaustion. Nature 622, 383–392. 10.1038/s41586-023-06568-6. [PubMed: 37731001]
40. Chen Y, Zander RA, Wu X, Schauder DM, Kasmani MY, Shen J, Zheng S, Burns R, Taparowsky EJ, and Cui W. (2021). BATF regulates progenitor to cytolytic effector CD8+ T cell transition during chronic viral infection. Nat. Immunol 22, 996–1007. 10.1038/s41590-021-00965-7. [PubMed: 34282329]
41. Beltra JC, Manne S, Abdel-Hakeem MS, Kurachi M, Giles JR, Chen Z, Casella V, Ngiow SF, Khan O, Huang YJ, et al. (2020). Developmental Relationships of Four Exhausted CD8+ T Cell Subsets Reveals Underlying Transcriptional and Epigenetic Landscape Control Mechanisms. Immunity 52, 825–841.e8. 10.1016/j.immuni.2020.04.014. [PubMed: 32396847]
42. Werner A, Manford AG, and Rape M. (2017). Ubiquitin-Dependent Regulation of Stem Cell Biology. Preprint at Elsevier Ltd, 10.1016/j.tcb.2017.04.002 https://doi.org/10.1016/j.tcb.2017.04.002.
43. Liu Y, Beyer A, and Aebersold R. (2016). On the Dependency of Cellular Protein Levels on mRNA Abundance. Preprint at Cell Press, 10.1016/j.cell.2016.03.014 https://doi.org/10.1016/j.cell.2016.03.014.
44. Hukelmann JL, Anderson KE, Sinclair LV, Grzes KM, Murillo AB, Hawkins PT, Stephens LR, Lamond AI, and Cantrell DA (2016). The cytotoxic T cell proteome and its shaping by the kinase mTOR. Nat. Immunol 17, 104–112. 10.1038/ni.3314. [PubMed: 26551880]
45. Myers SA, Rhoads A, Cocco AR, Peckner R, Haber AL, Schweitzer LD, Krug K, Mani DR, Clauser KR, Rozenblatt-Rosen O, et al. (2019). Streamlined protocol for deep proteomic profiling of FAC-sorted cells and its application to freshly isolated murine immune cells. Molecular and Cellular Proteomics 18, 995–1009. 10.1074/mcp.RA118.001259. [PubMed: 30792265]
46. Wang Y, Ma A, Song NJ, Shannon AE, Amankwah YS, Chen X, Wu W, Wang Z, Saadey AA, Yousif A, et al. (2025). Proteotoxic stress response drives T cell exhaustion and immune evasion. Nature. 10.1038/s41586-025-09539-1.
47. Asada N, Ginsberg P, Paust H-J, Song N, Riedel J-H, Turner J-E, Peters A, Kaffke A, Engesser J, Wang H, et al. (2025). The integrated stress response pathway controls cytokine production in tissue-resident memory CD4+ T cells. Nat. Immunol 26, 557–566. 10.1038/s41590-025-02105-x. [PubMed: 40050432]
48. Menk AV, Scharping NE, Moreci RS, Zeng X, Guy C, Salvatore S, Bae H, Xie J, Young HA, Wendell SG, et al. (2018). Early TCR Signaling Induces Rapid Aerobic Glycolysis Enabling Distinct Acute T Cell Effector Functions. Cell Rep. 22. 10.1016/j.celrep.2018.01.040.
49. Dupré L, Boztug K, and Pfajfer L. (2021). Actin Dynamics at the T Cell Synapse as Revealed by Immune-Related Actinopathies. Preprint at Frontiers Media S.A., 10.3389/fcell.2021.665519 https://doi.org/10.3389/fcell.2021.665519.
50. Dupré L, Houmadi R, Tang C, and Rey-Barroso J. (2015). T lymphocyte migration: An action movie starring the actin and associated actors. Preprint at Frontiers Research Foundation, 10.3389/fimmu.2015.00586 https://doi.org/10.3389/fimmu.2015.00586.
51. van de Wall S, Anthony SM, Hancox LS, Pewe LL, Langlois RA, Zehn D, Badovinac VP, and Harty JT (2024). Dynamic landscapes and protective immunity coordinated by influenza-specific lung-resident memory CD8+ T cells revealed by intravital imaging. Immunity 57, 1878–1892.e5. 10.1016/j.immuni.2024.06.016. [PubMed: 39043185]
52. Pan Y, Tian T, Park CO, Lofftus SY, Mei S, Liu X, Luo C, O'Malley JT, Gehad A, Teague JE, et al. (2017). Survival of tissue-resident memory T cells requires exogenous lipid uptake and metabolism. Nature 543, 252. [PubMed: 28219080]
53. Scharping NE, Menk AV, Moreci RS, Whetstone RD, Dadey RE, Watkins SC, Ferris RL, and Delgoffe GM (2016). The Tumor Microenvironment Represses T Cell Mitochondrial Biogenesis to Drive Intratumoral T Cell Metabolic Insufficiency and Dysfunction. Immunity 45, 374–388. 10.1016/j.immuni.2016.07.009. [PubMed: 27496732]
54. Song M, Sandoval TA, Chae C-S, Chopra S, Tan C, Rutkowski MR, Raundhal M, Chaurio RA, Payne KK, Konrad C, et al. (2018). IRE1α-XBP1 controls T cell function in ovarian cancer by regulating mitochondrial activity. Nature 562, 423–428. 10.1038/s41586-018-0597-x. [PubMed: 30305738]

55. Ma X, Bi E, Lu Y, Su P, Huang C, Liu L, Wang Q, Yang M, Kalady MF, Qian J, et al. (2019). Cholesterol Induces CD8(+) T Cell Exhaustion in the Tumor Microenvironment. Cell Metab. 30, 143–156.e5. 10.1016/j.cmet.2019.04.002. [PubMed: 31031094]
56. Cao Y, Trillo-Tinoco J, Sierra RA, Anadon C, Dai W, Mohamed E, Cen L, Costich TL, Magliocco A, Marchion D, et al. (2019). ER stress-induced mediator C/EBP homologous protein thwarts effector T cell activity in tumors through T-bet repression. Nat. Commun 10. 10.1038/s41467-019-09263-1.
57. Hurst KE, Lawrence KA, Essman MT, Walton ZJ, Leddy LR, and Thaxton JE (2019). Endoplasmic Reticulum Stress Contributes to Mitochondrial Exhaustion of CD8+ T Cells. Cancer Immunol. Res 7, 476 LP – 486. 10.1158/2326-6066.CIR-18-0182. [PubMed: 30659052]
58. Shen D, Coleman J, Chan E, Nicholson TP, Dai L, Sheppard PW, and Patton WF (2011). Novel Cell- and Tissue-Based Assays for Detecting Misfolded and Aggregated Protein Accumulation Within Aggresomes and Inclusion Bodies. Cell Biochem. Biophys 60, 173–185. 10.1007/s12013-010-9138-4. [PubMed: 21132543]
59. Enenkel C, and Ernst OP (2025). Proteasome dynamics in response to metabolic changes. Preprint at Frontiers Media SA, 10.3389/fcell.2025.1523382 https://doi.org/10.3389/fcell.2025.1523382.
60. Sade-Feldman M, Yizhak K, Bjorgaard SL, Ray JP, de Boer CG, Jenkins RW, Lieb DJ, Chen JH, Frederick DT, Barzily-Rokni M, et al. (2018). Defining T Cell States Associated with Response to Checkpoint Immunotherapy in Melanoma. Cell 175, 998–1013.e20. 10.1016/j.cell.2018.10.038. [PubMed: 30388456]
61. Liu D, Schilling B, Liu D, Sucker A, Livingstone E, Jerby-Amon L, Zimmer L, Gutzmer R, Satzger I, Loquai C, et al. (2019). Integrative molecular and clinical modeling of clinical outcomes to PD1 blockade in patients with metastatic melanoma. Nat. Med 25, 1916–1927. 10.1038/s41591-019-0654-5. [PubMed: 31792460]
62. Chapman NM, Boothby MR, and Chi H. (2020). Metabolic coordination of T cell quiescence and activation. Preprint at Nature Research, 10.1038/s41577019-0203-y https://doi.org/10.1038/s41577-019-0203-y.
63. de Morree A, and Rando TA (2023). Regulation of adult stem cell quiescence and its functions in the maintenance of tissue integrity. Preprint at Nature Research, 10.1038/s41580-022-00568-6 https://doi.org/10.1038/s41580-022-00568-6.
64. Kaitsuka T, and Hakim F. (2021). Response of pluripotent stem cells to environmental stress and its application for directed differentiation. Preprint at MDPI AG, https://doi.org/10.3390/biology10020084 10.3390/biology10020084.
65. Zhou SQ, Feng P, Ye ML, Huang SY, He SW, Zhu XH, Chen J, Zhang Q, and Li YQ (2024). The E3 ligase NEURL3 suppresses epithelial-mesenchymal transition and metastasis in nasopharyngeal carcinoma by promoting vimentin degradation. Journal of Experimental and Clinical Cancer Research 43. 10.1186/s13046-024-02945-9.
66. Hong S-W, Jin D-H, Shin J-S, Moon J-H, Na Y-S, Jung K-A, Kim S-M, Kim JC, Kim K, Hong YS, et al. (2012). Ring Finger Protein 149 Is an E3 Ubiquitin Ligase Active on Wild-type v-Raf Murine Sarcoma Viral Oncogene Homolog B1 (BRAF)*. Journal of Biological Chemistry 287, 24017–24025. 10.1074/jbc.M111.319822. [PubMed: 22628551]
67. Legesse A, Kaushansky N, Braunstein I, Saad H, Lederkremer G, Navon A, and Stanhill A. (2023). The role of RNF149 in the pre-emptive quality control substrate ubiquitination. Commun. Biol 6. 10.1038/s42003-023-04763-9.
68. Jin X, Liu J, Wang W, Li J, Liu G, Qiu R, Yang M, Liu M, Yang L, Du X, et al. (2022). Identification of age-associated proteins and functional alterations in human retinal pigment epithelium. Genomics Proteomics Bioinformatics. 10.1016/j.gpb.2022.06.001.
69. Kim JJ, Lee SB, Jang J, Yi S-Y, Kim S-H, Han S-A, Lee J-M, Tong S-Y, Vincelette ND, Gao B, et al. (2015). WSB1 promotes tumor metastasis by inducing pVHL degradation. Genes Dev. 29, 2244–2257. [PubMed: 26545811]
70. Kim JJ, Lee SB, Yi S-Y, Han S-A, Kim S-H, Lee J-M, Tong S-Y, Yin P, Gao B, Zhang J, et al. (2017). WSB1 overcomes oncogene-induced senescence by targeting ATM for degradation. Cell Res. 27, 274–293. 10.1038/cr.2016.148. [PubMed: 27958289]

71. Cao J, Wang Y, Dong R, Lin G, Zhang N, Wang J, Lin N, Gu Y, Ding L, Ying M, et al. (2015). Hypoxia-Induced WSB1 Promotes the Metastatic Potential of Osteosarcoma Cells. Cancer Res. 75, 4839–4851. 10.1158/0008-5472.CAN-15-0711. [PubMed: 26424695]
72. Nucifora FC, Nucifora LG, Ng C-H, Arbez N, Guo Y, Roby E, Shani V, Engelender S, Wei D, Wang X-F, et al. (2016). Ubiqutination via K27 and K29 chains signals aggregation and neuronal protection of LRRK2 by WSB1. Nat. Commun 7, 11792. 10.1038/ncomms11792. [PubMed: 27273569]
73. Poujade F-A, Mannion A, Brittain N, Theodosi A, Beeby E, Leszczynska KB, Hammond EM, Greenman J, Cawthorne C, and Pires IM (2018). WSB-1 regulates the metastatic potential of hormone receptor negative breast cancer. Br. J. Cancer 118, 1229–1237. 10.1038/s41416-018-0056-3. [PubMed: 29540773]
74. Barroso-Gomila O, Merino-Cacho L, Muratore V, Perez C, Taibi V, Maspero E, Azkargorta M, Iloro I, Trulsson F, Vertegaal ACO, et al. (2023). BioE3 identifies specific substrates of ubiquitin E3 ligases. Nat. Commun 14. 10.1038/s41467-023-43326-8.
75. Yamanaka S, Horiuchi Y, Matsuoka S, Kido K, Nishino K, Maeno M, Shibata N, Kosako H, and Sawasaki T. (2022). A proximity biotinylation-based approach to identify protein-E3 ligase interactions induced by PROTACs and molecular glues. Nat. Commun 13. 10.1038/s41467-021-27818-z.
76. Brenes AJ, Lamond AI, and Cantrell DA (2023). The Immunological Proteome Resource. Preprint at Nature Research, 10.1038/s41590-023-01483-4 https://doi.org/10.1038/s41590-023-01483-4.
77. Chu Y, Dai E, Li Y, Han G, Pei G, Ingram DR, Thakkar K, Qin JJ, Dang M, Le X, et al. (2023). Pan-cancer T cell atlas links a cellular stress response state to immunotherapy resistance. Nat. Med 29, 1550–1562. 10.1038/s41591-023-02371-y. [PubMed: 37248301]
78. Crowl JT, Heeg M, Ferry A, Milner JJ, Omilusik KD, Toma C, He Z, Chang JT, and Goldrath AW (2022). Tissue-resident memory CD8+ T cells possess unique transcriptional, epigenetic and functional adaptations to different tissue environments. Nat. Immunol 23, 1121–1131. 10.1038/s41590-022-01229-8. [PubMed: 35761084]
79. Fu J, Li K, Zhang W, Wan C, Zhang J, Jiang P, and Liu XS (2020). Large-scale public data reuse to model immunotherapy response and resistance. Genome Med. 12. 10.1186/s13073-020-0721-z.
80. Kurd NS, He Z, Louis TL, Milner JJ, Omilusik KD, Jin W, Tsai MS, Widjaja CE, Kanbar JN, Olvera JG, et al. (2020). Early precursors and molecular determinants of tissue-resident memory CD8 + T lymphocytes revealed by single-cell RNA sequencing.
81. Scharping NE, Rivadeneira DB, Menk AV, Vignali PDA, Ford BR, Rittenhouse NL, Peralta R, Wang Y, Wang Y, DePeaux K, et al. (2021). Mitochondrial stress induced by continuous stimulation under hypoxia rapidly drives T cell exhaustion. Nat. Immunol 22, 205–215. 10.1038/s41590-020-00834-9. [PubMed: 33398183]
82. Miller BC, Sen DR, Al Abosy R, Bi K, Virkud YV, LaFleur MW, Yates KB, Lako A, Felt K, Naik GS, et al. (2019). Subsets of exhausted CD8+ T cells differentially mediate tumor control and respond to checkpoint blockade. Nat. Immunol 20, 326–336. 10.1038/s41590-019-0312-6. [PubMed: 30778252]
83. Ron-Harel N, Ghergurovich JM, Notarangelo G, LaFleur MW, Tsubosaka Y, Sharpe AH, Rabinowitz JD, and Haigis MC (2019). T Cell Activation Depends on Extracellular Alanine. Cell Rep. 28, 3011–3021.e4. 10.1016/j.celrep.2019.08.034. [PubMed: 31533027]
84. Nüssing S, House IG, Kearney CJ, Chen AXY, Vervoort SJ, Beavis PA, Oliaro J, Johnstone RW, Trapani JA, and Parish IA (2020). Efficient CRISPR/Cas9 Gene Editing in Uncultured Naive Mouse T Cells for In Vivo Studies. The Journal of Immunology 204, 2308–2315. 10.4049/jimmunol.1901396. [PubMed: 32152070]
85. Seki A, and Rutz S. (2018). Optimized RNP transfection for highly efficient CRISPR/Cas9-mediated gene knockout in primary T cells. Journal of Experimental Medicine 215, 985–997. 10.1084/jem.20171626. [PubMed: 29436394]
86. Bernstein NJ, Fong NL, Lam I, Roy MA, Hendrickson DG, and Kelley DR (2020). Solo: Doublet Identification in Single-Cell RNA-Seq via Semi-Supervised Deep Learning. Cell Syst. 11, 95–101.e5. 10.1016/j.cels.2020.05.010. [PubMed: 32592658]

87. Mulè MP, Martins AJ, and Tsang JS (2022). Normalizing and denoising protein expression data from droplet-based single cell profiling. Nat. Commun 13. 10.1038/s41467-022-29356-8.

88. Wolf FA, Angerer P, and Theis FJ (2018). SCANPY: Large-scale single-cell gene expression data analysis. Genome Biol. 19. 10.1186/s13059-017-1382-0.

89. Hafemeister C, and Satija R. (2019). Normalization and variance stabilization of single-cell RNA-seq data using regularized negative binomial regression. Genome Biol. 20. 10.1186/s13059-019-1874-1.

90. Gayoso A, Lopez R, Xing G, Boyeau P, Valiollah Pour Amiri V, Hong J, Wu K, Jayasuriya M, Mehlman E, Langevin M, et al. (2022). A Python library for probabilistic analysis of single-cell omics data. Preprint at Nature Research, 10.1038/s41587-021-01206-w https://doi.org/10.1038/s41587-021-01206w.

91. Traag VA, Waltman L, and van Eck NJ (2019). From Louvain to Leiden: guaranteeing well-connected communities. Sci. Rep 9. 10.1038/s41598-019-41695-z.

92. Kuleshov MV, Jones MR, Rouillard AD, Fernandez NF, Duan Q, Wang Z, Koplev S, Jenkins SL, Jagodnik KM, Lachmann A, et al. (2016). Enrichr: a comprehensive gene set enrichment analysis web server 2016 update. Nucleic Acids Res. 44, W90–W97. 10.1093/nar/gkw377. [PubMed: 27141961]

93. Fang Z, Liu X, and Peltz G. (2023). GSEApy: a comprehensive package for performing gene set enrichment analysis in Python. Bioinformatics 39. 10.1093/bioinformatics/btac757.

94. Hunter John D. (2007). Matplotlib: A 2D Graphics Environment. IEEE.

95. Waskom M. (2021). seaborn: statistical data visualization. J. Open Source Softw 6, 3021. 10.21105/joss.03021.

96. Weinberger E, Lin C, and Lee SI (2023). Isolating salient variations of interest in single-cell data with contrastiveVI. Nat. Methods 20, 1336–1345. 10.1038/s41592-023-01955-3. [PubMed: 37550579]

97. Bolger AM, Lohse M, and Usadel B. (2014). Trimmomatic: A flexible trimmer for Illumina sequence data. Bioinformatics 30, 2114–2120. 10.1093/bioinformatics/btu170. [PubMed: 24695404]

98. Dobin A, Davis CA, Schlesinger F, Drenkow J, Zaleski C, Jha S, Batut P, Chaisson M, and Gingeras TR (2013). STAR: Ultrafast universal RNA-seq aligner. Bioinformatics 29, 15–21. 10.1093/bioinformatics/bts635. [PubMed: 23104886]

99. Liao Y, Smyth GK, and Shi W. (2014). FeatureCounts: An efficient general purpose program for assigning sequence reads to genomic features. Bioinformatics 30, 923–930. 10.1093/bioinformatics/btt656. [PubMed: 24227677]

100. Love MI, Huber W, and Anders S. (2014). Moderated estimation of fold change and dispersion for RNA-seq data with DESeq2. Genome Biol. 15. 10.1186/s13059-014-0550-8.

101. McInnes L, Healy J, Saul N, and Großberger L. (2018). UMAP: Uniform Manifold Approximation and Projection. J. Open Source Softw 3, 861. 10.21105/joss.00861.

102. van Dijk D, Sharma R, Nainys J, Yim K, Kathail P, Carr AJ, Burdziak C, Moon KR, Chaffer CL, Pattabiraman D, et al. (2018). Recovering Gene Interactions from Single-Cell Data Using Data Diffusion. Cell 174, 716–729.e27. 10.1016/j.cell.2018.05.061. [PubMed: 29961576]

103. Üresin N, Petrosius V, Aragon-Fernandez P, Furtwängler B, Schoof EM, and Porse BT (2024). Unraveling the proteome landscape of mouse hematopoietic stem and progenitor compartment with high sensitivity low-input proteomics. Preprint, 10.1101/2024.05.03.592307 https://doi.org/10.1101/2024.05.03.592307.

104. Meier F, Brunner AD, Frank M, Ha A, Bludau I, Voytik E, Kaspar-Schoenefeld S, Lubeck M, Raether O, Bache N, et al. (2020). diaPASEF: parallel accumulation–serial fragmentation combined with data-independent acquisition. Nat. Methods 17, 1229–1236. 10.1038/s41592-020-00998-0. [PubMed: 33257825]

105. Skowronek P, Thielert M, Voytik E, Tanzer MC, Hansen FM, Willems S, Karayel O, Brunner AD, Meier F, and Mann M. (2022). Rapid and In-Depth Coverage of the (Phospho-) Proteome With Deep Libraries and Optimal Window Design for dia-PASEF. Molecular and Cellular Proteomics 21. 10.1016/j.mcpro.2022.100279.

106. Demichev V, Messner CB, Vernardis SI, Lilley KS, and Ralser M. (2020). DIA-NN: neural networks and interference correction enable deep proteome coverage in high throughput. Nat. Methods 17, 41–44. 10.1038/s41592-019-0638-x. [PubMed: 31768060]

107. Ritchie ME, Phipson B, Wu D, Hu Y, Law CW, Shi W, and Smyth GK (2015). Limma powers differential expression analyses for RNA-sequencing and microarray studies. Nucleic Acids Res. 43, e47. 10.1093/nar/gkv007. [PubMed: 25605792]

108. Yu G, Wang LG, Han Y, and He QY (2012). ClusterProfiler: An R package for comparing biological themes among gene clusters. OMICS 16, 284–287. 10.1089/omi.2011.0118. [PubMed: 22455463]

109. Hänzelmann S, Castelo R, and Guinney J. (2013). GSVA: gene set variation analysis for microarray and RNA-Seq data.

110. Obers A, Poch T, Rodrigues G, Christo SN, Gandolfo LC, Fonseca R, Zaid A, Kuai JEY, Lai H, Zareie P, et al. (2024). Retinoic acid and TGF-β orchestrate organ-specific programs of tissue residency. Immunity. 10.1016/j.immuni.2024.09.015.

111. Graw S, Tang J, Zafar MK, Byrd AK, Bolden C, Peterson EC, and Byrum SD (2020). proteiNorm - A User-Friendly Tool for Normalization and Analysis of TMT and Label-Free Protein Quantification. ACS Omega 5, 25625–25633. 10.1021/acsomega.0c02564. [PubMed: 33073088]

112. Huber W, Von Heydebreck A, Ultmann HS¨, Poustka A, and Vingron M. (2002). Variance stabilization applied to microarray data calibration and to the quantification of differential expression.

113. Thurman TJ, Washam CL, Alkam D, Bird JT, Gies A, Dhusia K II, M.S. R, and Byrum SD (2023). proteoDA: a package for quantitative proteomics. J. Open Source Softw 8, 5184. 10.21105/joss.05184.

Highlights

- T_{RM} and T_{PEX} share expression of proteostasis-related genes
- T_{EX} experience a loss of proteostasis, including an accumulation of unfolded proteins
- *Ex vivo* T cell proteomics reveals biological pathways not reflected in transcriptomes
- E3 ligases rescue proteostasis and improves immunotherapeutic responses to cancer

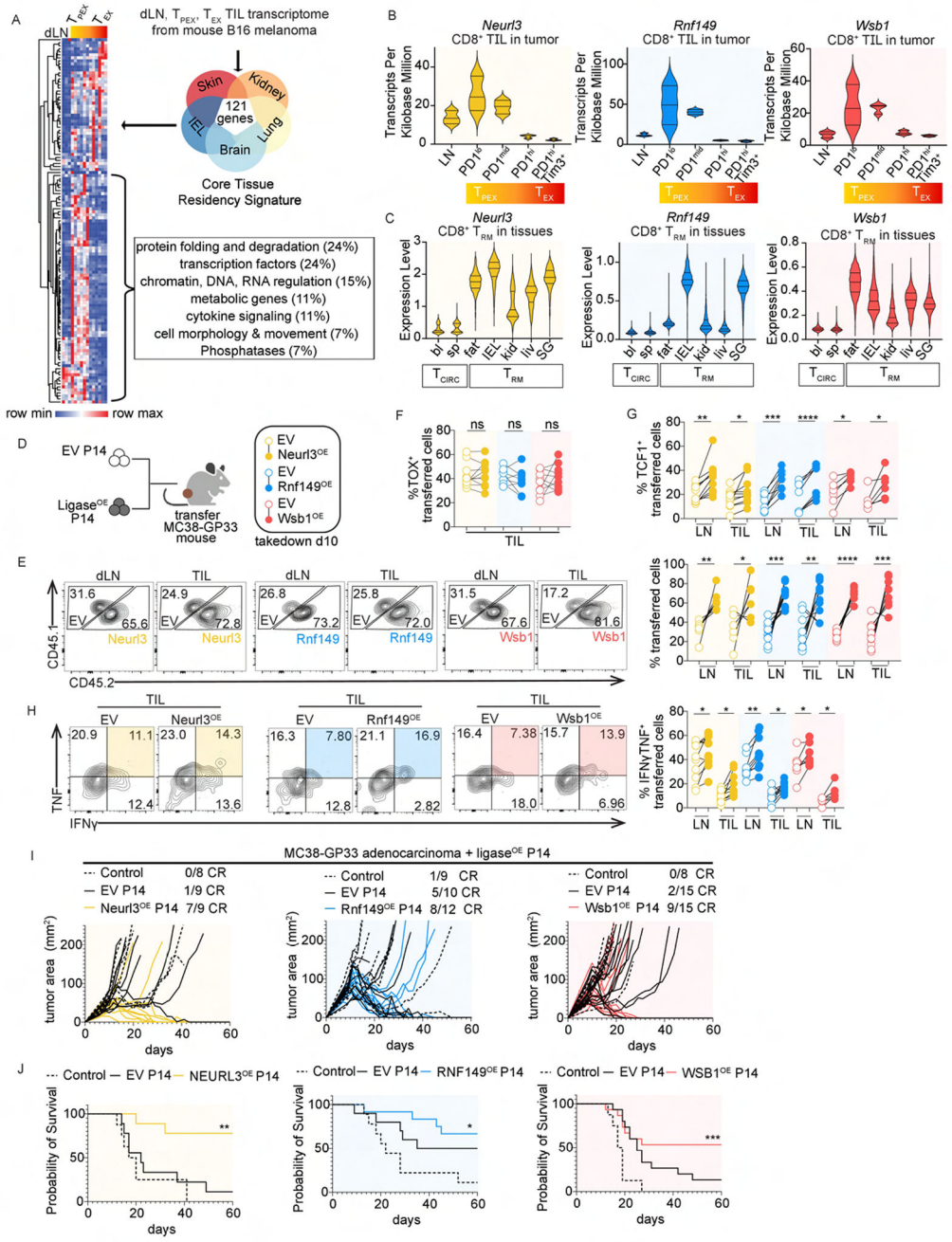

Figure 1: E3 ubiquitin ligases NEURL3, RNF149 and WSB1 are expressed in T_{PEX} and T_{RM}, and sustained expression can rescue TIL function in MC38 adenocarcinoma

A) Heatmap of bulk RNA-seq from endogenous $CD8^+$ T cells sorted from B16 mouse melanoma dLN and TIL (GSE175408[33]). TIL sorted on $PD1^{lo}$, $PD1^{mid}$, $PD1^{hi}$, $PD1^{hi}Tim3^+$, data were filtered using the core T_{RM} gene signature[32] and quantified via hierarchical clustering by rows and columns using one minus Pearson correlation (Supplemental Table 1).

B) *Neurl3*, *Rnf149*, or *Wsb1* RNA TPM (GSE175408[33]).

C) *Neurl3*, *Rnf149*, and *Wsb1* RNA expression levels from scRNA-seq of $CD8^+$ T_{RM} cells isolated from the IEL, kidney, SG, fat and liver, and memory from the spleen and blood (GSE182275[78]), quantified after MAGIC imputation.

D) Experimental schematic: Congenically mismatched P14 T cells were activated, transduced at 24 h with Empty Vector (EV) control or ligase-overexpressing retrovirus ($Neurl3^{OE}$, $Rnf149^{OE}$, or $Wsb1^{OE}$). Next day, cells were sorted on ametrine reporter expression, then cultured for three additional days, mixed 50:50 (250,000 EV + $Ligase^{OE}$; 500,000 total), then transferred into d10 MC38-$GP_{33–41}$-bearing mice; dLN and TIL were analyzed 10 days later (BioRender).

E) Representative flow plots and quantification of transferred P14 T cell frequencies as in D (*Neurl3*^{OE} n=7, *Rnf149*^{OE} n=11, *Wsb1*^{OE} n=10); three independent experiments.

F) Tox^+ P14 T cell frequencies in tumors as in D (*Neurl3*^{OE} n=10, *Rnf149*^{OE} n=8, *Wsb1*^{OE} n=9); three independent experiments.

G) $TCF1^+$ P14 T cell frequencies as in D (*Neurl3*^{OE} n=10, *Rnf149*^{OE} n=8, *Wsb1*^{OE} n=6); two or more independent experiments.

H) Representative flow plots and quantification of $IFN\gamma^+TNF^+$ P14 T cell frequencies as in D followed by 4 h of peptide restimulation plus protein transport inhibitor (*Neurl3*^{OE} n=10, *Rnf149*^{OE} n=8, *Wsb1*^{OE} n=7); three independent experiments.

I) Quantification of MC38-$GP_{33–41}$ tumor area in mice that received no T cells, EV P14 or *Neurl3*^{OE}, *Rnf149*^{OE}, or *Wsb1*^{OE} P14 T cells on d8 after tumor cell implantation. CR = complete regression; two independent experiments.

J) Survival data from I.

Statistical significance was calculated using paired Student's *t*-tests (E-H), or log-rank (Mantel-Cox) test (J). Connecting lines indicate that cells were isolated from the same mouse.

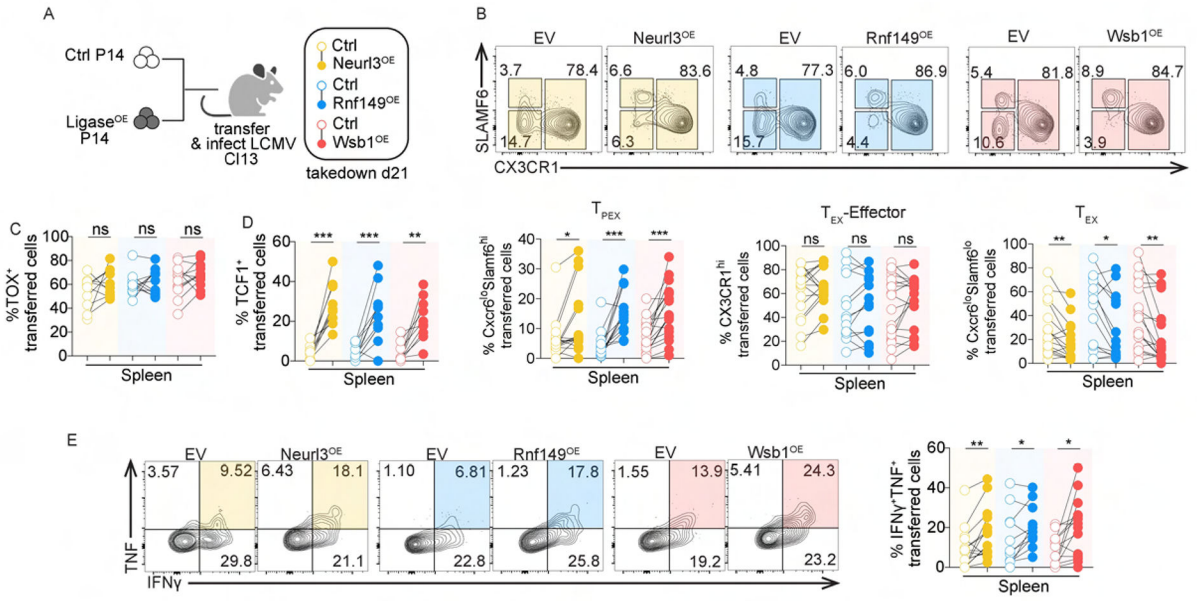

Figure 2: E3 ubiquitin ligases NEURL3, RNF149 and WSB1 expression increases T_{PEX} and decreases T_{EX} frequency in LCMV Cl13 chronic infection

A) Experimental schematic: Congenically mismatched P14 T cells were activated, transduced 24 h later with Empty Vector (EV) or ligase-overexpressing retrovirus (Neurl3^{OE}, Rnf149^{OE}, or Wsb1^{OE}). Next day, cells were sorted on ametrine reporter expression, then EV or Ligase^{OE} cells were mixed 50:50 (1,000 each; 2,000 total) and transferred into recipient mice subsequently infected with LCMV Cl13; spleens were analyzed 21 days later (BioRender).

B) Representative flow plots and quantification of SLAMF6 vs CX3CR1 P14 T cell frequencies as in A. Subsets defined as T_{PEX} (CX3CR1^{lo}SLAMF6^{hi}), T_{EX}-Effector (CX3CR1^{hi}) and T_{EX} (CX3CR1^{lo}SLAMF6^{lo}). (*Neurl3*^{OE} n=16; *Rnf149*^{OE} n=14; *Wsb1*^{OE} n=18); five independent experiments.

C) Quantification of TOX^{+} P14 T cell frequencies as in A (*Neurl3*^{OE} n=10; *Rnf149*^{OE} n=11; *Wsb1*^{OE} n=12); two independent experiments.

D) Quantification of TCF1^{+} P14 T cell frequencies as in A (*Neurl3*^{OE} n=10; *Rnf149*^{OE} n=11; *Wsb1*^{OE} n=10); two independent experiments.

E) Representative flow plots and quantification of TNF^{+}IFNγ^{+} P14 T cell frequencies as in A followed by 4 h of peptide restimulation plus protein transport inhibitor (*Neurl3*^{OE} n=15; *Rnf149*^{OE} n=13; *Wsb1*^{OE} n=17); four independent experiments.

Statistical significance was calculated using (B-E) paired Student's *t*-tests. Connecting lines indicate that cells were isolated from the same mouse.

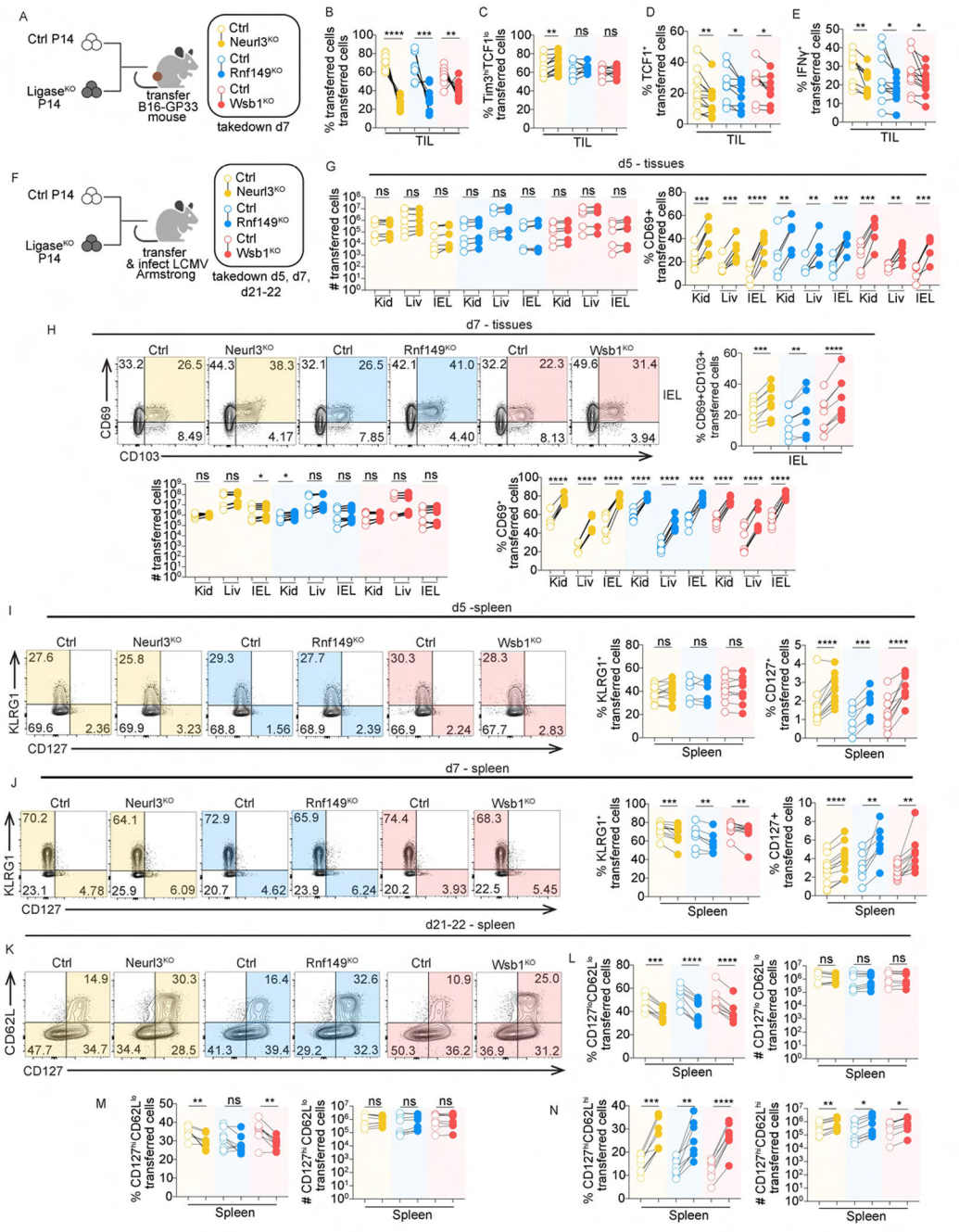

Figure 3: Loss of NEURL3, RNF149, or WSB1 expression accelerates T cell differentiation kinetics

A) Experimental schematic: Congenically mismatched P14 T cells were activated then nucleofected 24 h later with Thy1^{KO} Control CRISPR RNP or ligase^{KO} (Neurl3^{KO}, Rnf149^{KO}, Wsb1^{KO}) plus Thy1^{KO} CRISPR RNP. Cells were cultured to d5–6, mixed 50:50 (1×10^6 each; 2×10^6 total), and transferred into d8 B16-GP$_{33–41}$-bearing mice; dLN and TIL were analyzed 7 days later (BioRender).

B) Quantification of transferred P14 T cell frequencies as in A (*Neurl3*^{KO} n=13; *Rnf149*^{KO} n=12; *Wsb1*^{KO} n=12); three independent experiments.

C) Quantification of $Tim3^{hi}TCF1^{lo}$ P14 T cell frequencies as in A (*Neurl3*^{KO} n=13; *Rnf149*^{KO} n=9; *Wsb1*^{KO} n=9); three independent experiments.

D) Quantification of $TCF1^{+}$ P14 T cell frequencies as in A (*Neurl3*^{KO} n=13; *Rnf149*^{KO} n=9; *Wsb1*^{KO} n=9); three independent experiments.

E) Quantification of $IFN\gamma^{+}$ P14 T cell frequencies as in A followed by 4 h of peptide restimulation plus protein transport inhibitor (*Neurl3*^{KO} n=10; *Rnf149*^{KO} n=11; *Wsb1*^{KO} n=12); three or more independent experiments.

F) Experimental schematic: Congenically mismatched P14 T cells were activated and nucleofected 24 h later with $Thy1^{KO}$ Control CRISPR RNP, or ligase KO (*Neurl3*^{KO}, *Rnf149*^{KO}, *Wsb1*^{KO}) plus $Thy1^{KO}$ CRISPR RNP. EV and ligase^{KO} cells were mixed 50:50 (100,000 each; 200,000 total) and transferred into recipient mice subsequently infected with LCMV Armstrong. At 5 or 7 days, circulating $CD8^{+}$ T cells were IV labeled before sacrifice, and tissues were analyzed (BioRender).

G) Quantification transferred P14 T cell numbers and $CD69^{+}$ frequencies in the kidney, liver, and IEL at day 5 as in F (*Neurl3*^{KO} n=7; *Rnf149*^{KO} n=6; *Wsb1*^{KO} n=6); two independent experiments.

H) (Top left) Representative CD69 vs CD103 flow plot in the IEL; (Top right) $CD69^{+}CD103^{+}$ T cell frequencies in the IEL; (Bottom left) transferred P14 T cell numbers; and (Bottom right) $CD69^{+}$ P14 T cell frequencies in the kidney, liver, and IEL at day 7 as in F (*Neurl3*^{KO} n=7; *Rnf149*^{KO} n=7; *Wsb1*^{KO} n=7); two independent experiments.

I) (Left) Representative KLRG1 vs CD127 flow plot in the spleen; (Right) Splenic $KLRG1^{+}$ or $CD127^{+}$ P14 T cell frequencies at day 5 as in F (*Neurl3*^{KO} n=11; *Rnf149*^{KO} n=6; *Wsb1*^{KO} n=10); two or more independent experiments.

J) (Left) Representative KLRG1 vs CD127 flow plot in the spleen; (Right) splenic $KLRG1^{+}$ or $CD127^{+}$ P14 T cell frequencies at day 7 as in F (*Neurl3*^{KO} n=11; *Rnf149*^{KO} n=7; *Wsb1*^{KO} n=11); two or more independent experiments.

K) Representative splenic P14 CD62L vs CD127 flow plots at 21–22 days as in F.

L) Frequencies and cell numbers of splenic $CD127^{lo}CD62L^{lo}$ P14 T cells at day 21–22 as in F (*Neurl3*^{KO} n=8; *Rnf149*^{KO} n=8; *Wsb1*^{KO} n=8); two independent experiments.

M) Frequencies and cell numbers of splenic $CD127^{hi}CD62L^{lo}$ P14 T cells at day 21–22 as in F (*Neurl3*^{KO} n=8; *Rnf149*^{KO} n=8; *Wsb1*^{KO} n=8); two independent experiments.

N) Frequencies and cell numbers of splenic $CD127^{hi}CD62L^{hi}$ P14 T cells at day 21–22 as in F (*Neurl3*^{KO} n=8; *Rnf149*^{KO} n=8; *Wsb1*^{KO} n=8); two independent experiments.

Statistical significance was calculated using paired Student's *t*-tests (B-E, G-N). Connecting lines indicate that cells were isolated from the same mouse.

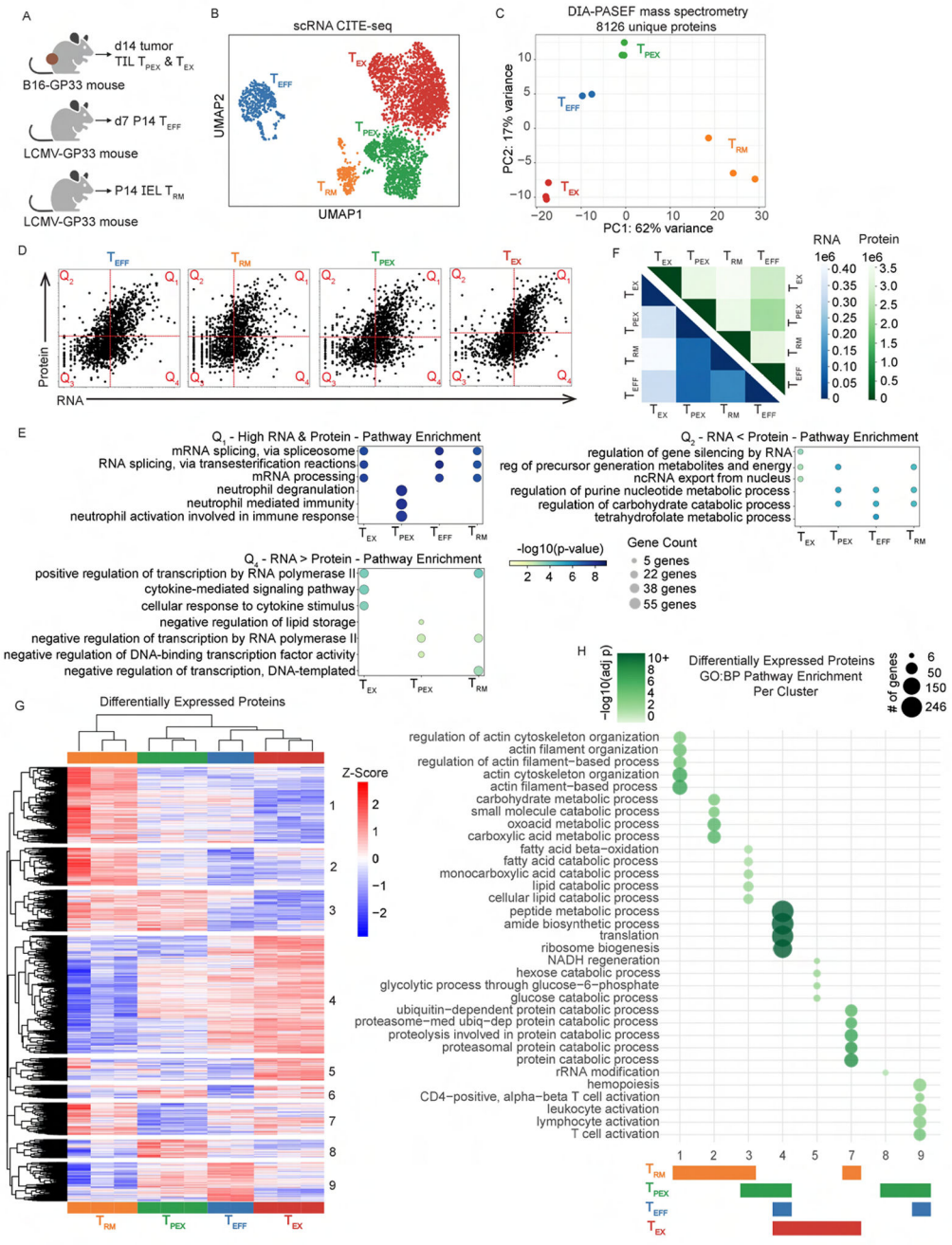

Figure 4: Comparing *ex vivo* T_{EX}, T_{PEX}, T_{RM}, and T_{EFF} transcriptome and proteome

A) Experimental schematic: Endogenous B16 TIL were sorted at d14 (T_{PEX} sorted on $CD8^{+}PD1^{lo/int}Tim3^{-}$ and T_{EX} sorted on $CD8^{+}PD1^{hi}Tim3^{+}$). In parallel, P14 were sorted from d7 LCMV Armstrong infection from spleen (T_{EFF}), and at memory timepoint from the IEL (T_{RM}) (BioRender).

B) RNA UMAP from CITE-seq of $CD8^{+}$ T cells from d7 LCMV Armstrong spleen (P14), d30 IEL (P14 + endogenous), and endogenous B16 TIL T_{PEX} and T_{EX} (defined by PD1 vs Tim3 CITE-seq and enrichment signature; Supplemental Figure 4E). The sequenced cells

were derived from 1 mouse for d7 spleen, pooled from 6 mice for d30 IEL, and pooled from 10 mice for TIL.

C) Protein PCA (DIA-PASEF) of $CD8^+$ T cells from d7 LCMV Armstrong spleen (P14), d14 IEL (P14), and endogenous B16 TIL T_{PEX} and T_{EX}. D14 T_{RM} was used as an early memory timepoint due to cell number limitations at d30. Replicates: d7 spleen n=2, d14 IEL n=3 (6 pooled samples/replicate), T_{PEX} n=3 (6 pooled/replicate) and T_{EX} n=3 (6 pooled/replicate).

D) RNA-protein scatter per T cell subset (non-zero RNA vs non-zero protein, one dot per gene), split into four quadrants by mean expression of total *x*- or *y*-axis.

E) Dot plot of genes from either Q_1, Q_2, or Q_4 for each T cell subset (from D), with GO:BP pathway enrichment for the top 3 significantly pathways per subset.

F) Euclidean distance heatmap of pseudobulk RNA-seq samples (in blue) and protein intensities (in green) in PCA space (darker = more similar).

G) Heatmap with unsupervised hierarchical clustering of the z-score of significant differentially expressed proteins from T_{EFF}, T_{RM}, T_{PEX}, and T_{EX}, with adjusted p-value <0.05.

H) Gene Ontology bubble plot of proteins defining each cluster from G.

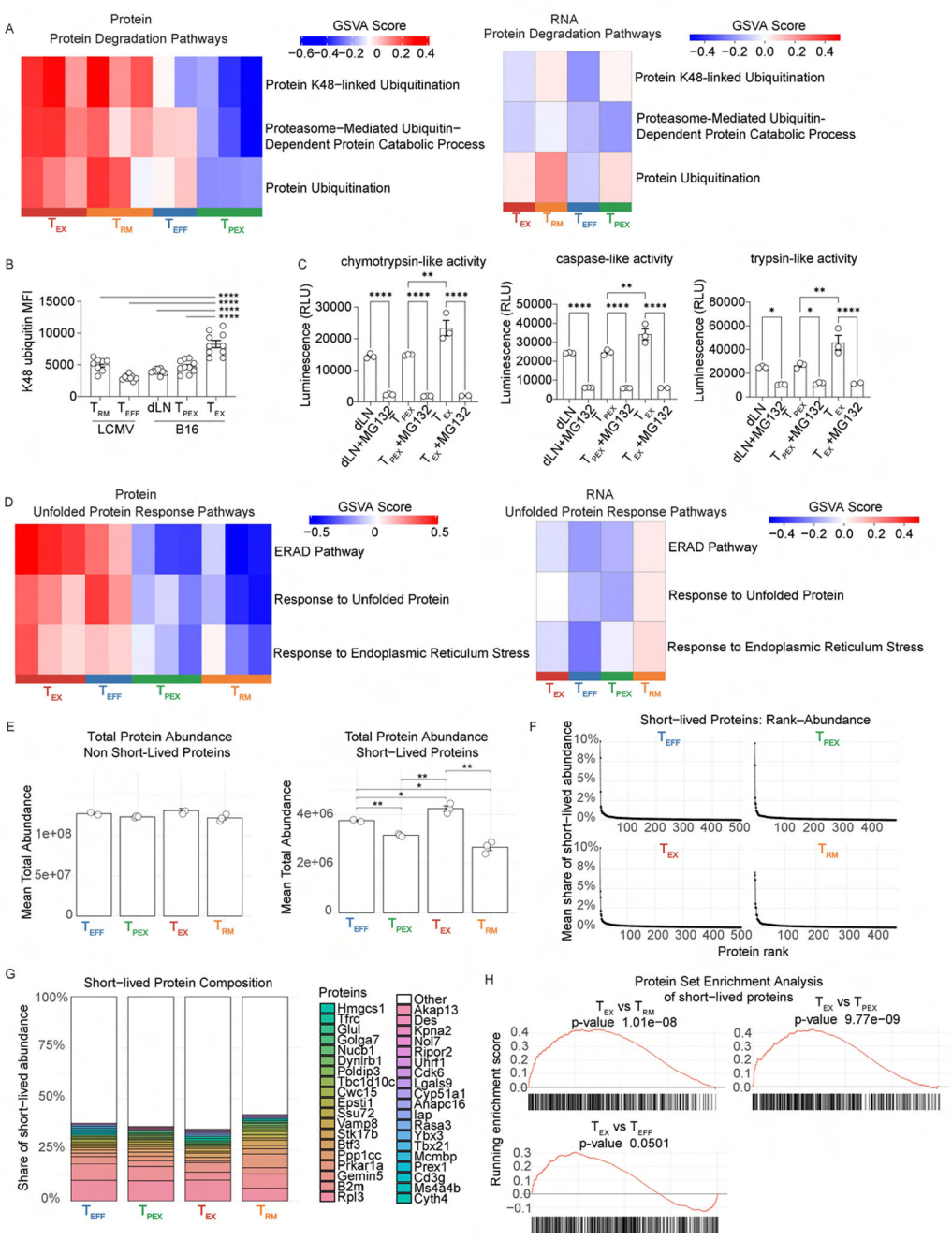

Figure 5: T_{EX} accumulates short-lived proteins yet have functional proteasomes

A) GSVA heatmaps of protein-degradation GO:BP pathways from proteomics (left, data from 4C) and mRNA (right, data from 4B).

B) K48 ubiquitin MFI in $CD8^+$ T cells from P14 IEL d30 (n=8) and P14 spleen d7 (n=9) after LCMV Armstrong infection; and endogenous dLN (n=10), T_{PEX} (n=10) and T_{EX} (n=10) from B16 melanoma after treatment with 10 μM MG-132 for 1 h at 37°C prior to fixation and staining.

C) Chymotrypsin-, caspase-, and trypsin-like activities in sorted dLN, T_{PEX}, and T_{EX} incubated ± 10 μM proteasome inhibitor MG-132 (1 h, 37°C, inhibitor as negative control); 2–3 independent replicates.

D) GSVA heatmaps of unfolded protein response GO:BP pathways from proteomics (left, data from 4C) and mRNA (right, data from 4B).

E) Using *in vitro* T cell protein half-life data (Supplemental Table 7), the *ex vivo* T_{EFF}, T_{RM}, T_{PEX}, and T_{EX} proteomics data were stratified into non-short-lived proteins (half-life between >8 h and ≤20 h; Left) and short-lived proteins (half-life ≤8 h; Right). The mean total abundance per category were quantified.

F) For short-lived proteins (defined in E), rank-abundance curves by subset.

G) For short-lived proteins (defined in E), composition shown as 100% stacked bars with the top 20 proteins per cell type and remaining proteins collapsed into “other”.

H) For short-lived proteins (defined in E), Protein Set Enrichment Analysis across pairwise comparisons with T_{EX}, plots show running enrichment score and short-lived protein postion. Statistical significance was calculated using (B, C, E) one-way ANOVA and empirical Bayes–moderated t-statistic (G).

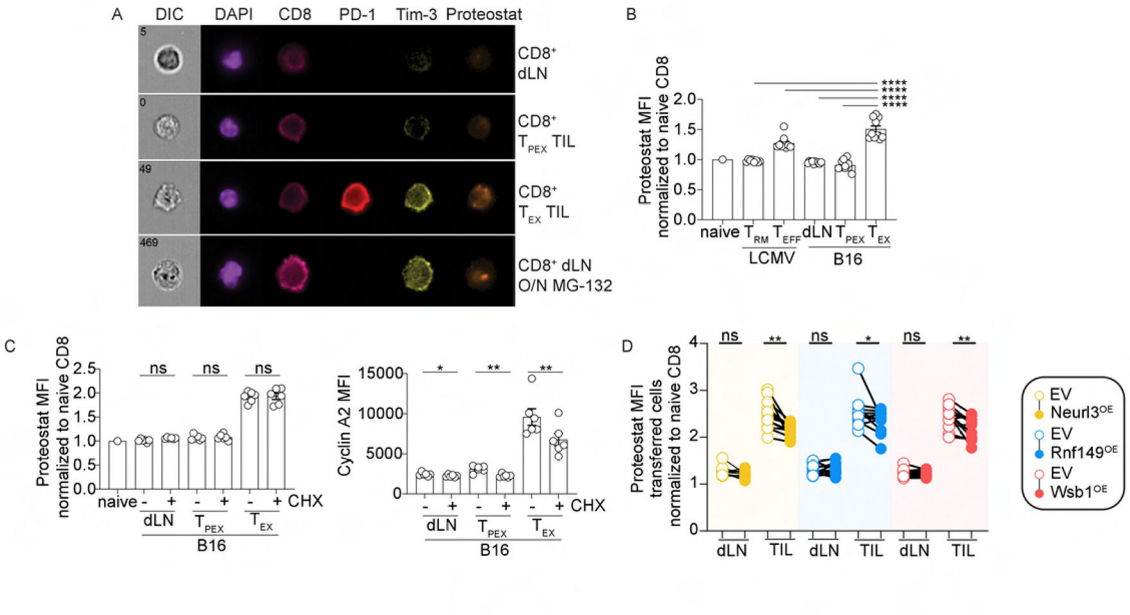

Figure 6: T_{EX} accumulates unfolded proteins, rescued by NEURL3, RNF149, or WSB1 expression

A) ImageStream visualization of Proteostat staining of $CD8^+$ T cells isolated from dLN or TIL (T_{PEX} and T_{EX}), plus MC-132-treated $CD8^+$ T cells (5 μM, 16hr).

B) Proteostat MFI (normalized to spiked-in, congenically mismatched naive $CD8^+$ T cells) in P14 IEL d30 (n=8) or P14 spleen d7 (n=9) after LCMV Armstrong infection, and endogenous dLN (n=10), T_{PEX} (n=10) and T_{EX} (n=10) TIL from B16 melanoma.

C) (Left) Proteostat MFI (normalized as in B) and (Right) Cyclin A2 MFI from $CD8^+$ T cells isolated from endogenous dLN (n=6), T_{PEX} (n=6) and T_{EX} (n=6) TIL from B16 melanoma, treated ± Cycloheximide (20 μg/mL, 6 h, 37°C). Representative of three independent experiments.

D) Proteostat MFI (normalized as in B) from P14 T cells from dLN or tumors of mice with congenically distinct EV vs *Neurl3*^{OE}, *Rnf149*^{OE}, or *Wsb1*^{OE} 8 days after adoptive transfer into tumor-bearing mice (*Neurl3*^{OE} n=12; *Rnf149*^{OE} n=12; *Wsb1*^{OE} n=11); three independent experiments.

Statistical significance was calculated using (B) one-way ANOVA and paired Student's *t*-tests (C-D). Connecting lines indicate that cells were isolated from the same mouse.

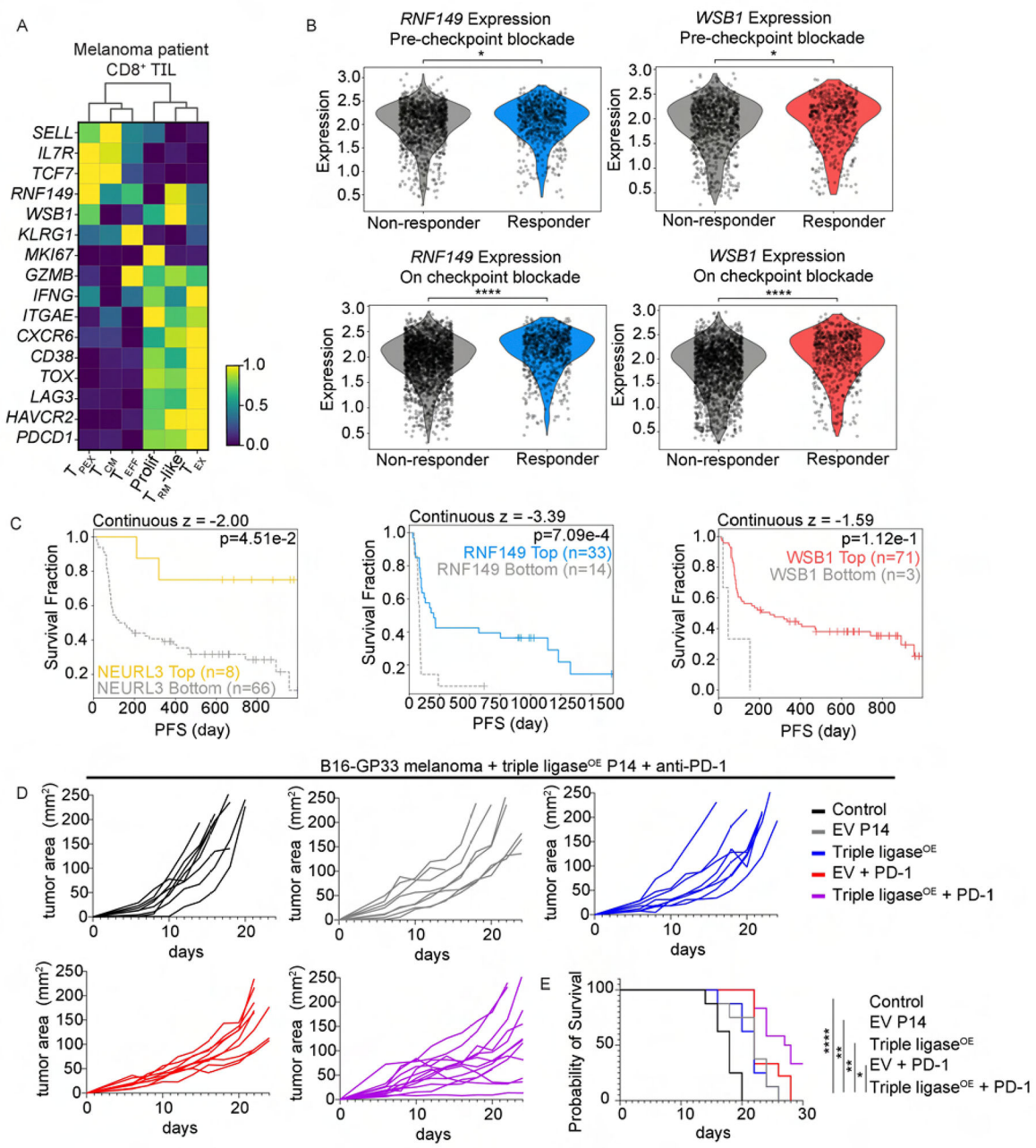

Figure 7: NEURL3, RNF149, or WSB1 expression corresponds with immunotherapeutic responses to checkpoint blockade in human melanoma and improves cancer immunotherapy in mice

A) Heatmap of CD8$^+$ T cell clusters from checkpoint blockade-treated melanoma patients (GSE120575[60]), annotated by top gene expression per cluster; RNF149 and WSB1 expression shown.

B) Violin plots of RNF149 or WSB1 RNA expression in CD8$^+$ TIL with patient data from A, stratified into non-responder vs responder, pre-treatment (top) and on-treatment (bottom).

C) Survival of patients with melanoma (dbGaP Study Accession: phs000452.v3.p1[61]) treated with checkpoint blockade after primary tumor resection and sequencing, stratified by gene expression (high/top vs low/bottom) in the primary tumor. The survival risk score is *z*-score gene effect of death risk in a Cox proportional hazards model. Analysis conducted by TIDE[79].

D) B16-$GP_{33–41}$ tumor area in mice that received no T cells, EV P14 or *Neurl3*$^{OE+}$*Rnf149*$^{OE+}$*Wsb1*^{OE} P14 T cells on d6 after tumor cell implantation with isotype or anti-PD1 treatment every other day; two independent experiments.

E) Survival from D.

Statistical significance was calculated using the (B) unpaired Student's *t*-tests or (C) CoxPH test or the (E) log-rank (Mantel-Cox) test.

Key resources table

REAGENT or RESOURCE	SOURCE	IDENTIFIER
Antibodies		
Anti-mouse CD3e PE	eBioscience	Cat: 12-0031-83; RRID: AB_465497
anti-mouse CD45.1 APC	eBioscience	Cat# 17-0453-82; RRID: AB_469398
anti-mouse CD45.1 Brilliant Violet 785	Biolegend	Cat# 110743; RRID: AB_2563379
anti-mouse CD45.1 FITC	eBioscience	Cat# 11-0453-85; RRID: AB_465059
anti-mouse CD45.1 PerCP Cy5.5	eBioscience	Cat# 45-0453-82; RRID: AB_1107003
anti-mouse CD45.2 Brillant Violet 605	Biolegend	Cat# 109837; RRID: AB_2561393
anti-mouse CD45.2 PerCP Cy5.5	eBioscience	Cat# 45-0454-82; RRID: AB_953590
anti-mouse CD45.2 BV421	Biolegend	Cat: 109831; RRID: AB_10900256
anti-mouse CD45.2 PE-Cyanine7	eBioscience	Cat# 25-0454-82; RRID: AB_2573350
anti-mouse CD45.2 APC	eBioscience	Cat: 17-0454-82; RRID: AB_469400
anti-mouse CD8a FITC	Biolegend	Cat# 100705; RRID: AB_312744
anti-mouse CD8a Brilliant Violet 711	Biolegend	Cat# 100747; RRID: AB_11219594
anti-mouse CD8a Brilliant Violet 785	Biolegend	Cat# 100747; RRID: AB_11219594
anti-mouse CD8a APC-eFluor780	eBioscience	Cat# 47-0081-82; RRID: AB_1272185
anti-mouse TCF1 Pacific Blue	Cell Signaling Technology	Cat# 9066S; RRID: AB_2797696
anti-mouse TCF1 A488	Cell Signaling Technology	Cat# 6444S; RRID: AB_2797627
anti-mouse TOX PE	Miltenyi Biotec	Cat# 130-120-716; RRID: AB_2801780
anti-mouse TOX APC	Miltenyi Biotec	Cat# 130-118-335; RRID: AB_2751485
anti-mouse TIM3 Brilliant Violet 785	Biolegend	Cat# 119725; RRID: AB_2716066
anti-mouse PD-1 PE Cy7	eBioscience	Cat# 25-9985-82; RRID: AB_10853805
anti-mouse PD-1 BV421	Biolegend	Cat# 135217; RRID: AB_10900085
anti-mouse TNF PE	eBioscience	Cat# 12-7321-82; RRID: AB_466199
anti-mouse IFNɣ APC	Biolegend	Cat# 505810; RRID: AB_315404
anti-mouse K48	Abcam	Cat# ab140601; RRID: AB_2783797
anti-mouse CD69 APC	eBioscience	Cat#17-0691-82; RRID: AB_1210795
anti-mouse CD103 PE	eBioscience	Cat# 12-1031-82; RRID: AB_465798
anti-mouse CCR9 PE-Cy7	eBioscience	Cat# 25-1991-82; RRID: AB_10854423
anti-mouse KLRG1 FITC	eBioscience	Cat# 11-5893-82; RRID: AB_1311265
anti-mouse CD127 PE Cy7	eBioscience	Cat# 25-1271-82; RRID: AB_469649
anti-mouse CD62L Brillant Violet 605	Biolegend	Cat# 104437; RRID: AB_11125577
anti-mouse THY1.1 Brillant Violet 650	Biolegend	Cat# 202533; RRID: AB_2562254
anti-mouse THY1.2 Brillant Violet 510	Biolegend	Cat# 140319; RRID: AB_2561395
anti-mouse SLAMF6 PE	BD Bioscience	Cat# 561540; RRID: AB_10713170
anti-mouse CX3CR1 A488	Biolegend	Cat# 149022; RRID: AB_2565705
anti-rabbit APC	Cell Signaling Technology	Cat# 4414S; RRID: AB_10693544
anti-mouse MHCII biotin	eBioscience	Cat: 13-5321-81; RRID: AB_466661
anti-mouse B220 biotin	Biolegend	Cat: 103204; RRID: AB_312989

REAGENT or RESOURCE	SOURCE	IDENTIFIER
anti-mouse CD4 biotin	Biolegend	Cat: 100404; RRID: AB_312689
anti-mouse CD19 biotin	Biolegend	Cat: 115504; RRID: AB_313639
anti-mouse CD11b biotin	Biolegend	Cat: 101204; RRID: AB_312787
Biotin anti-mouse Ly-6G/Ly-6C (Gr-1) Antibody	BioLegend	Cat#108404; RRID: AB_313368
anti-mouse NK1.1 biotin	ebioscience	Cat: 13-5941-85; RRID: AB_466805
Alexa Fluor® 488 AffiniPure® Donkey Anti-Rabbit IgG (H+L)	Jackson Immunoresearch	Cat: 711-545-152; RRID: AB_2313584
Cyclin A2 Recombinant Rabbit Monoclonal Antibody	Invitrogen	Cat: MA5-54060; RRID: AB_3248531
InVivoMAb polyclonal Armenian hamster IgG	Bio X Cell	Cat# BE0091
InVivoMAb anti-mouse PD-1 (CD279)	Bio X Cell	Cat# BE0033-2
InVivoMAb anti-mouse 4-1BB (CD137)	Bio X Cell	Cat #BE0239
InVivoMAb rat IgG2a isotype control, anti-trinitrophenol	Bio X Cell	Cat #BE0089
TotalSeq™-C0833 anti-mouse CD194 (CCR4) Antibody	BioLegend	Cat#131221; RRID: AB_2876463
TotalSeq™-C0096 anti-mouse CD45 Antibody	BioLegend	Cat#103169; RRID: AB_2832302
TotalSeq™-C0075 anti-mouse CD90.2 (Thy1.2) Antibody	BioLegend	Cat#105353; RRID: AB_2832346
TotalSeq™-C0930 anti-mouse Ly108 Antibody	BioLegend	Cat#134613; RRID: AB_2890692
TotalSeq™-C0879 anti-mouse IL-21R Antibody	BioLegend	Cat#131911; RRID: AB_2876466
TotalSeq™-C0377 anti-mouse CD197 (CCR7) Antibody	BioLegend	Cat#120131; RRID: AB_2819839
TotalSeq™-C0836 anti-mouse DR3 (TNFRSF25) Antibody	BioLegend	Cat#144415; RRID: AB_2876493
TotalSeq™-C0002 anti-mouse CD8a Antibody	BioLegend	Cat#100785; RRID: AB_2819776
TotalSeq™-C0111 anti-mouse CD5 Antibody	BioLegend	Cat#100647; RRID: AB_2860586
TotalSeq™-C0227 anti-mouse CD122 (IL-2Rβ) Antibody	BioLegend	Cat#105915; RRID: AB_2860612
TotalSeq™-C0881 anti-mouse CD272 (BTLA) Antibody	BioLegend	Cat#139123; RRID: AB_2892292
TotalSeq™-C0093 anti-mouse CD19 Antibody	BioLegend	Cat#115571; RRID: AB_2832392
TotalSeq™-C1006 anti-mouse CD160 Antibody	BioLegend	Cat#143015; RRID: AB_2892297
TotalSeq™-C0178 anti-mouse CD45.1 Antibody	BioLegend	Cat#110757; RRID: AB_2819824
TotalSeq™-C0198 anti-mouse CD127 (IL-7Rα) Antibody	BioLegend	Cat#135047; RRID: AB_2819874
TotalSeq™-C0981 anti-mouse TCR Vα2 Antibody	BioLegend	Cat#127829; RRID: AB_2819866
TotalSeq™-C0982 anti-mouse TCR Vα8.3 Antibody	BioLegend	Cat#127709; RRID: AB_2819865
TotalSeq™-C0114 anti-mouse F4/80 Antibody	BioLegend	Cat#123157; RRID: AB_2832437
TotalSeq™-C1063 anti-mouse CD45RB Antibody	BioLegend	Cat#103321; RRID: AB_2888760
TotalSeq™-C0171 anti-human/mouse/rat CD278 (ICOS) Antibody	BioLegend	Cat#313553; RRID: AB_2800823
TotalSeq™-C0378 anti-mouse CD223 (LAG-3) Antibody	BioLegend	Cat#125237; RRID: AB_2832450
TotalSeq™-C0228 anti-mouse CD183 (CXCR3) Antibody	BioLegend	Cat#126545; RRID: AB_2832454
TotalSeq™-C0130 anti-mouse Ly-6A/E (Sca-1) Antibody	BioLegend	Cat#108151; RRID: AB_2832370
TotalSeq™-C0837 anti-mouse IL-33Rα (IL1RL1, ST2) Antibody	BioLegend	Cat#145319; RRID: AB_2819892
TotalSeq™-C0193 anti-mouse CD357 (GITR) Antibody	BioLegend	Cat#126327; RRID: AB_2832452
TotalSeq™-C0834 anti-mouse CD39 Antibody	BioLegend	Cat#143815; RRID: AB_2819888
TotalSeq™-C1064 anti-mouse/rat CD81 Antibody	BioLegend	Cat#104915; RRID: AB_2876412

REAGENT or RESOURCE	SOURCE	IDENTIFIER
Totalseq™-C0214 anti-human/mouse integrin β7 Antibody	BioLegend	Cat#321229; RRID: AB_2810481
TotalSeq™-C0237 Rat IgG1, λ Isotype Ctrl Antibody	BioLegend	Cat#401921; RRID: AB_3097123
TotalSeq™-C0200 anti-mouse CD86 Antibody	BioLegend	Cat#105059; RRID: AB_2860608
TotalSeq™-C0121 anti-mouse TCR γ/δ Antibody	BioLegend	Cat#118141; RRID: AB_2819838
TotalSeq™-C0070 anti-human/mouse CD49f Antibody	BioLegend	Cat#313635; RRID: AB_2800825
TotalSeq™-C0197 anti-mouse CD69 Antibody	BioLegend	Cat#104551; RRID: AB_2832333
TotalSeq™-C0120 anti-mouse TCR β chain Antibody	BioLegend	Cat#109259; RRID: AB_2819820
TotalSeq™-C0013 anti-mouse Ly-6C Antibody	BioLegend	Cat#128051; RRID: AB_2832461
TotalSeq™-C0429 anti-mouse CD48 Antibody	BioLegend	Cat#103459; RRID: AB_2876409
TotalSeq™-C0885 anti-mouse CD270 (HVEM) Antibody	BioLegend	Cat#136309; RRID: AB_2876474
TotalSeq™-C0850 anti-mouse CD49a Antibody	BioLegend	Cat#142615; RRID: AB_2832511
TotalSeq™-C0421 anti-mouse CD49b Antibody	BioLegend	Cat#103527; RRID: AB_2876410
TotalSeq™-C0570 anti-mouse/rat CD29 Antibody	BioLegend	Cat#102237; RRID: AB_2890670
TotalSeq™-C0241 Armenian Hamster IgG Isotype Ctrl Antibody	BioLegend	Cat#400977; RRID: AB_2894970
TotalSeq™-C0916 anti-mouse CD124 (IL-4Rα) Antibody	BioLegend	Cat#144811; RRID: AB_2832524
TotalSeq™-C0073 anti-mouse/human CD44 Antibody	BioLegend	Cat#103063; RRID: AB_2813930
TotalSeq™-C0235 anti-mouse TCR Vβ8.1, 8.2 Antibody	BioLegend	Cat#118419; RRID: AB_2860641
TotalSeq™-C0983 anti-mouse TCR Vα8.3 Antibody	BioLegend	Cat#125711; RRID: AB_2819853
TotalSeq™-C0846 anti-mouse CD185 (CXCR5) Antibody	BioLegend	Cat#145537; RRID: AB_2814051
TotalSeq™-C0191 anti-mouse/rat/human CD27 Antibody	BioLegend	Cat#124245; RRID: AB_2832448
TotalSeq™-C0212 anti-mouse CD24 Antibody	BioLegend	Cat#101843; RRID: AB_2819784
TotalSeq™-C0014 anti-mouse/human CD11b Antibody	BioLegend	Cat#101275; RRID: AB_2832272
TotalSeq™-C0595 anti-mouse CD11a Antibody	BioLegend	Cat#101131; RRID: AB_2832271
TotalSeq™-C0117 anti-mouse I-A/I-E Antibody	BioLegend	Cat#107659; RRID: AB_2832368
TotalSeq™-C1062 anti-mouse CD30 Antibody	BioLegend	Cat#102313; RRID: AB_2888806
TotalSeq™-C0112 anti-mouse CD62L Antibody	BioLegend	Cat#104455; RRID: AB_2819800
TotalSeq™-C1012 anti-mouse CD178 (FasL) Antibody	BioLegend	Cat#106615; RRID: AB_2892272
TotalSeq™-C0562 anti-mouse CD83 Antibody	BioLegend	Cat#121521; RRID: AB_2860647
TotalSeq™-C0190 anti-mouse CD274 (B7-H1, PD-L1) Antibody	BioLegend	Cat#153610; RRID: AB_2860721
TotalSeq™-C0915 anti-mouse VISTA (PD-1H) Antibody	BioLegend	Cat#150219; RRID: AB_2860714
TotalSeq™-C0091 Mouse IgG2a, κ isotype Ctrl Antibody	BioLegend	Cat#400293; RRID: AB_2888922
TotalSeq™-C0090 Mouse IgG1, κ isotype Ctrl Antibody	BioLegend	Cat#400187; RRID: AB_2888921
TotalSeq™-C0092 Mouse IgG2b, κ isotype Ctrl Antibody	BioLegend	Cat#400381; RRID: AB_2888923
TotalSeq™-C0354 anti-mouse TCR Vβ5.1, 5.2 Antibody	BioLegend	Cat#139519; RRID: AB_2819882
TotalSeq™-C0813 anti-mouse CD9 Antibody	BioLegend	Cat#124825; RRID: AB_2876447
TotalSeq™-C0106 anti-mouse CD11c Antibody	BioLegend	Cat#117361; RRID: AB_2819834
TotalSeq™-C0807 anti-mouse CD200R (OX2R) Antibody	BioLegend	Cat#123919; RRID: AB_2876445

REAGENT or RESOURCE	SOURCE	IDENTIFIER
TotalSeq™-C0380 anti-rat CD90/mouse CD90.1 (Thy1.1) Antibody	BioLegend	Cat#202551; RRID: AB_2876578
TotalSeq™-C0195 anti-mouse CD134 (OX-40) Antibody	BioLegend	Cat#119435; RRID: AB_2832423
TotalSeq™-C0079 anti-mouse CD200 (OX2) Antibody	BioLegend	Cat#123823; RRID: AB_2860656
TotalSeq™-C0097 anti-mouse CD25 Antibody	BioLegend	Cat#102065; RRID: AB_2876399
TotalSeq™-C0118 anti-mouse NK-1.1 Antibody	BioLegend	Cat#108765; RRID: AB_2819815
TotalSeq™-C0078 anti-mouse CD49d Antibody	BioLegend	Cat#103633; RRID: AB_2860605
TotalSeq™-C0103 anti-mouse/human CD45R/B220 Antibody	BioLegend	Cat#103273; RRID: AB_2832307
TotalSeq™-C0116 anti-mouse Ly-6G/Ly-6C (Gr-1) Antibody	BioLegend	Cat#108463; RRID: AB_2832371
TotalSeq™-C0558 anti-mouse CD55 (DAF) Antibody	BioLegend	Cat#131815; RRID: AB_2876464
TotalSeq™-C0892 anti-mouse CD2 Antibody	BioLegend	Cat#100121; RRID: AB_2892259
TotalSeq™-C0001 anti-mouse CD4 Antibody	BioLegend	Cat#100571; RRID: AB_2813913
TotalSeq™-C0004 anti-mouse CD279 (PD-1) Antibody	BioLegend	Cat#109127; RRID: AB_2819819
TotalSeq™-C0003 anti-mouse CD366 (Tim-3) Antibody	BioLegend	Cat#119739; RRID: AB_2832424
TotalSeq™-C0236 Rat IgG1, κ Isotype Ctrl Antibody	BioLegend	Cat#400467; RRID: AB_2894972
TotalSeq™-C0238 Rat IgG2a, κ Isotype Ctrl Antibody	BioLegend	Cat#400577; RRID: AB_2894971
TotalSeq™-C0240 Rat IgG2c, κ Isotype Ctrl Antibody	BioLegend	Cat#400741; RRID: AB_3097108
TotalSeq™-C0095 Rat IgG2b, κ Isotype Ctrl Antibody	BioLegend	Cat#400677; RRID: AB_2894967
TotalSeq™-C0110 anti-mouse CD43 Antibody	BioLegend	Cat#143221; RRID: AB_2860697
TotalSeq™-C0563 anti-mouse CX3CR1 Antibody	BioLegend	Cat#149043; RRID: AB_2819898
TotalSeq™-C0909 anti-mouse CD182 (CXCR2) Antibody	BioLegend	Cat#149319; RRID: AB_2814053
TotalSeq™-C0926 anti-mouse CD186 (CXCR6) Antibody	BioLegend	Cat#151127; RRID: AB_2894676
TotalSeq™-C0426 anti-mouse CD192 (CCR2) Antibody	BioLegend	Cat#150631; RRID: AB_2876502
TotalSeq™-C0907 anti-mouse CD198 (CCR8) Antibody	BioLegend	Cat#150321; RRID: AB_2819900
TotalSeq™-C0192 anti-mouse CD20 Antibody	BioLegend	Cat#150427; RRID: AB_2860716
TotalSeq™-C0917 anti-mouse CD95 (Fas) Antibody	BioLegend	Cat#152616; RRID: AB_2860719
TotalSeq™-C0823 anti-mouse CD34 Antibody	BioLegend	Cat#152211; RRID: AB_2832536
TotalSeq™-C0203 anti-mouse CD150 (SLAM) Antibody	BioLegend	Cat#115947; RRID: AB_2819830
TotalSeq™-C0122 anti-mouse TER-119/Erythroid Cells Antibody	BioLegend	Cat#116259; RRID: AB_2832405
TotalSeq™-C1058 anti-mouse FR4 (Folate Receptor 4) Antibody	BioLegend	Cat#125113; RRID: AB_2876448
TotalSeq™-C0949 anti-mouse CD226 (DNAM-1) Antibody	BioLegend	Cat#133631; RRID: AB_2894682
TotalSeq™-C1011 anti-mouse CD155 (PVR) Antibody	BioLegend	Cat#131533; RRID: AB_2892286
TotalSeq™-C0077 anti-mouse CD73 Antibody	BioLegend	Cat#127237; RRID: AB_2860665
TotalSeq™-C0914 anti-mouse CD273 (B7-DC, PD-L2) Antibody	BioLegend	Cat#107229; RRID: AB_2860615
TotalSeq™-C0211 anti-mouse TCR Vγ2 Antibody	BioLegend	Cat#137713; RRID: AB_2819877
TotalSeq™-C0842 anti-mouse Ly-49A Antibody	BioLegend	Cat#116813; RRID: AB_2876431
TotalSeq™-C0074 anti-mouse CD54 Antibody	BioLegend	Cat#116137; RRID: AB_2819831
TotalSeq™-C0230 anti-mouse CD8b (Ly-3) Antibody	BioLegend	Cat#126639; RRID: AB_2892281

REAGENT or RESOURCE	SOURCE	IDENTIFIER
TotalSeq™-C0893 anti-mouse CD120b (TNF R Type II/p75) Antibody	BioLegend	Cat#113409; RRID: AB_2894663
TotalSeq™-C0301 anti-mouse Hashtag 1 Antibody	BioLegend	Cat: 155861; RRID: AB_2800693
TotalSeq™-C0302 anti-mouse Hashtag 2 Antibody	BioLegend	Cat: 155863; RRID: AB_2800694
TotalSeq™-C0303 anti-mouse Hashtag 3 Antibody	BioLegend	Cat: 155865; RRID: AB_2800695
TotalSeq™-C0304 anti-mouse Hashtag 4 Antibody	BioLegend	Cat: 155867; RRID: AB_2800696
TotalSeq™-C0305 anti-mouse Hashtag 5 Antibody	BioLegend	Cat: 155869; RRID: AB_2800697
TotalSeq™-C0306 anti-mouse Hashtag 6 Antibody	BioLegend	Cat: 155871; RRID: AB_2819910
TotalSeq™-C0307 anti-mouse Hashtag 7 Antibody	BioLegend	Cat: 155873; RRID: AB_2819911
TotalSeq™-C0308 anti-mouse Hashtag 8 Antibody	BioLegend	Cat: 155875; RRID: AB_2819912
TotalSeq™-C0309 anti-mouse Hashtag 9 Antibody	BioLegend	Cat: 155877; RRID: AB_2819913
TotalSeq™-C0310 anti-mouse Hashtag 10 Antibody	BioLegend	Cat: 155879; RRID: AB_2819914
TotalSeq™-C Mouse Universal Cocktail, V1.0	Biolegend	Cat: 199903; RRID: AB_2924498
Bacterial and virus strains		
Subcloning Efficiency™ DH5α Competent Cells	Thermo Scientific	Cat#18265017
LCMV-Armstrong	Rafi Ahmed, Emory University	NA
LCMV-Cl13	Rafi Ahmed, Emory University	NA
Biological samples		
Chemicals, peptides, and recombinant proteins		
AccuCheck Counting Beads	Thermo Scientific	Cat#PCB100
eBioscience Fixable Viability Dye eFluor 780	Thermo Scientific	Cat# 65-0865-14
eBioscience Fixable Viability Dye eFluor 450	Thermo Scientific	Cat#65-0863-18
Brilliant II SYBR Green qPCR Master Mix	Agilent Technologies	Cat#600828
HyClone™ RPMI 1640 media: Liquid	Fisher Scientific	Cat#SH30096FS
Gibco™ DMEM, high glucose, no glutamine	Fisher Scientific	Cat#11-960-069
HyClone™ Fetal Bovine Serum Characterized	HyClone	Cat#SH30071.03
Gibco™ Sodium Pyruvate (100 mM)	Thermo Scientific	Cat#11360070
Gibco™ HEPES (1M)	Thermo Scientific	Cat#15630080
Gibco™ MEM Non-Essential Amino Acids Solution (100X)	Fisher Scientific	Cat#11-140-050
Gibco™2-Mercaptoethanol	Thermo Scientific	Cat#21985023
Gibco™ Penicillin-Streptomycin-Glutamine (100X)	Thermo Scientific	Cat#10378-016
Clontech Labs 3P RETRONECTIN	Takara Bio	Cat#T100B
STREPTAVIDIN MICROBEADS	Miltenyi Biotec	Cat#130-048-101
SIGMA Percoll® pH 8.5-9.5 (25 °C)	Sigma-Aldrich	Cat#P1644-1L
Corning® DPBS (Dulbecco's Phosphate-Buffered Saline)	Corning	Cat#20-031-CV
Magnesium Chloride Hexahydrate	OmniPur	Cat#5980

REAGENT or RESOURCE	SOURCE	IDENTIFIER
Calcium Chloride Dihydrate (White Crystals to Powder), Fisher BioReagents™	Fisher Scientific	Cat#BP510-500
Calf Serum Iron Supplemented	R&D Systems	Cat#S11950H
Collagenase, Type 1	Worthington Biochemical	Cat# LS004196
HEPES (Fine White Crystals/Molecular Biology), Fisher BioReagents™	Fisher Scientific	Cat#BP310500
L-Glutamine ≥99% (HPLC), ReagentPlus®	Sigma-Aldrich	Cat#G3126-100G
Biochemical Fisher Chemical™ Ammonium Chloride ACS Grade ≥99.5%	Fisher Scientific	Cat#A661-500
Potassium Bicarbonate (Powder/USP/FCC), Fisher Chemical	Fisher Scientific	Cat#P235-500
Apex Bioresearch Products 20-147 EDTA, Disodium Dihydrate Salt, Ultra Pure Grade	Genesee Scientific	Cat#Genesee20-147
Corning™ Lymphocyte Separation Medium	Fisher Scientific	Cat#MT25072CV
Sodium Bicarbonate (Powder/Certified ACS), Fisher Chemical™	Fisher Scientific	Cat#S233-500
Hank's Balanced Salt Solution, 10X without sodium bicarbonate, calcium and magnesium	Corning	Cat#20-021-CV
1,4-Dithioerythritol ≥99.0%	Sigma-Aldrich	Cat# D8255-25G
Fixation Buffer	BioLegend	Cat#420801
eBioscience™ Foxp3 / Transcription Factor Staining Buffer Set	Invitrogen	Cat#00-5523-00
BD Cytofix/Cytoperm™ Fixation/Permeabilization Kit	BD Biosciences	Cat#BD554714
PROTEOSTAT® Protein aggregation assay	Enzo Life Sciences	Cat#ENZ-51023-KP050
MG-132, Ready Made Solution ≥90% (HPLC)	Sigma-Aldrich	Cat#M7449-200UL
RPMI 1640 Medium for SILAC	Thermo Scientific	Cat#A33823
Fetal Bovine Serum, dialyzed, US origin	Thermo Scientific	Cat#26-400-044
L-Arginine-HCl, 13C6, 15N4 for SILAC	Thermo Scientific	Cat#89990
L-Lysine-2HCl, 13C6, 15N2 for SILAC	Thermo Scientific	Cat#88209
L-Alanine ≥98% (TLC)	Sigma-Aldrich	Cat#A7627-1G
Recombinant Cas9-NLS purified protein	UC Berkeley MacroLab	NA
DAPI (4',6-Diamidino-2-Phenylindole, Dilactate)	Biolegend	Cat#422801
Recombinant human IL2 protein	CETUS	NA
Mouse IL-15 Recombinant Protein	PeproTech	Cat# 210-15-100UG
Recombinant Mouse TGF-β1	Biolegend	Cat# 763104
Retinoic acid ≥98% (HPLC) powder	Sigma-Aldrich	Cat# R2625-50MG
Sequencing grade modified trypsin	Promega	Cat# V5111
Lys-C protease	Fujifilm Wako	Cat# 129-02541
TCEP	Sigma-Aldrich	Cat# 580560-1GM
Iodoacetamide (IAA)	MP Biomedicals	Cat# 100351
Dithiothreitol (DTT)	Fisher Scientific	Cat# BP172-25
SPRIselect reagent	Beckman Coulter	Cat: B23318
Cycloheximide InSolution, 100 mg/mL in DMSO, Suitable for cell culture	Sigma-Aldrich	Cat: 239765-1ML
LCMV gp33-41 peptide	AnaSpec	Cat: 61296

REAGENT or RESOURCE	SOURCE	IDENTIFIER
Protein Transport Inhibitor Cocktail (500X)	ebioscience	Cat: 00-4980-93
Triton X-100	Sigma-Aldrich	Cat#X100
UltraPure™ SDS Solution, 10%	Thermo Scientific	Cat#24730020
Halt™ Protease Inhibitor Cocktail (100X)	Thermo Scientific	Cat#78430
Pierce™ Phosphatase Inhibitor Mini Tablets	Thermo Scientific	Cat#A32957
Water, Optima™ LC/MS Grade	Fisher Chemical	Cat#W6-1
Pierce™ Premium Grade TCEP-HCl	Thermo Scientific	Cat#PIPG82089
Triethylammonium Bicarbonate Buffer	Honeywell Fluka	Cat#60-044-973
Chloroform	Fisher Chemical	Cat#C297-4
Methanol, Optima™ LC/MS Grade	Fisher Chemical	Cat#A456-4
Acetonitrile, Optima™ LC/MS Grade	Fisher Chemical	Cat#A955-4
Formic Acid, 99.0+%, Optima™ LC/MS Grade	Fisher Chemical	Cat#A117-50
Trifluoroacetic Acid, Optima™ LC/MS Grade	Fisher Chemical	Cat#A116-10X1AMP
Waters Sep-Pak C18 1 cc Vac Cartridge, 50 mg Sorbent per Cartridge, 55 - 105 µm	Waters	Cat#WAT054955
AcroPrep Advance Filter Plate (Pall)	Fisher Scientific	Cat#17164641
Sequencing Grade Modified Trypsin, lyophilized	Promega	Cat#V5111
C18 Evotips	Evosep	Cat#EV2013
Critical commercial assays		
Proteasome-Glo 3-Substrate Cell-Based Assay System	Promega	Cat#G1180
P3 Primary Cell 4D-Nucleofector® X Kit S	Lonza	Cat#V4XP-3032
RNeasy Mini Kit (250)	Qiagen	Cat#74106
Applied Biosystems™ High-Capacity cDNA Reverse Transcription Kit	Fisher Scientific	Cat#43-688-14
Chromium Next GEM Single Cell 5' Kit v2	10X Genomics	Cat: PN-1000263
5' Feature Barcode Kit	10X Genomics	Cat: PN-1000541
Library Construction Kit	10X Genomics	Cat: PN-1000190
Dual Index Kit TT Set A	10X Genomics	Cat: PN-1000215
Dual Index Kit TN Set A	10X Genomics	Cat: PN-1000250
Pierce™ BCA Protein Assay Kits	Thermo Scientific	Cat#23227
Deposited data		
Mouse B16 CD8+ T cell dLN and TIL bulk RNAseq	Ford et al.[33]	GEO: GSE175408
Mouse P14 circ memory and TRM scRNAseq	Crowl et al.[78]	GEO: GSE182275
Mouse P14 T cells isolated from IEL or spleens postinfection (naïve to d90) scRNAseq	Kurd et al.[80]	GEO: GSE131847
Human melanoma TIL pre/post checkpoint blockade scRNAseq	Sade-Feldman et al.[60]	GEO: GSE120575
Clinical outcomes to PD1 blockade in patients with metastatic melanoma bulk RNAseq	Liu et al. [61]	dbGaP Study Accession: phs000452.v3.p1
Exhausted Mouse CD8 T cells generated *in vitro* bulk RNAseq	Scharping et al.[81]	GEO: GSE155192

REAGENT or RESOURCE	SOURCE	IDENTIFIER
CITE-seq of d5 ligase KO P14 T cells from LCMV Armstrong	This paper	GEO: GSE298127 Token: gxghoosifloznup
DIA PASEF *ex vivo* T cell mass spectrometry data (T_{EFF}, TPEX, TEX, TRM)	This paper	ProteomeXchange Consortium PRIDE: PXD063865 Token: ihZ5VtMxuC4V
DIA PASEF *ex vivo* T cell mass spectrometry data (T_{CM}, T_{EM}, LLTE, T_{RM})	This paper	ProteomeXchange Consortium PRIDE: PXD070932 Token: cdDl1Hst6nOo
TMT *ex vivo* T cell mass spectrometry data	This paper	ProteomeXchange Consortium MassIVE: MSV000097956 Password: Sharping2025
CITE-seq of CD3ε+ T cells from d7 LCMV Armstrong	This paper	GEO: GSE301271 Token: inevuaaobruthqv
CITE-seq of CD3ε+ T cells from d30 LCMV Armstrong	This paper	GEO: GSE301960 Token: elsngwocxtwphiz
CITE-seq of CD3ε+ T cells from B16-GP33	This paper	GEO: currently uploading, ID available in <5 business days
Protein turnover *in vitro* T cell mass spectrometry data	This paper	ProteomeXchange Consortium PRIDE: PXD067417 Token: g2FhAs25KH6N
EV and Neurl3^{OE} P14 - dLN and TIL bulk RNAseq	This paper	GEO: GSE298128 token: kfenckiqrdozhqz
Experimental models: Cell lines		
Platinum-E (Plat-E) Retroviral Packaging Cell Line	Cell Biolabs	Cat# RV-101
C57BL/6 mouse colon adenocarcinoma MC38, modified for GP33-41 expression	Kerafast	Parental line: Cat#ENH204-FP
C57BL/6 mouse B16-F10 skin melanoma, modified for GP33-41 expression	Gift from Dr Alain Lamarre	NA
Experimental models: Organisms/strains		
Mouse; C57BL/6J	Jackson Laboratory	Strain#000664; RRID: IMSR_JAX:000664
Mouse; B6.PL-*Thy1^{a}*/CyJ	Jackson Laboratory	Strain#000406; RRID: IMSR_JAX:000406
Mouse; P14 CD8 Transgenic (NCI background)	Rafi Ahmed, Emory University	N/A
Mouse; B6.SJL-*Ptprc^{a} Pepc^{b}*/BoyJ	Jackson Laboratory	Strain#002014; RRID: IMSR_JAX:002014
Oligonucleotides		
Beta Actin F: GAGACCTTCAACACCCC	This paper	NA
Beta Actin R: GTGGTGGTGAAGCTGTAGCC	This paper	NA
Neurl3 F: TGTGTACGGGACCACGAAAG	This paper	NA
Neurl3 R: ACTACAGCCACCTCCTCGAT	This paper	NA
Rnf149 F: GGAGTTCATCAGCGGTCAGT	This paper	NA
Rnf149 R: ACACATTGGACACGTTCGGT	This paper	NA
Wsb1 F: CTGGACGGTTGCTTTTGCTC	This paper	NA
Wsb1 R: TAACGTGCTCAGGAGGCTTG	This paper	NA
tracr RNA (Alt-R® CRISPR-Cas9 tracrRNA, ATTO™ 550)	IDT	Cat#1077024

REAGENT or RESOURCE	SOURCE	IDENTIFIER
/AltR1/rCrC rGrCrC rArUrG rArGrA rArUrA rArCrA rCrCrA rGrUrU rUrUrA rGrArG rCrUrA rUrGrC rU/AltR2/	IDT	Mm.Cas9.THY1.1.AC
/AltR1/rUrA rGrArG rGrGrU rGrGrC rUrCrU rUrCrG rCrCrA rGrUrU rUrUrA rGrArG rCrUrA rUrGrC rU/AltR2/	IDT	Mm.Cas9.NEURL3.1.AR
/AltR1/rGrG rArGrG rArGrC rArGrA rGrUrC rCrCrA rCrGrU rGrUrU rUrUrA rGrArG rCrUrA rUrGrC rU/AltR2/	IDT	Mm.Cas9.NEURL3.1.AS
/AltR1/rArG rGrUrC rCrGrG rGrCrA rCrArC rGrArA rGrGrG rGrUrU rUrUrA rGrArG rCrUrA rUrGrC rU/AltR2/	IDT	Mm.Cas9.NEURL3.1.AL
/AltR1/rArG rUrUrU rCrCrA rCrGrG rGrArA rCrGrC rCrArC rGrUrU rUrUrA rGrArG rCrUrA rUrGrC rU/AltR2/	IDT	Mm.Cas9.NEURL3.1.AJ
/AltR1/rArU rGrGrU rArUrC rGrUrG rUrUrC rArGrC rCrArG rGrUrU rUrUrA rGrArG rCrUrA rUrGrC rU/AltR2/	IDT	Mm.Cas9.NEURL3.1.AP
/AltR1/rGrU rUrGrU rArGrA rCrCrA rCrCrA rCrGrG rCrCrG rGrUrU rUrUrA rGrArG rCrUrA rUrGrC rU/AltR2/	IDT	Mm.Cas9.RNF149.1.AB
/AltR1/rGrU rArGrC rUrGrA rUrCrC rUrGrU rCrCrA rArArU rGrUrU rUrUrA rGrArG rCrUrA rUrGrC rU/AltR2/	IDT	Mm.Cas9.WSB1.1.AT
/AltR1/rUrC rUrUrA rCrGrG rCrArC rUrGrG rGrArC rCrArC rGrUrU rUrUrA rGrArG rCrUrA rUrGrC rU/AltR2/	IDT	Mm.Cas9.WSB1.1.AS
/AltR1/rUrC rCrUrU rGrUrG rArCrC rArCrG rCrArA rArGrU rGrUrU rUrUrA rGrArG rCrUrA rUrGrC rU/AltR2/	IDT	Mm.Cas9.WSB1.1.AP
/AltR1/rCrA rGrUrC rUrArU rArArC rGrUrG rCrUrC rArGrG rGrUrU rUrUrA rGrArG rCrUrA rUrGrC rU/AltR2/	IDT	Mm.Cas9.WSB1.1.AD
/AltR1/rArC rArArG rGrArG rUrArA rGrCrU rCrCrC rArUrC rGrUrU rUrUrA rGrArG rCrUrA rUrGrC rU/AltR2/	IDT	Mm.Cas9.WSB1.1.AG
Recombinant DNA		
pMSCV-IRES-mAmetrine 1.1 FP	Addgene	Cat#52113
pMSCV-IRES Neurl3 mAmetrine	This paper	NA
pMSCV-IRES Rnf149 mAmetrine	This paper	NA
pMSCV-IRES Wsb1 mAmetrine	This paper	NA
pMSCV-IRES Thy1.1	Addgene	Cat#17442
pMSCV-IRES Neurl3 Thy1.1	This paper	NA
pMSCV-IRES Rnf149 Thy1.1	This paper	NA
pMSCV-IRES Wsb1 Thy1.1	This paper	NA
pMSCV-IRES-mCherry FP	Addgene	Cat#52114
pMSCV-IRES Rnf149 mCherry	This paper	NA
Software and algorithms		
GraphPad Prism (v 7.0 / 9.0)	GraphPad	https://www.graphpad.com/
FlowJo	TreeStar	https://www.flowjo.com/
Trimmomatic	Bolger et al.[97]	https://github.com/usadellab/Trimmomatic
STAR	Dobin et al.[98]	https://github.com/alexdobin/STAR
DESeq2	Love et al.[100]	https://github.com/mikelove/DESeq2
EnhancedVolcano	Bioconductor	https://github.com/kevinblighe/EnhancedVolcano
dsb	Mulè et al.[87]	https://github.com/niaid/dsb

REAGENT or RESOURCE	SOURCE	IDENTIFIER
Scanpy	Wolf et al.[88]	https://github.com/scverse/scanpy
scvi-tools	Gayoso et al.[90]	https://github.com/scverse/scvi-tools
gseapy	Fang et al.[93]	https://github.com/zqfang/GSEApy
clusterProfiler	Yu et al.[108]	https://github.com/YuLabSMU/clusterProfiler
GSVA	Hänzelmann et al.[109]	https://bioconductor.org/packages/release/bioc/html/GSVA.html
limma	Ritchie et al.[107]	https://bioconductor.org/packages/release/bioc/html/limma.html
pheatmap	CRAN	https://cran.r-project.org/web/packages/pheatmap/index.html
MAGIC	van Dijk et al.[102]	https://github.com/KrishnaswamyLab/MAGIC
contrastiveVI	Weinberger et al.[96]	https://github.com/suinleelab/contrastiveVI
UMAP	McInnes et al.[101]	https://github.com/lmcinnes/umap
nlfitr	Github	https://github.com/TJMurphy/nlfitr
broom	CRAN	https://CRAN.Rproject.org/package=broom
Seaborn	Waskom[95]	https://github.com/mwaskom/seaborn
Matplotlib	Hunter[94]	https://matplotlib.org/
ggplot2	CRAN	https://CRAN.Rproject.org/package=ggplot2
py_diAID	Skowronek et al.[105]	https://github.com/MannLabs/pydiaid
DIA-NN 1.8.1	Demichev et al.[106]	https://github.com/vdemichev/DiaNN
Biorender	Biorender	https://www.biorender.com/
R (v4.4.3)	The R Project for Statistical Computing	http://www.r-project.org
Spectronaut software (version 18.2 and 20.3)	Biognosys	https://biognosys.com/software/spectronaut/
Other		
LS Columns	Miltenyi Biotec	Cat#130-042-401
MidiMACS™ Separator and Starting Kits	Miltenyi Biotec	Cat#130-042-301
4D-Nucleofector® Core Unit	Lonza	Cat#AAF-1003B
4D-Nucleofector® X Unit	Lonza	Cat#AAF-1003X
PepMap Neo trap column	Thermo Scientific	Cat# 174500
PepSep reversed-phase C18 column	Bruker Daltonics	Cat# 1893476
Probe Sonicator	Fisher Scientific	Cat#FB120110
Molecular Devices SpectraMax iD3	Molecular Devices	NA
Resolvex A200	Tecan	NA
SpeedVac SPD210	Thermo Scientific	Cat# SPD210-230
EvoSep One	EvoSep	Cat# EV1000
timsTOF Pro	Bruker Daltonik	NA

REAGENT or RESOURCE	SOURCE	IDENTIFIER
Endurance Column (OE) – 30 SPD	EvoSep	Cat# EV1113